UNIVERSITÀ
DI TRENTO
Dipartimento di
Fisica

PhD Thesis

Second harmonic generation in engineered silicon waveguides

Candidate: Chiara Vecchi

Supervisor: Prof. Lorenzo Pavesi

XXXIII Cycle

A Davide
Sei stato il primo che mi ha stravolto la vita
e anche se quando torno a casa ora mi picchi
in fondo mi vuoi bene come quando eri piccolino

Second harmonic generation in engineered silicon waveguides

Chiara Vecchi

April 2021

Contents

1 *Introduction* **1**

Introduction **1**

1.1 Silicon Photonics 1
1.2 Nonlinear Optics 2
1.2.1 Second order nonlinearities 3
1.2.2 Third order nonlinearities 4
1.2.3 Phase matching 6
1.3 The NEMO project 9
1.4 SHG in Silicon 12
1.5 This Thesis 13

2 *Strained silicon waveguides* **15**

Strained silicon waveguides **15**

2.1 SHG theory 15
2.2 Waveguide theory 17
2.3 Optical pulses in nonlinear waveguides 21
2.4 Intermodal phase matching condition 27
2.5 The experiment 30
2.5.1 Setup 31
2.5.2 The sample 36
2.5.3 Investigating the strain 39
2.5.4 From the experiment to $\chi^{(2)}$ estimation 42
2.5.5 Investigating the electric field 43

3 *EFISH Generation* **52**

EFISH Generation **52**
3.1 EFISH theory 52
3.2 Propagation in poled waveguides 54
3.3 Poling configurations 56
3.4 The experiment 57
3.4.1 Setup 57
3.4.2 The sample 58
3.4.3 Electric Field Induced Second Harmonic Generation . 61
3.4.4 SHG as function of the pump 61
3.4.5 Modeling of the fabrication defects 63
3.4.6 Estimation of the conversion efficiency and $\Delta\chi^{(2)}$ . . . 73
3.4.7 Future prospects 77

4 ***Microring resonator design*** **78**

Microrings design **78**
4.1 SHG condition in a microring 78
4.1.1 Light propagation in a microring resonator 79
4.1.2 The momentum conservation 80
4.1.3 The radius of the ring 82
4.2 Pump wavelength vs geometrical parameters 84
4.3 Robust geometries 86
4.4 The $\bar{4}$ symmetry 91

5 ***Conclusion*** **92**

Conclusion **92**

Appendix A **94**

Appendix B **97**

Chapter 1

Introduction

1.1 Silicon Photonics

In the last century Silicon has brought a revolution in electronics. Thanks to semiconductor technology it is now possible to make devices in an integrated and scalable manner. The complementary metal-oxide semiconductors (CMOS) allowed to have fast and low-power consumption chips with nanometric sized transistors. The grow of microelectronics was set by the Moore's law in 1965, which predicts that the number of transistors on a microprocessor chip will double every two years.

Meanwhile, the world of communications is changing too. Optical fibers are replacing copper wires all around the world. Indeed, optical fibers are more performing than copper cables while allowing high speed transmission over very long distances at higher bandwidth.

The two technologies of communication and computers are still separated because they are based on different material platforms: silicon for electronics and silica and III_V semiconductors for the optical communication. In the recent years, a new approach has been introduced to merge these two worlds: silicon photonics. The aim of silicon photonics is to close the gap between communication and data processing [1]. Nowadays heavily integrated silicon photonics devices have been proposed. One of the recent developments is towards silicon acting as an active material for wavelength conversion, electro-optic modulation and generation of entangled photons pairs for quantum applications. Mostly, this can be done by using nonlinear optical

phenomena.

1.2 Nonlinear Optics

In order to understand nonliner optics, let us assume that the material polarization **P** is proportional to the applied electric field **E**. When the electric field is strong enough to be compared with the field inside atoms, this affects the electronic distribution in the cristalline structure, changing the material response to the applied field [2].

In a one-dimensional description, the polarization and the applied field are related by:

$$P = \alpha E \tag{1.1}$$

where α is a proportionality constant. For the Lorenz linear model, the atoms can be seen like harmonic oscillators and the relation between polarization and applied field is the equivalent of the Hook's law [3]. If the field is strong enough, it starts to affect the electronic distribution inside the atom. This can be seen like a perturbation on the field E, and so the equation 1.1 can be modified, using a Taylor expansion, in

$$P = \alpha E + \beta E^2 + \gamma E^3 + ... \tag{1.2}$$

where α, β and γ are proportionality constants. The term proportional to E is the linear term, the term proportional to E^2 is the second order nonlinear term, the term proportional to E^3 is the third order nonlinear term, and so on. Increasing the applied field it is possible to enable higher order nonlinearities. In a more general formulation, we can write 1.2 like:

$$\mathbf{P} = \mathbf{P}_0 + \mathbf{P}^{(2)} + \mathbf{P}^{(3)} + ... = \mathbf{P}_0 + \mathbf{P}_{NL} \tag{1.3}$$

being $\mathbf{P}_0$ the linear polarization vector and $\mathbf{P}_{NL}$ the nonlinear polarization vector given by the sum of all the n order nonlinear terms $\mathbf{P}^{(n)}$ [4]. From equations 1.2 and 1.3, setting out the equation for the linear constant α and nonlinear constant β and γ it is possible to write:

$$\mathbf{P}_0 = \varepsilon_0 \chi^{(1)} \cdot \mathbf{E} = \varepsilon_0 \sum_{ij} \chi_{ij}^{(1)} E_i \hat{\mathbf{u}}_j \tag{1.4}$$

$$\mathbf{P}^{(2)} = \varepsilon_0 \chi^{(2)} : \mathbf{E}^2 = \varepsilon_0 \sum_{ijk} \chi_{ijk}^{(2)} E_i E_j \hat{\mathbf{u}}_k \tag{1.5}$$

$$\mathbf{P}^{(3)} = \varepsilon_0 \chi^{(3)} \vdots \mathbf{E}^3 = \varepsilon_0 \sum_{ijkl} \chi_{ijkl}^{(3)} E_i E_j E_k \hat{\mathbf{u}}_l. \tag{1.6}$$

ε_0 is the vacuum permittivity, $\chi^{(1)}$ is the first order susceptibility tensor and it is related to the refractive index tensor n by the relation $\chi_{ij}^{(1)} + 1 = n_{ij}^2$, $\chi^{(2)}$ is the second order susceptibility tensor and $\chi^{(3)}$ is the third order susceptibility tensor.

1.2.1 Second order nonlinearities

To evaluate second order nonlinear phenomena the electric field can be written as a superposition of two monochromatic waves:

$$\mathbf{E}(\mathbf{r}, t) = \Re\left[\sum_{n=1}^{2} \widetilde{\mathbf{E}}_n(\mathbf{r}, \omega_n) e^{-i\omega_n t}\right] = \sum_{n=1}^{2} \left[\mathbf{E}_n(\mathbf{r}, \omega_n) e^{i\omega_n t} + c.c.\right] \tag{1.7}$$

where $\widetilde{\mathbf{E}}_n(\mathbf{r}, \omega_n) = 2\mathbf{E}_n(\mathbf{r}, \omega_n)$.

From equation 1.5, the second order nonlinear polarization is obtained:

$$\begin{aligned} \mathbf{P}^{(2)}(\mathbf{r}, t) = \varepsilon_0 \chi^{(2)} : \Big[& \mathbf{E}_1^2(\mathbf{r}, \omega_1) e^{-i2\omega_1 t} + \mathbf{E}_2^2(\mathbf{r}, \omega_2) e^{-i2\omega_2 t} + \\ & + 2\mathbf{E}_1(\mathbf{r}, \omega_1) \mathbf{E}_2(\mathbf{r}, \omega_2) e^{-i(\omega_1+\omega_2)t} + \\ & + 2\mathbf{E}_1(\mathbf{r}, \omega_1) \mathbf{E}_2^*(\mathbf{r}, \omega_2) e^{-i(\omega_1-\omega_2)t} + \\ & + \mathbf{E}_1(\mathbf{r}, \omega_1) \mathbf{E}_1^*(\mathbf{r}, \omega_1) + \mathbf{E}_2(\mathbf{r}, \omega_2) \mathbf{E}_2^*(\mathbf{r}, \omega_2) \Big] \\ & + c.c. \end{aligned} \tag{1.8}$$

Each line of equation 1.8 describes a different second order nonlinear process. The first line describes *Second Harmonic Generation* (SHG), where a photon at frequency ω_2 is generated from two photons at frequency $\omega_1 = \omega_2/2$.

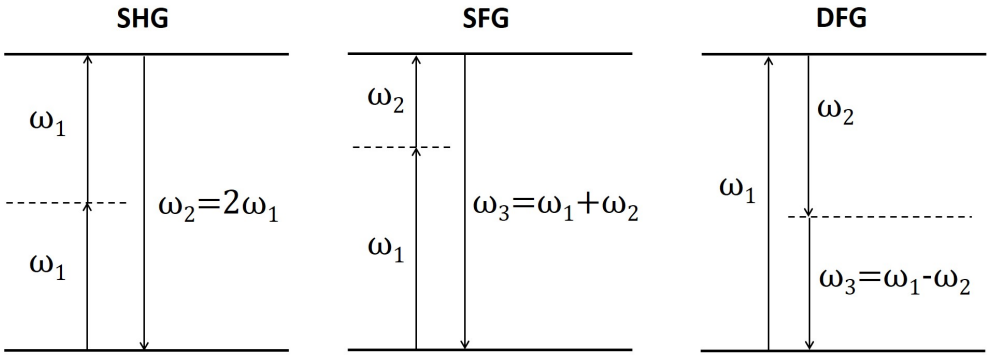

Figure 1.1: Schemes of the Second Harmonic Generation (SHG), Sum Frequency Generation (SFG) and Difference Frequency Generation (DFG) processes in a quantum picture.

The second line describes *Sum Frequency Generation* (SFG), where two photons at frequency ω_1 and ω_2 annihilate and a photon of a frequency $\omega_1 + \omega_2$ is generated. The third line describes *Difference Frequency Generation* (DFG), where the generated photon has a frequency $\omega_1 - \omega_2$. The last line is related to *Optical Retification* (OR) and generates a DC component.

1.2.2 Third order nonlinearities

Adopting the same procedure used for the second order nonlinear polarization vector, also the third order nonlinear polarization vector $P^{(3)}$ can be derived. The final result, where for simplicity all the permutations on the wave indices are omitted, is

$$\begin{aligned}
\mathbf{P}^{(3)}(\mathbf{r},t) = \varepsilon_0 \chi^{(3)} \vdots \Big[& \mathbf{E}_1^3(\mathbf{r},\omega_1)\, e^{-i3\omega_1 t} + \\
& + 3\mathbf{E}_1^2(\mathbf{r},\omega_1)\, \mathbf{E}_2(\mathbf{r},\omega_2)\, e^{-i(2\omega_1+\omega_2)t} + \\
& + 3\mathbf{E}_1^2(\mathbf{r},\omega_1)\, \mathbf{E}_2^*(\mathbf{r},\omega_2)\, e^{-i(2\omega_1-\omega_2)t} + \\
& + 6\mathbf{E}_1(\mathbf{r},\omega_1)\, \mathbf{E}_2(\mathbf{r},\omega_2)\, \mathbf{E}_3(\mathbf{r},\omega_3)\, e^{-i(\omega_1+\omega_2+\omega_3)t} + \\
& + 6\mathbf{E}_1(\mathbf{r},\omega_1)\, \mathbf{E}_2(\mathbf{r},\omega_2)\, \mathbf{E}_3^*(\mathbf{r},\omega_3)\, e^{-i(\omega_1+\omega_2-\omega_3)t} + \\
& + 3\left|\mathbf{E}_1(\mathbf{r},\omega_1)\right|^2 \mathbf{E}_1(\mathbf{r},\omega_1)\, e^{-i\omega_1 t} + \\
& + 6\left|\mathbf{E}_2(\mathbf{r},\omega_2)\right|^2 \mathbf{E}_1(\mathbf{r},\omega_1)\, e^{-i\omega_1 t} \Big] \\
& + c.c.
\end{aligned} \tag{1.9}$$

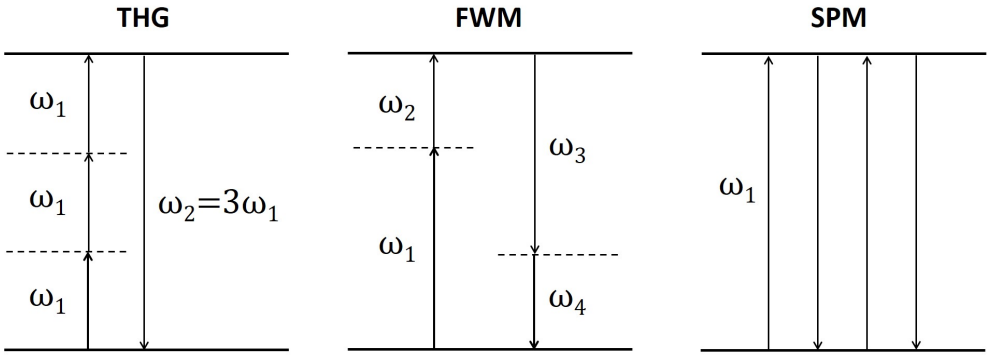

Figure 1.2: Schemes of the Third Harmonic Generation (THG), stimulated Four Wave Mixing (FWM) and Self Phase Modulation (SPM) processes in a quantum picture.

The term in the first line describes *Third Harmonic Generation* (THG). Similarly to SHG, THG is obtained when three photons with identical frequencies ω_1 annihilate and a photon is generated at the triple frequency $\omega_3 = 3\omega_1$.

The elements from the second to the fifth lines describe *stimulated Four Wave Mixing* (FWM), which takes place when two pump waves interact with a weak wave, providing an amplification of the weak wave and the generation of a fourth wave. The generated wave at lower frequency is called signal and the generated wave at larger frequency is called idler. A different process that involve four waves is the spontaneous FWM, that is a non-classical process that is stimulated by vacuum fluctuations. In this case, the signal and the idler photons are directly generated without the interaction with the weak wave [5].

The term in the sixth line describes the *Self Phase Modulation* (SPM), that is governed by the real part of $\chi^{(3)}$ and is responsible of intensity-dependent perturbations of the refractive index, and the *Two Photon Absorption* (TPA), that is controlled to the imaginary part of $\chi^{(3)}$ and is responsible of intensity-dependent variations of the absorption coefficient. SPM is known also as AC Kerr effect. In this case, the material refractive index n can be written as [6]:

$$n = n_0 + n_2 I + i\frac{\lambda}{4\pi}\left[\alpha_0 + \beta_{TPA} I\right] \tag{1.10}$$

with n_0 linear refractive index, α_0 linear loss coefficient, λ wavelength, n_2 Kerr coefficient, β_{TPA} TPA coefficient and I field intensity. The coefficients n_2

and β_{TPA} are related to the effective third order nonlinear coefficient $\chi^{(3)}_{eff}$ by [6, 7]:

$$n_2 = \frac{3}{4\varepsilon_0 c n_0^2} \Re\left(\chi^{(3)}_{eff}\right) \tag{1.11}$$

$$\beta_{TPA} = \frac{3\omega}{2\varepsilon_0 c^2 n_0^2} \Im\left(\chi^{(3)}_{eff}\right) \tag{1.12}$$

with c speed of light in the vacuum. This two coefficients are related together by the Figure Of Merit $FOM = n_2 / (\lambda \beta_{TPA})$. Larger is the FOM, more efficient is the third order nonlinearity of the material.

The term in the seventh line indicates *Cross Phase Modulation* (XPM), where the propagation of a signal at frequency ω_1 is perturbed by a signal at frequency ω_2.

When one wavelength is weaker than the others or is set to DC, a peculiar dependence of $P^{(3)}(\mathbf{r}, t)$ appears. Let us consider in 1.9 the second and the third lines and let us use a DC field for ω_2 (i.e. $\omega_2 = 0$), then:

$$\mathbf{P}^{(3)}(\mathbf{r}, t) = 3E_1^2(r, \omega_1) E_{DC} e^{-i2\omega_1 t} + 3E_1^2(r, \omega_1) E_{DC} e^{-i2\omega_1} \tag{1.13}$$

which resembles to a SHG process. However, a DC electric field is needed to enable SHG by $\chi^{(3)}$. This process is called *Electic Field Induced SHG* (EFISH). Moreover, when $\omega_3 = 0$, additional phase-modulation terms appear in $P^{(3)}$, introducing a perturbation of the material refractive index. This perturbation scales quadratically with the low-frequency wave amplitude. This process is called *DC Kerr effect* and is the first nonlinear optical effect demonstrated in 1875 by the scotsman John Kerr.

1.2.3 Phase matching

All the processes that involve frequency conversion, such as SHG, DFG, SFG, THG and FWM are called parametric processes. Parametric processes are related to the real part of the suscettibility tensor, therefore photon energy conservation always occurs, while non-parametric processes are related to his immaginary part.

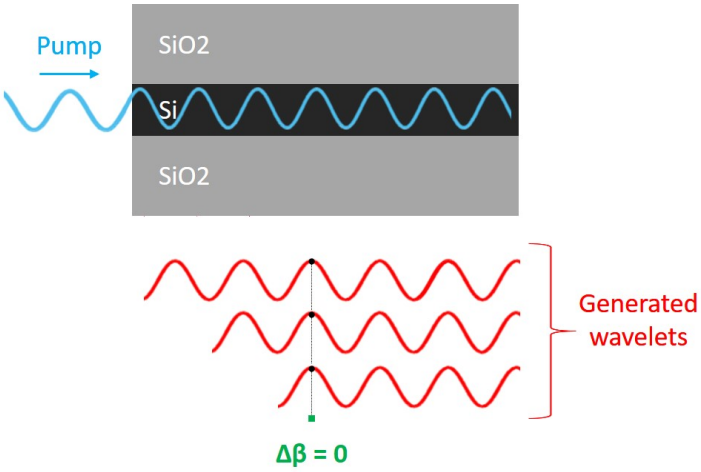

(a)

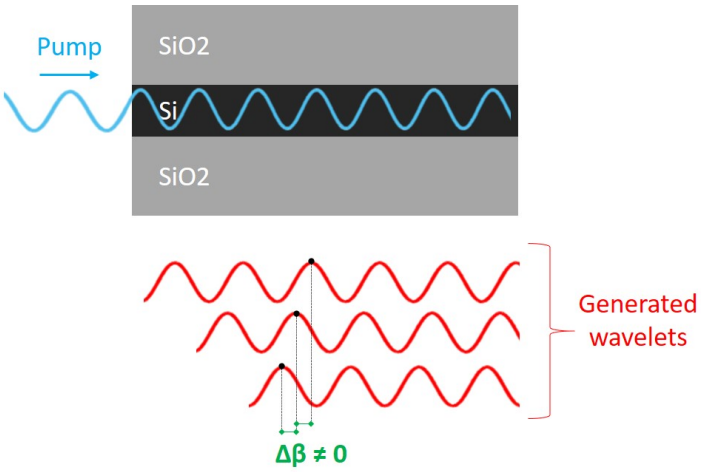

(b)

Figure 1.3: In the case of perfect phase matching ($\Delta\beta = 0$) all the generated wavelets sum in a constructive way.

In order to be efficient, parametric processes need to satisfy the *phase matching condition*. For the phase-matching condition in a SHG process, it defines the propagation constant β as:

$$\beta = \frac{2\pi}{\lambda} n \tag{1.14}$$

and the mismatch coefficient $\Delta\beta$ as:

$$\Delta\beta = 2\beta_p - \beta_{SH} = 2\frac{2\pi}{\lambda_p} n_p - \frac{2\pi}{\lambda_{SH}} n_{SH} = \frac{4\pi}{\lambda_p} \left(n_p - n_{SH}\right), \tag{1.15}$$

where β_p and β_{SH} are the propagation constants for the pump wavelength (i.e. at frequency ω_1) and for the second harmonic wavelength (at frequency $\omega_2 = 2\omega_1$). In order to satisfy the phase matching condition, the mismatch coefficient must be close to zero. This is because the generation efficiency is proportional to a coefficient of form $sinc^2\left(\frac{\Delta\beta L}{2}\right)$ where L is the length of the region where interaction occurs [3]. To satisfy the phase-matching condition means that all the contributions to SH generated in different region of the sample add up constructively. This condition is hard to fulfill automatically. Therefore, different techniques were developed to ease the task. In particular, in integrated photonics, thanks to the effective index dispersion, a used phase-matching technique is the *intermodal phase-matching* [8]. It consists in the use of different optical modes in a waveguide for the pump and the second harmonic, in order to obtain phase-matching between the two waves. In fact, the effective index in a waveguide is a function of the wavelength. This effect is due to the chromatic dispersion of the material. Another technique is the *birefringent phase-matching* [9, 10], where the two waves, propagating with different polarizations, are subjected to different refractive indexes due to the birefringence of the material. Both these two techniques work on n_p and n_{SH} in order to achieve the condition $\Delta\beta = 0$, so that a perfect phase-matching between the pump and the second harmonic is achieved. Another mechanism that can be used is the *Quasi Phase-matching Condition* (QPM). In this technique, the phase-matching condition is achieved by using a spatial modulation of the material nonlinearities to account for the mismatch between the two different modes. In this way the new mismatch parameter is

$\Delta\beta = 2\Delta\beta_p - \Delta\beta_{SH} + \frac{2\pi m}{\Lambda}$, where m is an integer number and Λ is the periodicity of the nonlinearity variation [3]. The most common way is to introduced a periodic change in the sign of the nonlinear coefficient of the material creating periodic structure in the nonlinear medium [36]. This technique is called poling. There are also many different techniques exploiting natural properties of nonlinear materials. An example is the use of the $\bar{4}$ symmetry phase matching in crystals like GaP, GaAs and ZnSe. $\bar{4}$ symmetry means that using a 90° and a crystal inversion it is possible to reproduced the original crystalline structure [11]. In a material that shows this kind of symmetry it is possible to create a periodic structure rotating the crystal of 90° in a periodic way along the waveguide. In this structure the propagating wave experiments a periodic domain inversion.

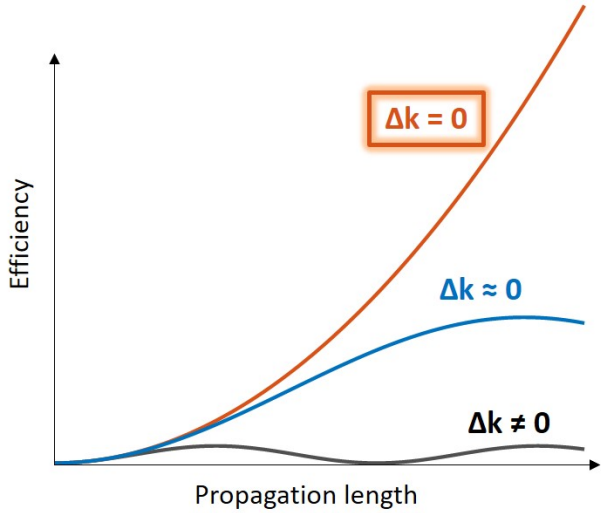

Figure 1.4: Generation efficiency as a function of the propagation length. When the phase matching condition is respected the process reach the maximum of the efficiency.

1.3 The NEMO project

The work reported in this thesis was within a national project named NEMO [12]. The project NEMO (*Nonlinear dynamics of optical frequency combs*) is a 36 months Research Project of National Interest (PRIN) that started in 2017. Part-

ners of the projects are the University of Brescia, the University *La Sapienza* of Rome, the CNR institute of Naples, the INO institute of Florence and the University of Trento. The goal of the project is to find chip-scale integrable methods for the generation of optical frequency combs (OFCs) using second order nonlinearities.

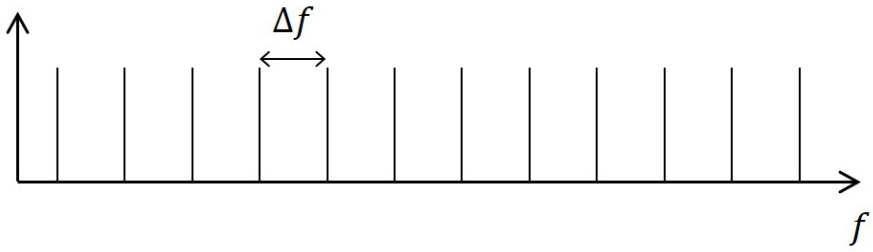

Figure 1.5: Sketch of an optical frequency comb (OFC). OFCs are light source with thousands of laser lines spaced in frequency by the same quantity Δf.

OFCs are light sources with a spectrum containing thousands of equally spaced laser lines, that have application in many different fields like synchronization of telecommunication systems, astronomical spectral calibration, biomedical or environmental spectrometry [13, 14]. The peculiarity of OFCs is that an octave span OFC allows to do high precise optical frequency measurements. Nowaday OFCs are available in the visible (VIS) and near-infrared (NIR) spectral range and can be transferred to the mid infrared (MIR) spectral range by difference frequency generation or optical parametric oscillation [15]. OFCs in the MIR region can also be directly generated using quantum cascade lasers (QCLs) [16]. Thanks to OFCs with direct broad spectral emission in the MIR region, it is possible to simultaneously monitoring multiple trace gas species and doing quantitative detection of liquid and solid samples [12]. Furthermore, MIR spectroscopy is a powerful technique for identifying and quantifying molecular species and non-intrusive diagnostics of composite systems of physical, chemical or biological interest in gas, liquid or solid phase. MIR spectrometers are used in research, minimally invasive medical diagnostics, environmental monitoring, industrial real-time process control, and security applications and they could be used to assess the quality of pharmaceutical and food products and facilitating process control during production. In 2011 Kippenberg et al. showed how passive comb sources

based on Kerr microresonators give the technological possibility to reduce the size of OFC devices [17]. Then, OFC generation was demonstrated also in bulk free-space resonators, where OFCs may arise entirely through second-order nonlinear effects [18]. In this work, SHG was provided by a periodically poled lithium niobate (LN) crystal placed in a traveling-wave optical cavity. The poled LN crystal shows a high $\chi^{(2)}$, while the cavity was designed to be resonant around the fundamental pump wavelength $\lambda_p = 1064.45$ nm. Fundamental and generated beams are separated after leaving the cavity by a dichroic mirror and sent to different collection stages. With the proper poling, the LN can provide either SHG or optical parametric oscillations (OPO), depending on whether it is pumped by the fundamental or the second harmonic mode. In this way a broadband quadratic comb is generated both around the fundamental pump frequency and its second harmonic. This work takes the advantage of the use of second order nonlinearities, which are simpler to control, require low pump power to be accessible and intrinsically lead to the simultaneous generation of two octave-distant combs that can provide a useful link between two spectral regions for metrological applications.

One of the aim of the NEMO project is to reproduce the same effects in a silicon microresonator. Silicon is currently the most used platform for photonics integration, so employing a silicon microring allows to have a compact low cost scalable OFC source that can be integrated with the C-MOS technology. However, the crystalline structure of silicon has a diamond-like structure. This means that bulk silicon is a centrosymmetric material. In this material, the polarization vector must satisfy the condition:

$$\mathbf{P}(\mathbf{E}) = -\mathbf{P}(-\mathbf{E}). \tag{1.16}$$

From equation 1.3 it is possible to notice that for second order nonlinearities the condition

$$\mathbf{P}^{(2)}(\mathbf{E}) = -\mathbf{P}^{(2)}(-\mathbf{E}) \tag{1.17}$$

is fulfilled only when $\mathbf{P}^{(2)} = 0$, meaning that, for centrosimmetric materials, all the second order nonlinearities are inhibited and $\chi^{(2)} = 0$ in the dipole approximation.

The role of the university of Trento in this project is to obtain SHG in silicon waveguides, and then design and test a microring suitable for second order comb generation in collaboration with the Naples team.

1.4 SHG in Silicon

Second Harmonic Generation (SHG), is a parametric second order nonlinear effect. Being a second order nonlinear process, it is directly linked to the $\chi^{(2)}$ of the material. As silicon $\chi^{(2)} = 0$ in the dipole approximation, nowadays most of the nonlinear silicon photonics devices use third order nonlinearities, which are strong in silicon due to a high third order nonlinear coefficient $\chi^{(3)}$. Still, second order nonlinearities are appealing for silicon photonics. In the last ten years, lots of effort was spent to obtain second order nonlinear process in silicon, and strained silicon waveguides appeared as the most viable solution. In this kind of structures, the centrosymmetry of bulk silicon is mechanically broken by an inhomogeneous strain which is applied on the silicon waveguide by a stressing layer of a different material with a different lattice constant deposited as a cladding [19]. The first experiment with strain silicon waveguides using a silicon nitride stressing layer was performed by Jacobsen et al. in 2006 [20] measuring the Pockels effect. In Jacobsen's work a second order nonlinear coefficient $\chi^{(2)} = 15$ pm/V was determined using a stressing layer of amorphous SiN deposited on the top of a photonic crystal waveguide. The photonic crystal structure was obtained by air holes carved on the lateral side of the waveguide. An additional SiO_2 layer was sandwiched between the waveguide and the stressing layer. This work was followed by many others and values of the strain-induced $\chi^{(2)}$ up to 340 pm/V were estimate from DC measurements of the EO effect [21, 22]. In the work by Chmielak et al. [21] the Si_3N_4 stressing layer was deposited directly on the top of a rib waveguide; in this way, both the top surface and the vertical sidewalls are subject to tensile strain. In the work by Damas et al. [22] a strip waveguide grown on a SiO_2 wafer was surrounded by Si_3N_4 and on the top of the structure an additional layer of SiO_2 was deposited. Second order nonlinearities in Silicon where also investigated using Second Harmonic Generation (SHG), where in multimodal waveguides without any specific phase matching mechanism a value of $\chi^{(2)} = 40 \pm 30$ pm/V was

claimed [23]. In this work it was also offered the first quantitative model of second-order nonlinearities in strained silicon from first principle calculation.

However, other studies questioned the interpretation of these measurements. Actually, during the deposition of the stressing layer, dangling bonds form at the interface between this SiN and silicon. The dangling bonds form charged defects that act as positive fix ions and release free-carriers in the core of the waveguide. Azadeh et al. [24] demonstrated that frozen charges at the interface between the silicon waveguide and the stressing layer determined an abundance of free-carriers in the waveguide that can affect the value of the effective measured nonlinear coefficient in DC electro-optic measurements because of the free carrier dispersion. Also, Olivares et al. invoked free carrier dispersion as the mechanism ruling the apparent second order nonlinearity [25]. In addition an upper limit of the value of the $\chi^{(2)}$ was experimentally fixed at 8 pm/V by a frequency dependent measurement that allowed to separate the effect due to free-carriers [26]. Finally, it was also demonstrated that different materials used to stress silicon gave different values for the SHG efficiency even if the induced strain was the same [27]. These observations suggest that the second order nonlinearity in strained silicon is not only due to the strain: the defects formed at the core/cladding interface play an important role too. Moreover, in this work for the first time it was demonstrated that the positive charges at the interface of the two different materials can generate an electric E_{DC} field in the core of the waveguide. This field, coupled with the high $\chi^{(3)}$ of silicon, generates via EFISH generation an effective $\chi^{(2)}_{EFISH} = 3\chi^{(3)}E_{DC}$. The greatest problem is that both strain and EFISH coexist in this kind of structures. Therefore, the final measurable $\chi^{(2)}$ is a superposition of the two effects.

In order to be able to generate a controlled $\chi^{(2)}$ in a silicon microring, the origin of this effect must be made clear. Then the second order nonliearity will be engineered in a silicon microring suitable for comb generation.

1.5 This Thesis

The principal purpose of my thesis is to understand and control SHG in silicon. Chapter 2 and Chapter 3 are dedicated to the study of SHG in Silicon. Chapter 2 presents an experiment that allows to isolate and study separately

the effect of strain and EFISH in a strained silicon waveguide via SHG. It is demonstrated that the main responsible of $\chi^{(2)}$ in silicon is the EFISH, setting also an upper limit to the strain induced $\chi^{(2)}$. An estimate of the charge density at the Si/SiN interface has been done too. In Chapter 3, a way to generate a controlled $\chi^{(2)}$ using EFISH is proposed. A new design of a poled waveguide is proposed to reach a generation higher than other literature results.

Chapter 4 is dedicated to the study of a set of geometries of microring suitable for SHG that are robust against fabrication defects. Taking advantage of the $\bar{4}$-symmetry of $\chi^{(2)}$, a general method to engineer the microrings is proposed.

Chapter 2

Strained silicon waveguides

2.1 SHG theory

In a bulk material, starting with Maxwell's equation, if $\rho = 0$ and $j = 0$ it is possible to obtain the optical wave equation

$$\boldsymbol{\nabla} \times \boldsymbol{\nabla} \times \mathbf{E} + \frac{1}{c^2} \frac{\partial^2 \mathbf{E}}{\partial t^2} = 0. \tag{2.1}$$

In a medium without losses and dispersion one may obtain:

$$\mathbf{D} = \varepsilon \mathbf{E} + \mathbf{P} \tag{2.2}$$

$$\mathbf{D}^{(1)} = \varepsilon_0 \mathbf{E} + \mathbf{P}^{(1)} = \varepsilon_0 \varepsilon^{(1)} \mathbf{E}. \tag{2.3}$$

Assuming that the pump power is varying slowly, it is possible to obtain [3]:

$$-\nabla^2 \mathbf{E} + \frac{\varepsilon^{(1)}}{c^2} \frac{\partial^2 \mathbf{E}}{\partial t^2} = -\frac{1}{\varepsilon_0 c^2} \frac{\partial^2 \mathbf{P}_{NL}}{\partial t^2}. \tag{2.4}$$

Neglecting the nonlinear term, the solution would be:

$$\mathbf{E}(z,t) = \frac{1}{2} a \left(e^{i(k_\omega z - \omega t)} + c.c. \right) \tag{2.5}$$

where a is the amplitude, z is the propagation direction, $k_\omega = \frac{n_\omega \omega}{c}$ and $n^2 = \varepsilon^{(1)}$. A similar solution can be assumed for the SH mode, but with a variation in the amplitude along z:

$$\mathbf{E}_{SH}(z,t) = \frac{1}{2} a_{SH} \left(e^{i(k_{SH} z - \omega_{SH} t)} + c.c. \right). \tag{2.6}$$

From 1.8, substituting the solution obtained it is possible to write $\mathbf{P}_{SH}^{(2)}$ as:

$$\mathbf{P}_{SH}^{(2)} = \frac{1}{2} \varepsilon_0 \chi^{(2)} a_p^2 \frac{1}{2} \left(e^{2i(k_p z - \omega_p t)} + c.c. \right). \tag{2.7}$$

Substituting $\mathbf{P}_{SH}^{(2)}$ and $\mathbf{E}_{SH}$ in 2.4 one obtains:

$$\begin{aligned} &\left(\frac{d^{(2)} a_{SH}}{dz^2} + 2ik_{SH} \frac{da_{SH}}{dz} - k_{SH}^2 a_{SH} + \frac{\varepsilon_{SH}^1 \omega_{SH}^2}{c^2} a_{SH} \right) e^{ik_{SH} - \omega_{SH} t} + c.c. = \\ &- \frac{\chi^{(2)} a_p^2 \omega_{SH}^{(2)}}{2c^2} e^{i(2k_p z - \omega_{SH} t)} + c.c. \end{aligned} \tag{2.8}$$

Applying the slowly varying amplitude approximation $\left| \frac{d^2 a_{SH}}{dz^2} \right| \ll \left| k_{SH} \frac{da_{SH}}{dz} \right|$ equation 2.8 can be simplified to:

$$\frac{da_{SH}}{dz} = \frac{i\chi^{(2)} a_p^2 \omega_{SH}^2}{4k_{SH} c^2} e^{i\Delta\beta z} \tag{2.9}$$

with $\delta k = 2k_p - k_{SH}$. Integrating the equation from $z = 0$ to $z = L$ generation length, it is possible to obtain:

$$a_{SH} = \int_0^L \frac{i\chi^{(2)} a_p^2 \omega_{SH}^2}{4k_{SH} c^2} e^{i\Delta k z} dz = \frac{i\chi^{(2)} a_p^2 \omega_{SH}^2}{4k_{SH} c^2} \left(\frac{e^{i\Delta k L - 1}}{i\Delta k} \right). \tag{2.10}$$

The optical intensity [3] is:

$$I = \frac{1}{2} n c \varepsilon_0 |a|^2 \tag{2.11}$$

so for I_{SH} it would be:

$$I_{SH} = \frac{\left(\chi^{(2)}\right)^2 \omega_{SH}^2}{8c^3 n_{SH} n_p^2 \epsilon_0} I_p^2 L^2 sinc^2\left(\frac{\Delta kL}{2}\right). \tag{2.12}$$

The intensity's maximum is obtained under perfect phase matching condition ($\Delta k = 0$), in this condition the intensity is proportional to:

$$I_{SH} \propto (\chi^{(2)})^2 I_P^2 L^2 \tag{2.13}$$

clearly showing how the intensity of the generated wave quadratically scales with $\chi^{(2)}$.

2.2 Waveguide theory

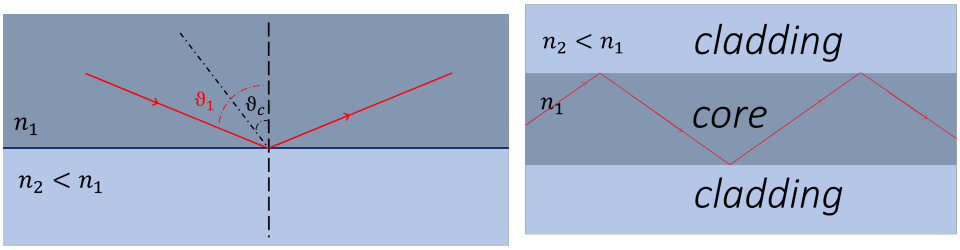

(a) (b)

Figure 2.1: (a) sketch of total internal reflection process: when $n_2 < n_1$ and $\vartheta_1 > \vartheta_c$ the total reflection occurs; (b) sketch of an index-guiding waveguide.

When a waveguide is considered, the situation changes. Index-guiding waveguides are structures based on total internal reflection. Total internal reflection occurs when a propagating wave in a medium with a refractive index n_1 reaches an interface with a different medium with refractive index n_2 at an angle ϑ_1 larger than a particular critical angle ϑ_c with respect to the normal to the surface. If $n_2 < n_1$ the wave is entirely reflected, as shown in figure 2.1(a). In figure 2.1(b) is shown a sketch of an index-guiding structure. In order to exploit the total internal reflection, index-guiding waveguides are characterized by a core composed by a material with a high refractive index n_1 surrounded by a cladding of a lower refractive index n_2 material.

Waveguides can be produced using several different geometries, the more frequently used are sketched in figure 2.2. The most common wavegide is the optical fiber, which has a cylindrical shape. In the slab waveguide, the core and the cladding materials extend infinitely and light is confined only in the direction perpendicular to this plane. Light is confined in two directions in the strip waveguide, where a strip of core material is embedded into the cladding. Similarly, in the rib waveguide a slab waveguide is superimposed by a strip waveguide.

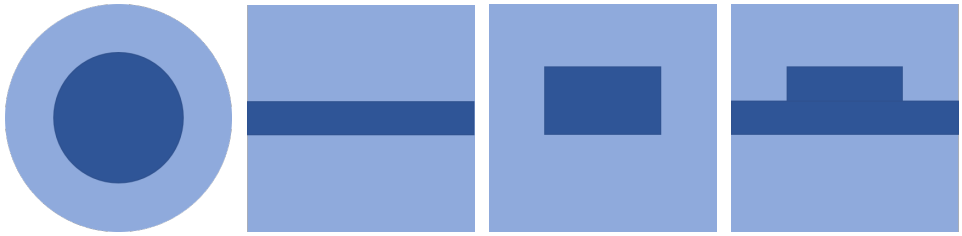

(a) (b) (c) (d)

Figure 2.2: Cross-section of some of the most common waveguide geometries: (a) cylindrical shape waveguide, (b) slab waveguide, (c) strip waveguide and (d) rib waveguide.

In an optical waveguide, the two materials are chosen so that the critical angle ϑ_c is very small. In this way the light that passes through the waveguide is all confined in the core and is guided by this structure. Light travels in the form of discrete modes of electric field profiles $e_m(x, y, \omega)$ in the perpendicular plane to the propagating direction (x, y), which are solutions of the Helmholtz equation [28]:

$$\left(\nabla^2_{(x,y)} + \left[\beta^{(m)}\right]^2\right) e_m\left(x, y, \omega\right) = \frac{\omega^2}{c^2} n^2\left(x, y\right) e_m\left(x, y, \omega\right). \tag{2.14}$$

The refractive index $n(x, y)$ for a fixed wavelength depends only on the cross section of the waveguide, therefore the dependence in these coordinates is of the form $e^{i\beta^{(m)}z}$ were $\beta^{(m)}$ is the propagation constant of the mth mode.

The propagation constant β depends on the frequency, and it can be expanded as a Taylor series around a central frequency ω_0 as follows:

$$\beta(\omega) = \sum_j \frac{\beta_j}{j!} (\omega - \omega_0)^j \tag{2.15}$$

with

$$\beta_j = \frac{\partial^j \beta}{\partial \omega^j}. \tag{2.16}$$

The result is:

$$\beta(\omega) = \beta_0 + (\omega - \omega_0) \frac{\partial^1}{\partial \omega^1} + \frac{1}{2} (\omega - \omega_0)^2 \frac{\partial^2 \beta}{\partial \omega^2} + \frac{1}{6} (\omega - \omega_0)^3 \frac{\partial^3 \beta}{\partial \omega^3} ... \tag{2.17}$$

The term β_0 is related to phase velocity v_{phase} by the relation:

$$v_{phase} = \frac{c}{n_{eff}} = \frac{\omega}{\beta_0} \tag{2.18}$$

with c speed of light and n_{eff} effective index of the mode:

$$\beta_0 = \frac{2\pi}{\lambda} n_{eff}(\omega_0). \tag{2.19}$$

The term β_1 is related to the group velocity v_g of the mode in the waveguide and to the group index of the mode n_g by the relation:

$$v_g = \frac{1}{\beta_1} = \frac{c}{n_g}. \tag{2.20}$$

with c speed of light. Using equation 1.14 it is possible to obtain:

$$n_g = c\beta_1 = n_{eff}(\lambda) - \lambda \frac{\partial n_{eff}(\lambda)}{\partial \lambda}. \tag{2.21}$$

Fitting the effective refractive index as function of the wavelength

$$n_{eff}(\lambda) = C + B\lambda + A\lambda^2 \tag{2.22}$$

it is possible to extract the group index from the index dispersion in the waveguide as:

$$n_g = C - A\lambda^2. \tag{2.23}$$

The term β_2 is called the Group Velocity Dispersion (GVD). The GVD can also be extracted from the index dispersion in the waveguide:

$$GVD = \frac{1}{c}\frac{\partial n_g}{\partial \omega} = \frac{A\lambda^3}{\pi c^2}. \tag{2.24}$$

When $\beta_2 > 0$ the dispersion is said to be normal, while it is anomalous if $\beta_2 < 0$. The values assumed by $\beta^{(m)}$ are function of the geometrical parameters of the waveguide and the smaller is the structure, more dominant are the effects of the variations in the geometry.

In addition to the modal order m, optical modes are also classified based on their polarization. The classification between *Transverse Electric* (TE) and *Transverse Magnetic* (TM) modes is done on the basis of their dominant electric field component, which coincides with the direction parallel to the waveguide width in case of TE modes, and the direction parallel to the waveguide height for TM modes. For the m*th* mode the modal confinement factor is defined as:

$$\Gamma_m = \frac{\int_{A_0} n^2(x,y)\left|e_m(x,y)\right|^2 dxdy}{\int n^2(x,y)\left|e_m(x,y)\right|^2 dxdy} \tag{2.25}$$

where the numerator integral is evaluated over waveguide's cross section area A_0, while the denominator integral is evaluated over all the xy plane. The higher the modal order, the lower is the confinement factor as defined in equation 2.25. As a consequence, the effective index monotonically decreases as the modal order increases, since the optical field is more subjected to the external refractive index. Given the waveguide geometry, the maximum number of supported modes is limited and no analytical expression exists to determine this number.

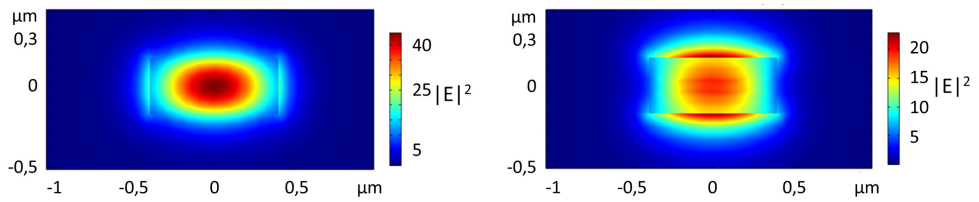

(a) (b)

Figure 2.3: (a) modal profile of the norm of the electric field for a TE mode supported by a (800×350) nm silicon waveguide for $\lambda = 1.55$ μm wavelength; (b) modal profile of the norm of the electric field for a TM mode supported by a (800×350) nm silicon waveguide for $\lambda = 1.55$ μm wavelength.

2.3 Optical pulses in nonlinear waveguides

The presence of optical nonlinearities in waveguides induces a perturbation $\delta\mathbf{P} = \mathbf{P}_{NL} \neq 0$ that modifies the electromagnetic field. The pulse can be described by the electromagnetic field $(\mathbf{E}_0, \mathbf{H}_0)$ and the perturbation induces a modification $(\mathbf{E}_1, \mathbf{H}_1)$ in the electric field [7, 29]. Using the Lorentz's reciprocity theorem it is possible to relate together the perturbed and unperturbed field as:

$$\frac{\partial}{\partial z}\int_A (\mathbf{E}_0^* \times \mathbf{H}_1 + \mathbf{E}_1 \times \mathbf{H}_0^*) \cdot \hat{z}\, dA = i\omega \int_A \mathbf{E}_0^* \cdot \delta\mathbf{P}\, dA \tag{2.26}$$

where the integrals are evaluated on the whole plane orthogonal to the field propagation direction in the waveguide A and ω is the pulse frequency. From now onwards it is assumed that the unperturbed pulse spectral width $\Delta\omega$ is much smaller than its central frequency ω_0 ($\Delta\omega \ll \omega_0$). In this situation the field $(\mathbf{E}_0, \mathbf{H}_0)$ can be written as:

$$\begin{aligned} \mathbf{E}_0(\mathbf{r}, \omega_0) &= \frac{1}{2}\mathbf{e}(\mathbf{r}_\perp, \omega_0)\, e^{i\beta_0 z} \\ \mathbf{H}_0(\mathbf{r}, \omega_0) &= \frac{1}{2}\mathbf{h}(\mathbf{r}_\perp, \omega_0)\, e^{i\beta_0 z} \end{aligned} \tag{2.27}$$

being $\beta_0 = \beta(\omega_0)$, $\mathbf{r}_\perp$ a vector in the A plane, $\mathbf{e}(\mathbf{r}_\perp, \omega_0)$ and $\mathbf{h}(\mathbf{r}_\perp, \omega_0)$ the profiles of the electromagnetic field at frequency ω_0 in the A plane. Under these conditions the total power P_0 of the unperturbed electromagnetic field is:

$$P_0 = \frac{1}{4}\int_A \left[\mathbf{e}\left(\mathbf{r}_\perp,\omega_0\right)\times\mathbf{h}^*\left(\mathbf{r}_\perp,\omega_0\right)+\mathbf{e}^*\left(\mathbf{r}_\perp,\omega_0\right)\times\mathbf{h}\left(\mathbf{r}_\perp,\omega_0\right)\right]\cdot\hat{z}\,dA. \quad (2.28)$$

The perturbed field $(\mathbf{E}_1, \mathbf{H}_1)$ can be written as:

$$\begin{aligned}\mathbf{E}_1\left(\mathbf{r},\omega\right) &= \frac{1}{2}u\left(z,\omega\right)\mathbf{e}\left(\mathbf{r}_\perp,\omega\right)e^{i\beta(\omega)z}\\ \mathbf{H}_1\left(\mathbf{r},\omega\right) &= \frac{1}{2}u\left(z,\omega\right)\mathbf{h}\left(\mathbf{r}_\perp,\omega\right)e^{i\beta(\omega)z}\end{aligned} \quad (2.29)$$

where $u\left(z,\omega\right)$ is the modulation of the amplitude introduced by the perturbation. Assuming that the perturbation is small enough to guarantee:

$$\mathbf{e}\left(\mathbf{r}_\perp,\omega\right)\sim\mathbf{e}\left(\mathbf{r}_\perp,\omega_0\right);\ \ \mathbf{h}\left(\mathbf{r}_\perp,\omega\right)\sim\mathbf{h}\left(\mathbf{r}_\perp,\omega_0\right) \quad (2.30)$$

the optical power carried by the perturbed field is:

$$P = P_0\left|u\left(z,\omega\right)\right|^2. \quad (2.31)$$

The partial differential equation describing the spatial evolution of the mode amplitude may be obtained by inserting the definitions 2.27 and 2.29 in equation 2.26:

$$\frac{du\left(z,\omega\right)}{dz}+i\left(\beta-\beta_0\right)u\left(z,\omega\right)=\frac{i\omega}{2P_0}e^{-i\beta z}\int_A\mathbf{e}^*\left(\mathbf{r}_\perp\omega_0\right)\cdot\delta\mathbf{P}\left(\mathbf{r},\omega\right)\,dA. \quad (2.32)$$

Equation 2.32 describes the propagation of optical pulses in waveguides under the effect of a polarization vector perturbation $\delta\mathbf{P}\left(\mathbf{r},\omega\right)$. If different optical pulses with frequencies sufficiently spaced far apart are propagating in the same waveguide, it is necessary to write a separate equation like equation 2.32 for each of them. Otherwise, a single equation should be used.

For SHG, two different pulses are propagating in the waveguide, the pump pulse at frequency ω_p and the SH pulse at frequency $\omega_{SH} = 2\omega_p$, without overlap between the two spectra. However silicon shows a strong $\chi^{(3)}$ that induces third order pulse distortion effects that must be considered.

Moreover, fabrication imperfections introduce in the waveguide a linear absorption term, which determines a perturbation of the polarization vector as well. Therefore, the polarization vector perturbation $\delta\mathbf{P}$ can be written as:

$$\delta\mathbf{P}\left(\mathbf{r},\omega\right)=\mathbf{P}^{(2)}\left(\mathbf{r},\omega\right)+\mathbf{P}^{(3)}\left(\mathbf{r},\omega\right)+\mathbf{P}_{L}\left(\mathbf{r},\omega\right) \tag{2.33}$$

being $\mathbf{P}^{(2)}\left(\mathbf{r},\omega\right)$ the polarization vector term related to $\chi^{(2)}$, $\mathbf{P}^{(3)}\left(\mathbf{r},\omega\right)$ the polarization vector related to $\chi^{(3)}$ and $\mathbf{P}_{L}\left(\mathbf{r},\omega\right)$ the polarization vector related to propagation losses that will induced a linear perturbation of the polarization vector. This perturbation will affect both the SH and the pump modes.

For the SH pulse, according to equation 1.5 the term $\mathbf{P}^{(2)}\left(\mathbf{r},\omega_{SH}\right)$ is written as:

$$\begin{aligned}\mathbf{P}^{(2)}\left(\mathbf{r},\omega_{SH}\right)&=\varepsilon_{0}\chi^{(2)}:\mathbf{E}_{p}^{2}\left(\mathbf{r},\omega_{p}\right)\\&=\frac{\varepsilon_{0}}{4}\chi^{(2)}:\mathbf{e}^{2}\left(r_{\perp},\omega_{p}\right)u_{p}^{2}e^{i2\beta_{p}z}.\end{aligned} \tag{2.34}$$

Replacing $\delta\mathbf{P}=\mathbf{P}^{(2)}$ in equation 2.32 one obtains the equation describing the propagation of the SH pulse when only SHG effects are considered:

$$\frac{du_{SH}}{dz}+i\left(\beta_{SH}-\beta_{0,SH}\right)u_{SH}=i\gamma_{SH}^{(2)}\frac{P_{0,p}}{\sqrt{P_{0,SH}}}u_{p}^{2}e^{i\Delta\beta z} \tag{2.35}$$

where $\Delta\beta$ is the mismatch coefficient as defined in equation 1.15 and the coefficient $\gamma_{SH}^{(2)}$ is defined as:

$$\gamma_{SH}^{(2)}=\omega_{SH}\frac{n_{g,p}\sqrt{n_{g,SH}}}{\sqrt{8A_{0}\varepsilon_{0}c^{3}}}\Gamma^{(2)}. \tag{2.36}$$

In equation 2.36 the term $n_{g,p}$ is the group index for the pump mode at frequency ω_{p} and the term $n_{g,SH}$ is the group index for the SH mode at frequency ω_{SH}, A_{0} is the waveguide area and the term $\Gamma^{(2)}$ is defined as:

$$\Gamma^{(2)}=\frac{\sqrt{A_{0}}\int_{A}\mathbf{e}\left(\mathbf{r}_{\perp},\omega_{p}\right)\chi^{(2)}:\mathbf{e}^{*}\left(\mathbf{r}_{\perp},\omega_{SH}\right)\mathbf{e}\left(\mathbf{r}_{\perp},\omega_{p}\right)dA}{\left(\int_{A}n^{2}\left(\mathbf{r}_{\perp},\omega_{p}\right)\left|\mathbf{e}\left(\mathbf{r}_{\perp}\omega_{p}\right)\right|^{2}dA\right)\left(\int_{A}n^{2}\left(\mathbf{r}_{\perp},\omega_{SH}\right)\left|\mathbf{e}\left(\mathbf{r}_{\perp},\omega_{SH}\right)\right|^{2}dA\right)^{\frac{1}{2}}} \tag{2.37}$$

where all the integral are evaluated over the whole area A of the plane orthogonal to the field propagation direction and $n\left(\mathbf{r}_{\perp},\omega_i\right)$ is the refractive index distribution in the plane A at frequency ω_i.

While not only SHG occurs in the waveguide, also the third order nonlinearities must be considered in the pulse equation. The term $\mathbf{P}^{(3)}\left(\mathbf{r},\omega_{SH}\right)$ can be derived from equation 1.6. While the SH pulse propagates, it is affected by the Self Phase Modulation (SPM) and Cross Phase Modulation (XPM). Since in the undepleted pump approximation the pump pulse is always much stronger than the SH pulse, the SPM term can be neglected, considering only the XPM term. In this case $\mathbf{P}^{(3)}\left(\mathbf{r},\omega_{SH}\right)$ can be written as:

$$\begin{aligned}\mathbf{P}^{(3)}\left(\mathbf{r},\omega_{SH}\right) &= 6\varepsilon_0\chi^{(3)}\vdots\left|\mathbf{E}_p.\left(\mathbf{r},\omega_p\right)\right|^2\mathbf{E}_{SH}\left(\mathbf{r},\omega_{SH}\right)\\ &= \frac{3}{4}\varepsilon_0\chi^{(3)}\vdots\left|\mathbf{e}\left(\mathbf{r}_{\perp},\omega_p\right)\right|^2\mathbf{e}\left(\mathbf{r}_{\perp},\omega_{SH}\right)\left|u_p\right|^2u_{SH}e^{i\beta_{SH}z}.\end{aligned} \tag{2.38}$$

Replacing $\delta\mathbf{P}=\mathbf{P}^{(3)}$ in equation 2.32 it becomes:

$$\frac{du_{SH}}{dz}+i\left(\beta_{SH}-\beta_{0,SH}\right)u_{SH}=2i\gamma^{(3)}_{SH,p}P_{0,p}\left|u_p\right|^2u_{SH}. \tag{2.39}$$

The coefficient $\gamma^{(3)}_{SH,p}$ is defined as:

$$\gamma^{(3)}_{SH,p}=\frac{3\omega_{SH}n_{g,SH}n_{g,p}}{4\varepsilon_0A_0c^2}\Gamma^{(3)}_{SH,p} \tag{2.40}$$

while the term $\Gamma^{(3)}_{SH,p}$ is defined as:

$$\Gamma^{(3)}_{SH,p}=\frac{A_0\int_A\mathbf{e}^*\left(\mathbf{r}_{\perp},\omega_p\right)\chi^{(3)}\vdots\mathbf{e}\left(\mathbf{r}_{\perp},\omega_{SH}\right)\mathbf{e}^*\left(\mathbf{r}_{\perp},\omega_{SH}\right)\mathbf{e}\left(\mathbf{r}_{\perp},\omega_p\right)dA}{\left(\int_An^2\left(\mathbf{r}_{\perp},\omega_{SH}\right)\left|\mathbf{e}\left(\mathbf{r}_{\perp},\omega_{SH}\right)\right|^2dA\right)\left(\int_An^{(2)}\left(\mathbf{r}_{\perp},\omega_p\right)\left|\mathbf{e}\left(\mathbf{r}_{\perp},\omega_p\right)\right|^2dA\right)} \tag{2.41}$$

Also in this case the integrals are evaluated over the whole A plane.

In addition, the contribution of the losses must also be taken into account. The term $\mathbf{P}_L\left(\mathbf{r},\omega_{SH}\right)$ is given by:

$$\begin{aligned}\mathbf{P}_L\left(\mathbf{r},\omega_{SH}\right) &= \varepsilon_0\delta\chi^{(1)}\mathbf{E}_{SH}\left(\mathbf{r},\omega_p\right)\\ &= \frac{1}{2}\varepsilon_0\delta\chi^{(1)}u_{SH}\mathbf{e}\left(\mathbf{r}_{\perp},\omega_{SH}\right)e^{i\beta_{SH}z}.\end{aligned} \tag{2.42}$$

where $\delta\chi^{(1)}$ is the perturbation of the first order susceptibility related to the losses. Replacing also here $\delta\mathbf{P} = \mathbf{P}_L$ in equation 2.32 it becomes:

$$\frac{du_{SH}}{dz} + i\left(\beta_{SH} - \beta_{0,SH}\right) u_{SH} = -\frac{\alpha_{SH}}{2} u_{SH} \tag{2.43}$$

where the term α_i is the loss coefficient of the mode at frequency ω_i:

$$\alpha_{SH} = -\frac{i\omega_{SH}\varepsilon_0}{2P_{0,SH}} \int_A \delta\chi^{(1)}\left(\mathbf{r}_\perp, \omega_{SH}\right) \left|\mathbf{e}^*\left(\mathbf{r}_\perp, \omega_{SH}\right)\right|^2 dA. \tag{2.44}$$

As shown in 2.44, the loss coefficient is related to the spatial distribution of $\delta\chi^{(1)}$ inside the waveguide, which in turn depends on the spatial distribution of the absorption coefficient determined by losses. However, since losses depend mainly on the fabrication imperfections, α_{SH} is typically extracted from experimental measurements.

Finally, the equation describing the SH pulse in the waveguide taking into account second order nonlinearities, third order nonlinearities and propagation losses can be derived by combining equation 2.35, 2.39 and 2.43:

$$\begin{aligned} &\frac{du_{SH}}{dz} + i\left(\beta_{SH} - \beta_{0,SH}\right) u_{SH} = \\ &\qquad = i\gamma^{(2)}_{SH} \frac{P_{0,p}}{\sqrt{P_{0,SH}}} u_p^2 e^{i\Delta\beta z} + 2i\gamma^{(3)}_{SH,p} P_{0,p} \left|u_p\right|^2 u_{SH} - \frac{\alpha_{SH}}{2} u_{SH}. \end{aligned} \tag{2.45}$$

Similarly to the SH pulse, to write the pump pulse equation one may consider the three terms separately. For the SHG contribution, according to equation 1.5 the term $\mathbf{P}^{(2)}\left(\mathbf{r}, \omega_p\right)$ can be written as:

$$\begin{aligned} \mathbf{P}^{(2)}\left(\mathbf{r}, \omega_p\right) &= 2\varepsilon_0 \chi^{(2)} : \mathbf{E}_{SH}\left(\mathbf{r}, \omega_{SH}\right) \mathbf{E}_p^*\left(\mathbf{r}, \omega_p\right) \\ &= \frac{1}{4}\varepsilon_0 \chi^{(2)} : \mathbf{e}\left(\mathbf{r}_\perp, \omega_{SH}\right) \mathbf{e}^*\left(\mathbf{r}_\perp, \omega_p\right) u_{SH} u_p^* e^{i\left(\beta_{SH} - \beta_p\right) z}. \end{aligned} \tag{2.46}$$

Substituting $\delta\mathbf{P} = \mathbf{P}^{(2)}$ in equation 2.32 for the SHG contribution one obtains:

$$\frac{du_p}{dz} + i\left(\beta_p - \beta_{0,p}\right) u_p = 2i\gamma_p^{(2)} \sqrt{P_{0,SH}} u_{SH} u_p^* e^{-i\Delta\beta z} \tag{2.47}$$

The term $\mathbf{P}^{(3)}\left(\mathbf{r},\omega_p\right)$ can be derived from equation 1.6. If the pump pulse is much stronger than the SH pulse, the SPM term is predominant over XPM term caused by the SH pulse. The result is then:

$$\begin{aligned}\mathbf{P}^{(3)}\left(\mathbf{r},\omega_p\right) &= 3\varepsilon_0\chi^{(3)}\vdots\left|\mathbf{E}_p\left(\mathbf{r},\omega_p\right)\right|^2\mathbf{E}_p\left(\mathbf{r},\omega_p\right)\\ &= \frac{3}{8}\varepsilon_0\chi^{(3)}\vdots\left|\mathbf{e}\left(\mathbf{r}_\perp,\omega_p\right)\right|^2\mathbf{e}\left(\mathbf{r}_\perp,\omega_p\right)\left|u_p\right|^2u_pe^{i\beta_pz}.\end{aligned} \tag{2.48}$$

Substituting $\delta\mathbf{P}=\mathbf{P}^{(3)}$ in equation 2.32 the result is:

$$\frac{du_p}{dz}+i\left(\beta_p-\beta_{0,p}\right)u_p=i\gamma^{(3)}_{p,p}P_{0,p}\left|u_p\right|^2u_p. \tag{2.49}$$

The pump pulse is also affected by the propagation losses in the following way:

$$\frac{du_p}{dz}+i\left(\beta_p-\beta_{0,p}\right)u_p=-\frac{1}{2}\alpha_pu_p. \tag{2.50}$$

Joining equations 2.47, 2.49 and 2.50 it is possible to obtain the general equation for the pump pulse:

$$\begin{aligned}&\frac{du_p}{dz}+i\left(\beta_p-\beta_{0,p}\right)u_p=\\ &\quad=2i\gamma^{(2)*}_p\sqrt{P_{0,SH}}u_{SH}u^*_pe^{-i\Delta\beta z}+i\gamma^{(3)}_{p,p}P_{0,p}\left|u_p\right|^2u_p-\frac{1}{2}\alpha_pu_p.\end{aligned} \tag{2.51}$$

By Fourier-transforming equations 2.45 and 2.51, a system of coupled equations that describes the spatial and temporal evolution of the pump and SH pulse amplitudes $u_p\left(z,t\right)$ and $u_{SH}\left(z,t\right)$ can be derived:

$$\begin{cases}\frac{du_{SH}}{dz}+\sum_{m\geq1}\frac{(i)^{m-1}\beta_{SH,m}}{m!}\frac{\partial^mu_{SH}}{\partial t^m}=\\ =i\gamma^{(2)}_{SH}\frac{P_{0,p}}{\sqrt{P_{0,SH}}}u_p^2e^{i\Delta\beta z}+2i\gamma^{(3)}_{SH,p}P_{0,p}\left|u_p\right|^2u_{SH}-\frac{\alpha_{SH}}{2}u_{SH}\\ \frac{du_p}{dz}+\sum_{m\geq1}\frac{(i)^{m-1}\beta_{p,m}}{m!}\frac{\partial^mu_p}{\partial t^m}=\\ =2i\gamma^{(2)*}_p\sqrt{P_{0,SH}}u_{SH}u^*_pe^{-i\Delta\beta z}+i\gamma^{(3)}_{p,p}P_{0,p}\left|u_p\right|^2u_p-\frac{\alpha_p}{2}u_p\end{cases} \tag{2.52}$$

where $\Delta\beta=\beta_p-\beta_{SH}$ and $\beta_{i,m}$ identify the m*th* mode related to the Fourier transformation. Equations 2.52 describes the complete propagation of optical

pulses. This system of equations can be simplified by neglecting third-order nonlinearities and the effect of losses. Moreover in the continuous-wave approximation, it is possible to neglect the terms with time derivatives. In this way the equation describing the propagation of the SH pulse can be simplified:

$$\frac{du_p}{dz} = i\gamma_{SH}^{(2)} \frac{P_{0,p}}{\sqrt{P_{0,SH}}} u_p^2 e^{i\Delta\beta z}. \tag{2.53}$$

The pump power is therefore not affected by the generation of the SH pulse and $u_p(z) \sim const$. This is called undepleted pump approximation [3]. Assuming also that $\gamma_{SH}^{(2)}$ is constant along z, that is typically valid except in the situation where a periodically poling is used, in equation 2.53 only the exponential term shows a dependence from z [4]. Integrating over all the waveguide length the total SH power is:

$$P_{SH} = P_{0,SH} |u_{SH}|^2 = P_p^2 \left|\gamma_{SH}^{(2)}\right|^2 L^2 sinc^2\left(\frac{\Delta\beta L}{2}\right). \tag{2.54}$$

This is the most common way to express the SH power in the continuous-wave and in the undepleted pump approximations. It shows that the SH power quadratically depends on both the pump power P_p and the waveguide length L. Moreover, the SH power depends quadratically also on the second order nonlinear coefficient $\gamma_{SH}^{(2)}$ that, as shown in equations 2.36 and 2.37, is directly proportional to $\chi^{(2)}$. SH power depends also on the squared cardinal sine of $\frac{\Delta\beta L}{2}$: if $\Delta\beta = 0$, perfect phase matching condition, there is the maximum of the generation. As $\Delta\beta$ increases the generation efficiency decreases.

2.4 Intermodal phase matching condition

As explained in Section 1.2.3, in the SHG process phase matching condition is required. The phase matching condition in equation 1.15 is obtained if [30]:

$$n_{eff,p} = n_{eff,SH}. \tag{2.55}$$

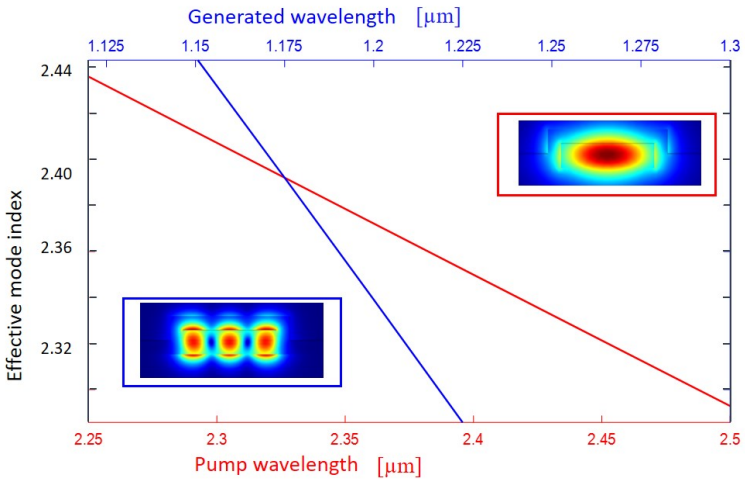

Figure 2.4: Process used to find the intermodal phase matching condition. The red curve shows the dispersion of the effective refractive index for a TE1 mode between $\lambda_p = 2.25$ and $\lambda_p = 2.5$ μm wavelength, while the blue curve shows the dispersion of the effective refractive index for a TM3 mode at $\lambda_{SH} = \lambda_p/2$ wavelength for the same geometry. The phase matching condition for this geometry of the waveguide is reached at $\lambda_p = 2.34$ μm, where the two lines cross and the condition $n_{eff,p} = n_{eff,SH}$ is satisfied.

This condition is hard to satisfy with pump and SH signals propagating on the same modal order because of the refractive index dispersion. The problem can be overcame by using pump and SH waves propagating on different modal orders. This method is commonly known as intermodal phase-matching [31]. In the intermodal phase matching the width of the waveguide w is chosen to have phase-matching for given combinations of pump and SH modal orders. In this work the modal combination will be chosen in order to have phase matching condition around 2.2 μm. This wavelength has been chosen for two reasons: first at this wavelength Two Photon Absorbtion in silicon, that will compete with SHG, is negligible [32], second using a pump wavelength above 2.2 μm allows to generate a SH signal above 1.1 μm, in the transparent spectral region of silicon. In figure 2.4 is shown an example of waveguide engineering process. The red curve shows the dispersion of the effective refractive index for a TE1 mode between $\lambda_p = 2.25$ μm and $\lambda_p = 2.5$ μm wavelength. The blue curve shows the dispersion of the effective refractive index for a TM3 mode at $\lambda_{SH} = \lambda_p/2$ wavelength for the same geometry. The pump and the SH dispersion curves cross at $\lambda_p = 2.34$ μm, where $n_{eff,p} = n_{eff,SH}$ and the phase matching condition is satisfied. The insets of the figure show the simulated profiles of the pump and SH mode. This values are obtained by using the Electromagnetic Module of the COMSOL Multiphysics® FEM software. The effective refractive index depends on the geometry of the waveguide and so the phase matching condition also strongly depends on the geometry of the waveguide.

Equation 2.54 shows that the generated power depends on $\left|\gamma^{(2)}\right|^2$ with $\gamma^{(2)}$ defined as in equation 2.36. This in turn leads to the fact that P_{gen} is proportional to $\left|\Gamma^{(2)}\right|^2$. In order to determine $\left|\Gamma^{(2)}\right|^2$ it is necessary to know the spatial distribution of the tensor $\chi^{(2)}$ in the waveguide. However, it is also possible to define a parameter quantifying the SHG strength taking into account only the overlap between the pump and the SH modes. Considering $\chi^{(2)}$ spatially constant, $\Gamma^{(2)}$ becomes:

$$\Gamma^{(2)} = \chi^{(2)} K \tag{2.56}$$

where the adimensional parameter K is defined as

$$K = \frac{\sqrt{A_0}\int_A e_x\left(\mathbf{r}_\perp,\omega_p\right) e_k^*\left(\mathbf{r}_\perp,\omega_{SH}\right) e_x\left(\mathbf{r}_\perp,\omega_p\right) dA}{\left(\int_A n^2\left(\mathbf{r}_\perp,\omega_p\right)\left|e_x\left(\mathbf{r}_\perp,\omega_p\right)\right|^2 dA\right)\left(\int_A n^2\left(\mathbf{r}_\perp,\omega_{SH}\right)\left|e_k\left(\mathbf{r}_\perp,\omega_{SH}\right)\right|^2 dA\right)^{\frac{1}{2}}}. \tag{2.57}$$

This equation considers a TE polarized pump field and a SH field polarized along a direction k that can be either x or y. The coefficient K describes the overlap between the pump and the SH modes. For a spatially constant $\chi^{(2)}$, the SHG conversion efficiency is proportional to K. It is now possible to define an effective second order susceptibility $\chi^{(2)}_{eff}$ as:

$$\chi^{(2)}_{eff} = \left|\frac{\Gamma^{(2)}}{K}\right|. \tag{2.58}$$

This quantity can be interpreted as the equivalent spatially constant $\chi^{(2)}$ that would have given the same SHG efficiency.

2.5 The experiment

To be able to control SHG in silicon waveguides, one needs to first understand the origin of this process. As explained in section 1.4, two are the possible causes: the strain, that can break the centrosymmetry of the silicon crystalline structure, and the presence of charged defects at the interface between the silicon waveguide and the stressing layer that generate a dressed $\chi^{(2)}$. The aim of this experiment is to perform a SHG measurement that allow to separate the two different processes to understand the effects of each one of them. The sample is a strain silicon waveguide with intermodal phase matching condition.

To investigate the effect of the strain, SHG is studied under an external mechanical load. A screw-equipped sample holder as the one shown in figure 2.5 is used. Rotating the screw it is possible to apply a variable vertical load orthogonal to the main plane of the sample in its center, while the sample edges are fixed. This load allows to set a tunable strain inside the waveguide.

To control the effect of the charge defects at the interfaces of the waveguide, the method described by Piccoli et al. [33] was used. In this work the

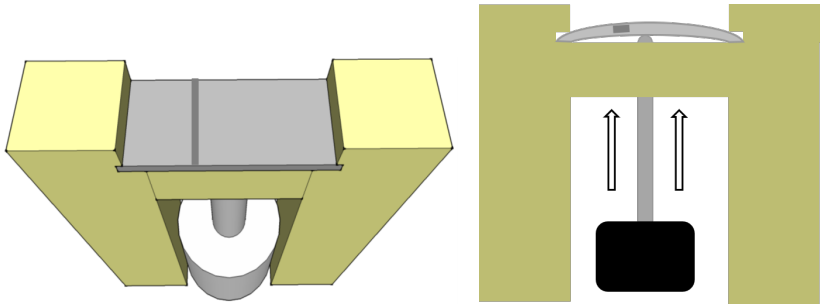

(a) (b)

Figure 2.5: Sketch of the screw-equipped sample holder. The total width of the sample holder is 6 mm and the screw is in the center. The screw introduces a displacement ΔH in the center of the sample while the edges are fixed. The analyzed waveguide is located 0.9 mm from the center.

authors performed C-V measurements at 10 KHz on different samples that have been exposed to 254 nm UV light from a Hg bulb lamp [34, 35]. The exposure times varied from 1 minute up to 32 hours. In this way they show that it is possible to neutralize the effective charge density in the stressing layer.

2.5.1 Setup

The experimental setup to measured SHG is composed by four different parts:

- the source: it is a Ti:sapphire laser with two different amplification stages cascaded. The Ti:sapph laser (Spectra-Physics Tsunami®) is a solid state 4 levels laser. The active medium of the Tsunami is a titanium doped sapphire crystal, that has an absorption band between 400 nm and 600 nm and an emission band between 670 nm and 1000 nm. The Ti:S is optically pumped by a 4 W laser at 532 nm long wavelength (Spectra-Physics Millennia®) and can operate both in a mode-locked condition, using an acousto-optic modulator, as well as in a quasi Continuous-Way (CW) condition. During this experiment the laser operates in a mode-locked condition with a bandwidth of 70 nm around a central wavelength of 800 nm. Its repetition rate is 82 MHz with pulse duration $\delta_t = 35$ fs. The beam of the laser is then amplified by the two amplification stages. The first stage of amplification is a regenerative amplifier (Spectra-Physics Spitfire Pro System®). It is a

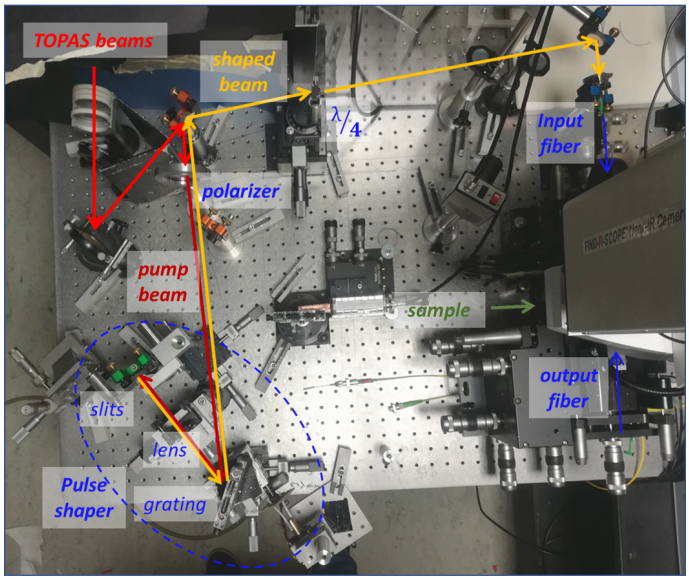

(a)

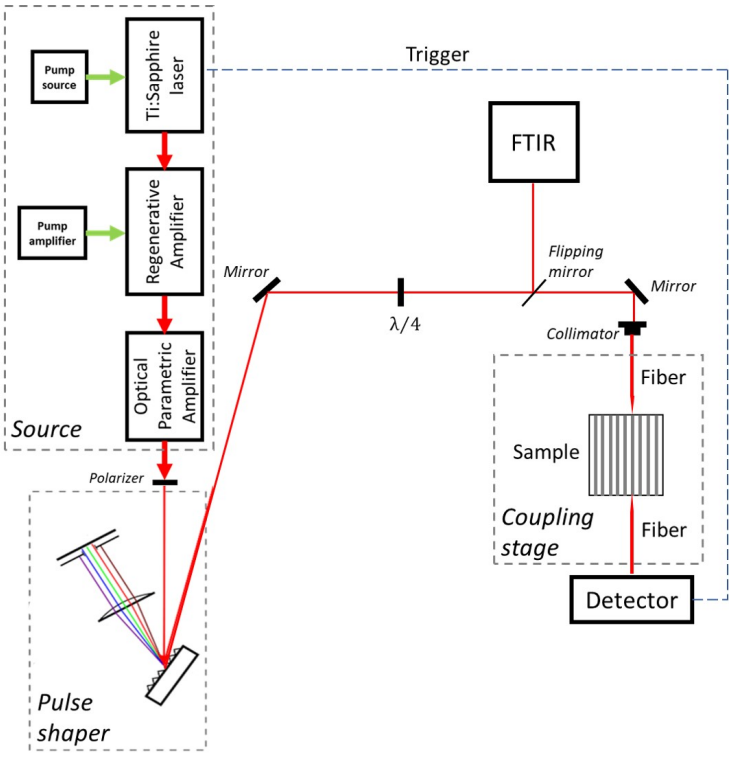

(b)

Figure 2.6: Experimental setup for SHG measurements. The sources and the detectors are not visible in the photo.

solid state amplifier that overcomes the optical damage threshold of the crystalline material by using the chirped pulse amplification method (see the appendix for further information). At the output of the amplifier, an average power above 3W is measured, with 1 kHz repetition rate. The second amplification stage is a nonlinear stage composed by an optical parametric amplifier (Light Conversion TOPAS-C®). Here the amplified beam at 800 nm is divided in two arms. The first arm is directed onto a sapphire plate and generates a supercontinuum signal in the range between 1.14 μm and 1.6 μm. The signal thusly generated is then mixed with the second arm of the amplified signal in a nonlinear crystal. Here two beams are generated through DFG process. These generated beam wavelengths can be tuned by changing the orientation angle of the crystal. The lower wavelength beam is named signal beam and can be tuned in the range from 1.4 μm to 1.6 μm, while the higher wavelength beam is named idler beam and can be tuned in the range from 1.6 μm to 2.6 μm. The signal and the idler have linear orthogonal polarization, so they can be easily separated using a polarizer. In this experiment, the idler signal is used as pump beam. Therefore, this stage can act as a tunable mid-infrared light source. The total average power emitted by the OPA is 600 mW with a peak power of $\sim$ 7 GW. This power, if directly coupled in a waveguide, will burn the input facet. The damage threshold of this kind of structure is not known exactly but the damage threshold for the crystalline silicon in air for $\lambda = 2200$ nm and a pulse width of 0.66 ps is 0.18 j/cm^2 [36]. A pulse shaping-stage is therefore needed before the input in the sample to prevent any problem. This additional stage cuts the pump pulse spectrum, determining a temporal enlargement of the pulse width and a peak power reduction. Moreover, the pump pulse spectral width reduction allows to better match the wavelength range over which the phase-matching condition is satisfied.

- The pulse-shaping stage: while $\Delta t \Delta\omega = 4ln2$ [37], a pulse can be temporally tailored by shaping its spectrum. In this setup the pulse-shaper work in a $4f$ configuration [38], as shown in figure 2.7. The pulse first arrives onto a diffraction grating, that separates its different spectral

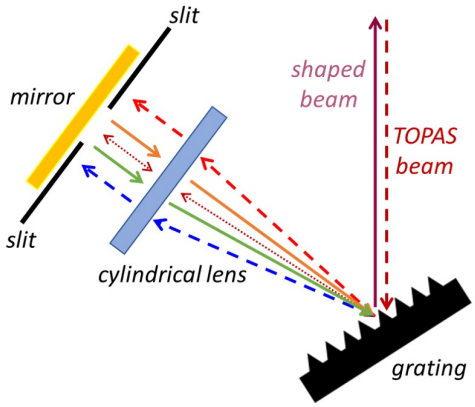

Figure 2.7: Sketch of the pulse-shaper. The shaped beam is temporally enlarged and spectrally squeezed.

components. Then a cylindrical lens transforms the angular dispersion of the pulse in spatial dispersion, making it possible to use tunable slits to selected only a portion of the frequency components. The selected frequencies are then reflected back by a mirror and focused on the grating by the lens, so that a collimated beam is created again. It is possible to modify manually the aperture of the slits to change the width of the pulse at the output of the pulse-shaper. In our experiment the beam is cut from 253 nm to 14 nm. In addition, an automatic rotation system placed below the diffraction grating is used to tune the central wavelength of the final pulse to allow to do measurement scanning the pump wavelength. This mechanism, with an additional stage of neutral filters, allows to couple the pump signal to the sample without risks for the sample associated to the high peak power. The neutral filters are also used to set the desired pump power for the experiment.

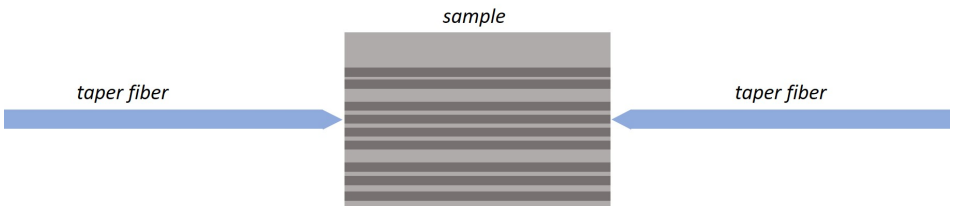

Figure 2.8: Sketch of the butt coupling stage: two identical taper fibers are used to inject/collect the signal in/from the sample.

- The coupling stage: the light is coupled in the sample via butt coupling. The pulse arrives in a collimator that couples light into a tapered lensed optical fiber. This fiber is used to inject the light in the input facet of the sample waveguide. A second identical fiber is used to collect the light that comes out from the output facet of the sample waveguide. Both the fibers are mounted on piezoelectric controlled flexure stages, in order to guarantee the best coupling between fibers and sample. An half waveplate is placed before the collimator of the input fiber to select the proper polarization to couple into the waveguide. The waveguides analyzed in this section support only the TE polarization for the MIR wavelengths used as pump, so the half waveplate is set in order to maximize the pump signal transmitted by the waveguide. Before the pulse is coupled in the waveguide, a flipping mirror allows to monitor it by performing a scan with the FTIR spectrometer. The setup is also equipped with a 1550 nm wavelength Amplified Stimulated Emission (ASE) laser. Since the NIR-VIS camera (FIND-R SCOPE-85700®) is not sensitive to MIR wavelengths, the ASE source is used for the first rough alignment of the two fibers with the waveguide sample. The use of the two fibers for the coupling guarantees the collinearity of the ASE beam with the pump beam. This allows to do the first coupling of the pump beam with the ASE source, and then to maximize the TOPAS signal using an extended InGaAs photodiode (Thorlabs FD05D®) with a responsivity between 800 nm and 2600 nm.

- The detection stage: the pump power transmitted by the waveguide is checked by the extended InGaAs photodiode. The source is pulsed, so a lock-in amplifier triggered by the pump signal is used to synchronize the detection with the pulses in order to improve the signal sensitivity, which can be set around 200 pW. To detect the SH signal, the situation is more challenging. For these waveguides the SH signal is expected to be at the fW level [4], therefore a photon counting technique is needed to detect it. An InGaAs Single Photon Avalanche Diode (SPAD ID-Quantique-ID201®) with an efficiency in the range from 10% to 20% in a wavelength between 1150 nm and 1200 nm is used. Also in this case a triggered configuration is used and is possible to set manually

the detection window duration. The gating time is set using a side effect of the pump signal, that it is detected by the SPAD via TPA process. By bending the collection fiber is then possible to filter out the pump. Indeed, the fibers are single mode around 1550 nm and do not guide well the MIR wavelengths. So bending the fiber lets the pump signal to escape and being extinguished without affecting the SH signal, that is well guided in the fiber. To be sure that the pump is extinguished is used another time the side effect of the SPAD: the fiber is bent manually since the signal is covered by the noise. The average power P_{SH}, at λ_{SH} wavelength, collected by the SPAD can be evaluated as:

$$P_{SH} = \frac{hc}{\lambda_{SH}} \frac{C - C_{dc}}{DE} \tag{2.59}$$

being c the light speed, h the Planck constant, C the detected counting rate, C_{dc} the dark count of the SPAD and DE the detection efficiency. The SHG signal can also be spectrally analyzed using a scanning monochromator realized with a diffraction grating in a double-pass configuration. This monochromator is placed between the collection fiber and the detector.

2.5.2 The sample

The devices are fabricated in *Fondazione Bruno Kessler* on a 6′ SOI wafer, with a 243 nm thick silicon layer deposited on a 3 μm thick BOX. The design was performed by dott. Claudio Castellan. A 365 nm UV lithography is used to define the waveguides, which are realized in a second moment by using reactive ion etching. On the top of the waveguides a 140 nm thick SiN cladding is conformally deposited by LPCVD. This induce a tensile stress in the silicon waveguide, estimated around 1.25 GPa via wafer bow measurement. This tensile stress deforms the crystalline structure of the whole waveguide in a non uniform way as shown in figure 2.9(b), breaking the silicon centrosymmetry. The height of the SiN layer corresponds to the maximum value reachable before cracking the wafer. A 2D map of the displacement of the strain in the cross section waveguide is shown in figure 2.10. In the same chip are

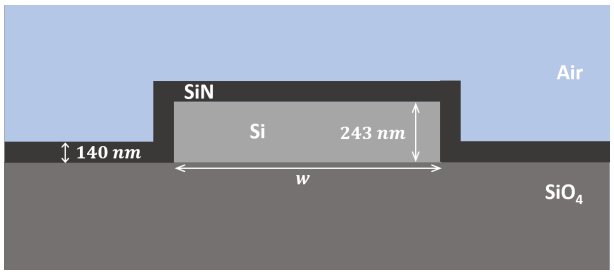

(a)

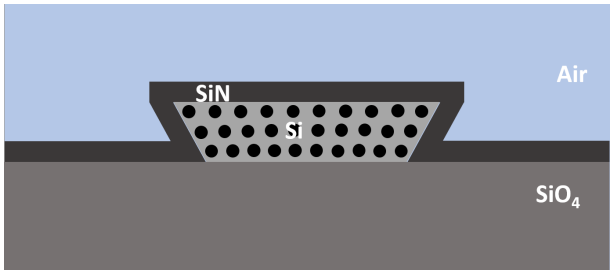

(b)

Figure 2.9: (a) cross section of the studied waveguides. The parameter w is used to phase-match different pump wavelengths in different designs of the waveguides; (b) sketch of the effect of the tensile stress on the crystalline structure of the silicon waveguide core.

present different designs of waveguides with different widths. All the different widths are properly selected to introduce intermodal phase-matching between the TE1 pump mode and TM3 SH mode at different pump wavelength [4]. A typical waveguide cross-section is sketched in figure 2.9(a). The losses for the pump mode have been evaluated via the cut-back method and are 9 dB per facet for a waveguide width $w \sim 1$ μm. The losses for the SH mode are evaluated as in 2.44 and are 15.5 dB per facet for a 1 μm wide waveguide [4].

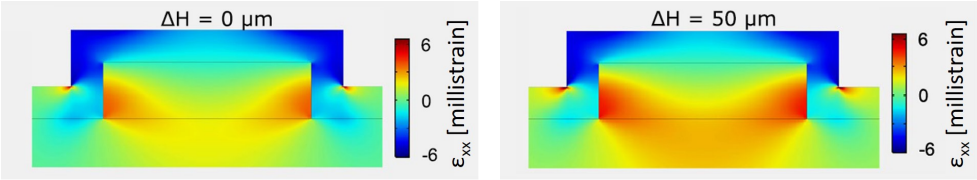

(a) (b)

Figure 2.10: (a) 2D map displacement of the strain given by the SiN stressing layer in the cross section waveguide (b) 2D map of the displacement of the strain in the cross section waveguide when a displacement of 50 μm is applied to the sample by using the screw. Simulation performed by Claudio Castellan.

As previously explained, the origin of SHG is not clear but these samples have been designed assuming that SHG can be entirely attributed to strain. Berciano et al. in 2018 [39] measured an electro-optic effect in a strained waveguide and attributed it to Pockels effect. They fitted the experimental data with the theoretical model reported in [40] with parameters connecting the $\chi^{(2)}$ to strain gradient. Assuming that these parameters can be used also for SHG, the $\chi^{(2)}$ distribution inside the waveguide can be estimated using the coefficients reported by Damas et al. [40] and evaluating the strain gradient with a FEM simulation, as reported by Castellan [4]. In this work, the waveguides are designed to phase-match the TE1 pump mode and the TM3 SH mode. The waveguide cross section is on the xy plane and the waveguide longitudinal axis is the z axis. The tensor element that is involved in this generation is $\chi^{(2)}_{strain\,xxy}$ and can be evaluated as [40]:

$$\chi^{(2)}_{strain\,xxy}(\phi) = \Gamma_{xxy,xxy}\eta_{xxy}(\phi) + \Gamma_{xxy,yyy}\eta_{yyy}(\phi) \tag{2.60}$$

where ϕ is the crystallographic axis along which the waveguide is oriented, $\phi = 0$ in this work, $\eta_{mnl} = d\varepsilon_{mn}/dx_l$ are the strain gradient components and $\Gamma_{ijk,mnl}$ are coefficients that depend on the semiconductor. For a waveguide of width $w = 900$ nm the avarange value of $\chi^{(2)}_{strain\,xxy}$ is 1.75 pm/V [4, 41]. Using equation 2.37 it is also possible to evaluate $\left|\Gamma^{(2)}\right| = 0.47$ fm/V, that corresponds to an effective second order nonlinearity $\chi^{(2)} = 0.13$ pm/V [4]. This is the constant value of $\chi^{(2)}$ that would give the same $\Gamma^{(2)}$ that can be extracted by the model described in [40, 39].

2.5.3 Investigating the strain

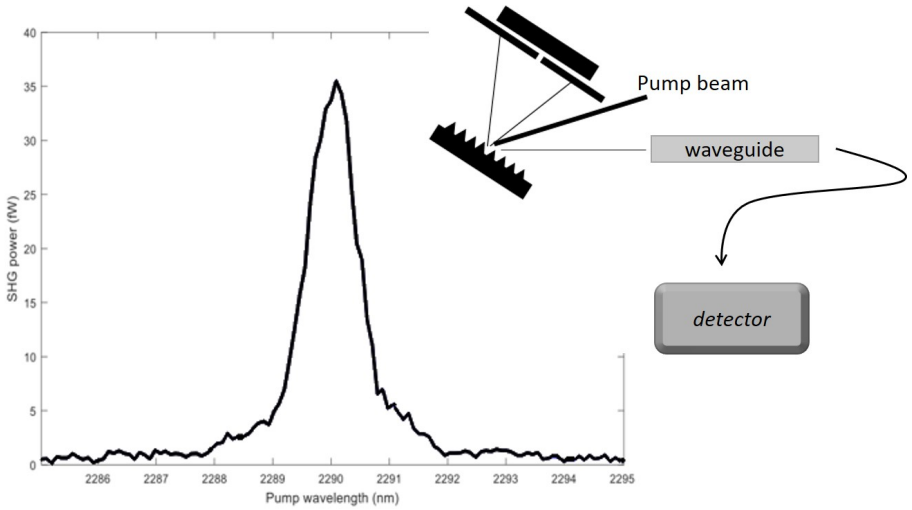

Figure 2.11: On-chip SH power as a function of the pump wavelength for a 11 mm long waveguide of width $w = 906$ nm. The pump wavelength is scanned using a reflection grating rotated with an automatic system. The detector used for this kind of measurement is the ID-Quantique-ID201®.

A first set of measurements have been performed in order to investigate the behavior of the sample. The spectrum of the generation efficiency of SH as function of the pump wavelength λ_P shows a single peak at $\lambda_P \sim 2290$ nm, as shown in figure 2.11. This is the first proof of the SHG occurrence, as it occurs only at the wavelength that provides phase-matching condition. The spectral analysis of the SH pulse has also been performed and is shown in figure 2.12. These measurements have been performed fixing the pump wavelength at the maximum of the generation and scanning the generated

wavelength at the output of the sample around the expected SH wavelength $\lambda_{SH} = \lambda_P/2$. Here it is visible how by changing the width of the sample also the wavelength of the peak changes, showing the strong dependence of the phase-matching condition from the geometry of the sample. A 2D map of the SH generated power as function of λ_P and λ_{SH} is reported in figure 2.13. The tolerance of the phase-matching condition respect to the pump wavelength is 2 nm, as expected from the simulation performed during the design [4], and is always respected the condition $\lambda_{SH} = \lambda_P/2$.

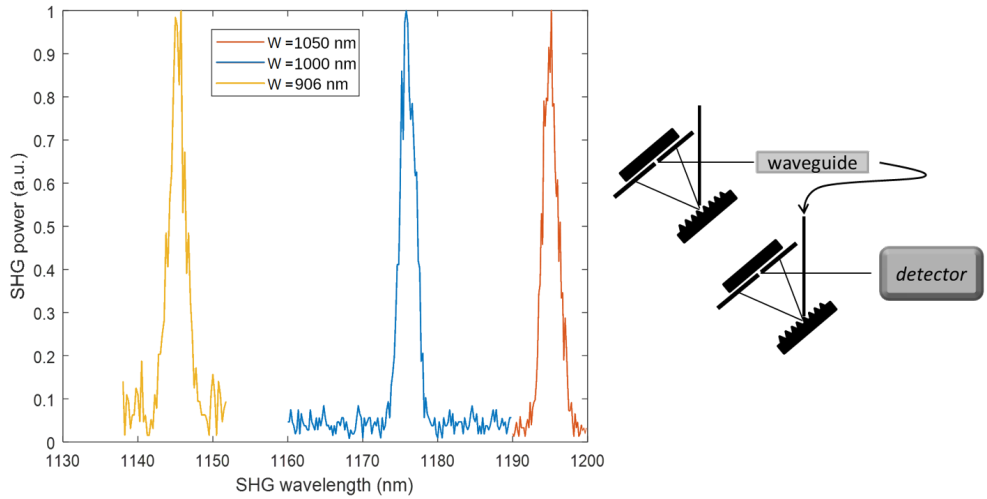

Figure 2.12: Spectral analysis of the SH pulse. First the proper pump wavelength λ_P is set and then a spectrum around $\lambda_{SH} = \frac{\lambda_P}{2}$ is performed. Notice that a different width of the sample correspond to a different peak wavelength, as the phase-matching condition is different.

The behavior of the SHG as function of the pump power has also been investigated. In figure 2.14 it can be observed that the SHG power scales in a quadratic way with the pump power, as expected from equation 2.54.

The results presented so far show that we observed SHG, but they do not offer any proof on the origin of the nonlinearity causing this generation. The aim of the following experiment is to investigate the source of this induced $\chi^{(2)}$. To achieve this goal, the same experiment described previously has been carried out on a 4 mm long waveguide with a width of 906 nm using the screw-equipped sample holder. The tensile stress introduced by the SiN stressing layer sets the initial strain conditions ($\Delta H = 0$) which is then

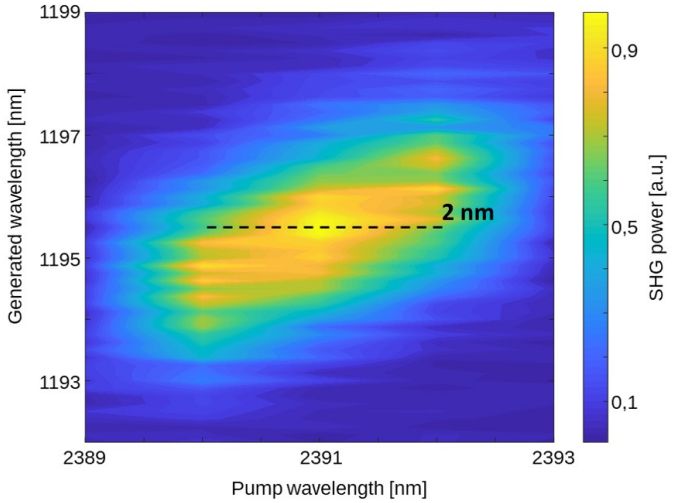

Figure 2.13: Map of the SHG power as function of λ_P and λ_{SH} for a 4 mm long waveguide with $w = 1050$ nm of width. First λ_P is set and a measurement scanning λ_{SH} is performed, then λ_P is moved in a new position and a new scan of λ_{SH} is performed. The condition $\lambda_{SH} = \lambda_P/2$ is always respected and the waveguide shows a generation band of 2 nm, as expected from simulations.

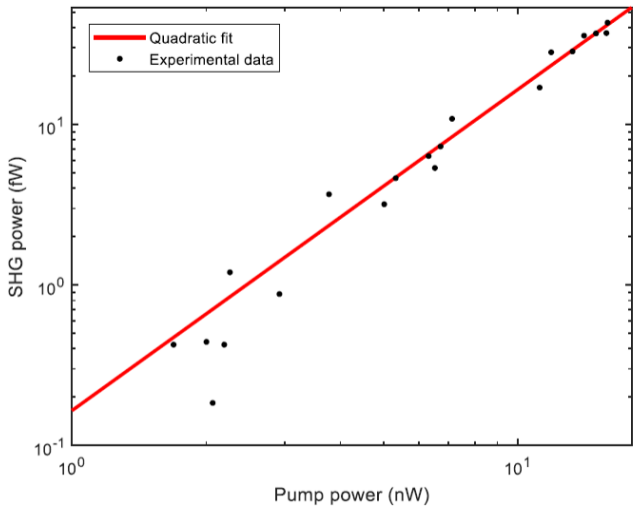

Figure 2.14: SHG power dependence from the pump power for a waveguide 4 mm long and 1050 nm wide in a *log-log* scale. As expected from equation 2.54, SHG power scales in a quadratic way with the pump power.

increased by rotating the screw. The results are shown in figure 2.15. Increasing the load in the sample results in a shift of the peak. Indeed, increasing the strain in the sample induces a change in the effective index by the photoelastic effect, and this leads to a change in the phase-matching condition. However, despite this shift in the peak wavelength, the SH power is always the same, revealing that the value of $\chi^{(2)}$ is not increasing with the strain [41].

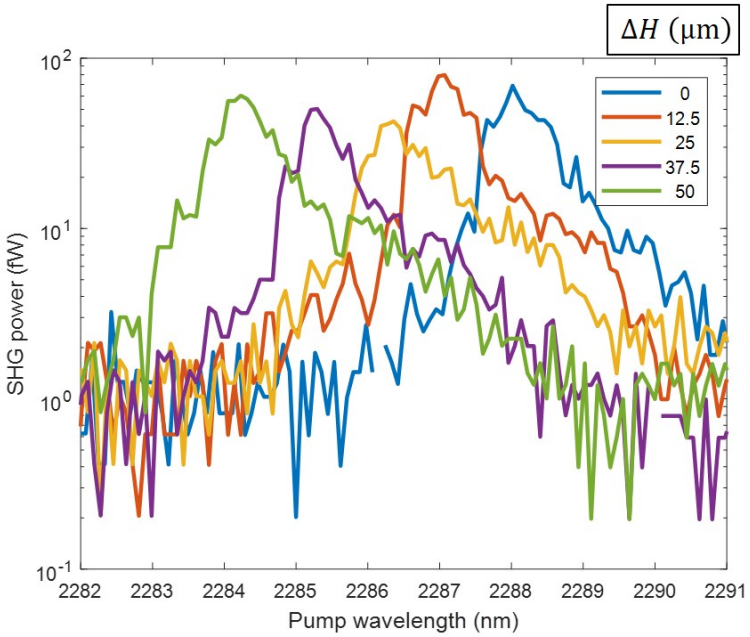

Figure 2.15: Measurements on a 4 mm long and 906 nm wide waveguide for five different values of the displacement ΔH induced by the screw in the center of the sample. Due to the different phase-matching conditions in the various measurements the peak's wavelength is shifted, but the SHG power is the same.

2.5.4 From the experiment to $\chi^{(2)}$ estimation

In order to evaluate the $\chi^{(2)}$ inside the waveguide, a uniform distribution of it in the waveguide cross section is assumed. In this situation $\Gamma^{(2)} = \chi^{(2)} K$, as in equation 2.56. This is true for small value of $\Gamma^{(2)}$, in which the SH pulse does not affect the pump pulse. In this situation, neglecting dispersion and phase-modulation, the solution of 2.52 has a simple solution of the form $u_{SH} = \Gamma^{(2)}$ [4]. The quantity known in the experiment is P_p and the quantity measured in the experiment is $P_{SH} = P_{0,SH} |u_{SH}|^2$, that depends only on the modulus

of $\Gamma^{(2)}$ and not on its phase. So, considering the typical powers of the experiment shown so far, $\Gamma^{(2)}$ can be considered as an input parameter of a numerical model to solve 2.56.

Using the model reported in [4], it is possible to obtain the average SH power as a function of both the pump average power and the second order nonlinear coefficient $\left|\Gamma^{(2)}\right|$, as shown in figure 2.16. While in the experiment all the parameter used in the model can be estimated, except $\left|\Gamma^{(2)}\right|$, it can be useful to invert the plot, as in figure 2.17, reporting $\left|\Gamma^{(2)}\right|$ as function of the pump and the SH powers. Finally it is possible to obtain $\chi^{(2)}_{eff}$ using equation 2.58.

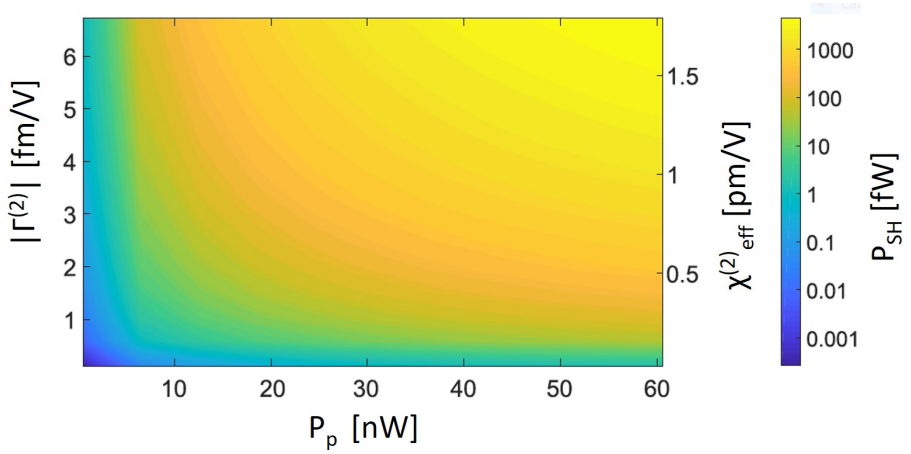

Figure 2.16: Average SH power as function of the pump and $\left|\Gamma^{(2)}\right|$ for a 900 nm wide and 5 mm long waveguide with a pulse duration of 5 ps and propagation losses of 8 dB/cm for both the pump and the SH pulses. On the right axis it is also reported the value of $\chi^{(2)}_{eff}$ that correspond to the $\left|\Gamma^{(2)}\right|$ reported in the left axis. Image of courtesy by Claudio Castellan.

2.5.5 Investigating the electric field

The second possible cause of the SHG can be the electric field generated by the charge defects at the interface between the silicon and the silicon nitride stressing layer. In the ideal bonding condition of SiN, silicon has four nitrogen atoms as neighbors, while nitrogen has three silicon atoms as neighbors. As the lattice step and the chemical composition of the two materials are dif-

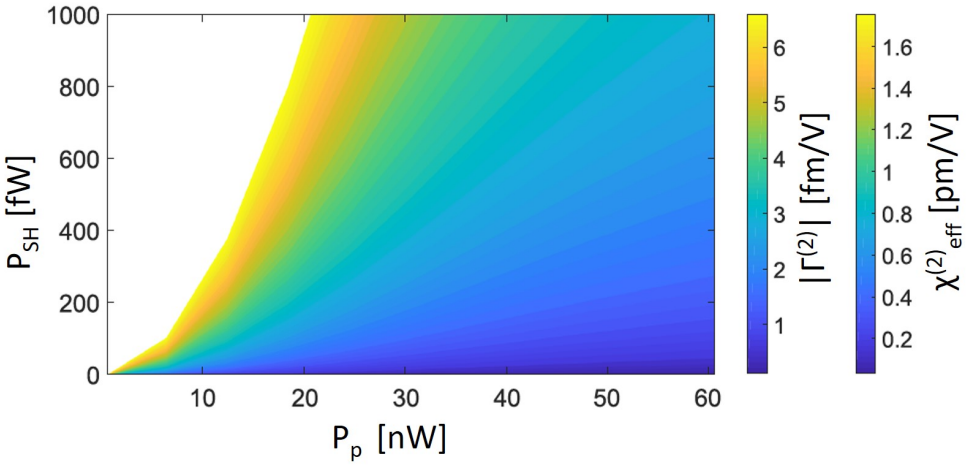

Figure 2.17: Second order nonlinear coefficient as a function of the pump average power and the SH average power obtained by inverting the plot 2.17 . Image of courtesy by Claudio Castellan.

ferent, during the deposition of the SiN on the top of the silicon waveguide a formation of defects can occur [42, 43]. The most common defects are are the *K center* and the *N center*, defects (left and right sketches in figure 2.18 respectively). The *K* center is formed by a silicon atom bound by three nitrogen atoms and a dangling bond. The *N* center is formed by a nitrogen atom bound by two silicon atoms and a dangling bond. The most significant defect that occurs during this LPCVD deposition is the *K* center [33]. It may assume three different charge states: the positive state K^+ where there are no electrons in the dangling bond, the neutral state K^0 where there is one electron in the dangling bond, and the negative state K^- where there are two electrons in the dangling bond [44]. The most thermodynamically favorable charge state is the K^+ center [45]. These positive defects at the interfaces of the silicon waveguide create an electric field E_{DC} in the core of the waveguide itself, that interacts with the high third order nonlinear coefficient $\chi^{(3)}$ of the bulk silicon creating an effective (dressed) $\chi^{(2)} = 3\chi^{(3)}E_{DC}$. This process is called Electric Field Induced Second Harmonic (EFISH), and it is a third order nonlinear process that occurs when the nonlinear polarization vector $P^{(3)}$ acquires terms at frequencies $2\omega_1$ and $2\omega_2$, and can be seen as a SHG process [27].

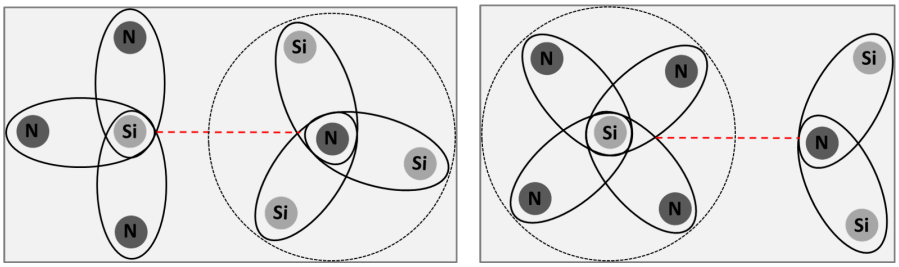

(a) (b)

Figure 2.18: (a) sketch of the K center defect: the silicon atom establishes a dangling bond with an electronically complete nitrogen atom; (b) sketch of the N center defect: the nitrogen atom establishes a dangling bond with an electronically complete silicon atom.

To understand the role of EFISH in the measurements described so far, it is useful try to remove these K^+ center defects. This can be done by irradiating the sample with UV light. This process annihilates the positive centers with the charges of the free electrons present in the core of the waveguide, neutralizing them in K^0 center defects.

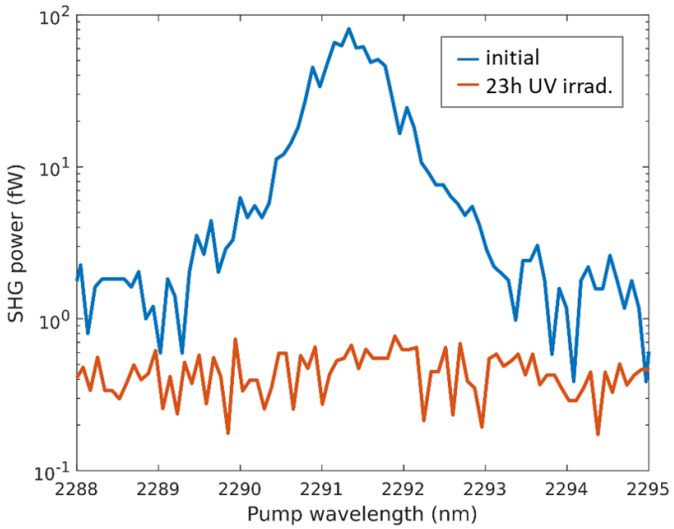

Figure 2.19: Spectral analysis of the SH peak before the UV exposure and after 23h of irradiation. After the UV irradiation the peak disappears completely.

The same measurement shown so far has been done on the same sample before and after the UV irradiation. In figure 2.19 is shown the spectral anal-

ysis of the SH peak in the two situation. After the UV irradiation the SHG signal is completely suppressed. This result clarifies that the origin of the SH in silicon waveguide is not due to the strain but by the presence of charge defects, showing that SHG disappears when dangling bonds are passivated. Any effect different from EFISH that can induce a $\chi^{(2)}$ in the material is below the noise level of the experiment, that is 0.5 fW. So it is possible to set the upper limit of the strain induced $\chi^{(2)}$ at 0.05 pm/V. This value is also supported by a theoretical evaluation of Khurgin et al. [46].

From this situation, the external load has been applied again, to see if it is possible to increase the induced $\chi^{(2)}$ only increasing the strain in the waveguide. Rotating the screw the peak appears again but with a lower power, as shown in figure 2.20. Similar to the previous measurements, the peak is blue-shifted with respect to the one measured in the original waveguide. When the strain is removed, the peak is shifted back to its original position, since the strain is removed and the strain-induced refractive index change vanishes, but the SHG magnitude remains however the same. If this SHG signal were due to strain, it is expected to disappear. Therefore, one may conclude that this peak can not be due to the strain. Moreover, it can be removed with 4 hours of UV irradiation. So, the most probable interpretation of this fact could be the re-activation of defects due to a mechanical break of the dangling bonds, that are weaker respect to covalent bonds [47]. This also explain why the power is lower: it is a mechanical break given by the thin deformation of the surface under the external load.

For sake of completeness also C-V measurements to estimate the charge density were carried out following [33]. In a first moment a simplified version of the device, that is shown in figure 2.21, where waveguides are defined has been studied. Waveguides are defined on a SOI wafer, which possesses a SiO2 layer between the waveguide layer and the substrate. Therefore, three different interfaces of interest are present. Moreover, the lithographic definition of the waveguides can induce other errors that can affect the estimation of the areal charge density σ that is going to be presented. The system used for these preliminarily measurements is constituted by a 600 μm thick p-doped silicon substrate with a 140 nm thick SiN layer deposited on the top. The test structure is contacted by an aluminum back contact and a 787 μm diameter Hg droplet as a gate contact. For simplicity, it is assumed that the metal con-

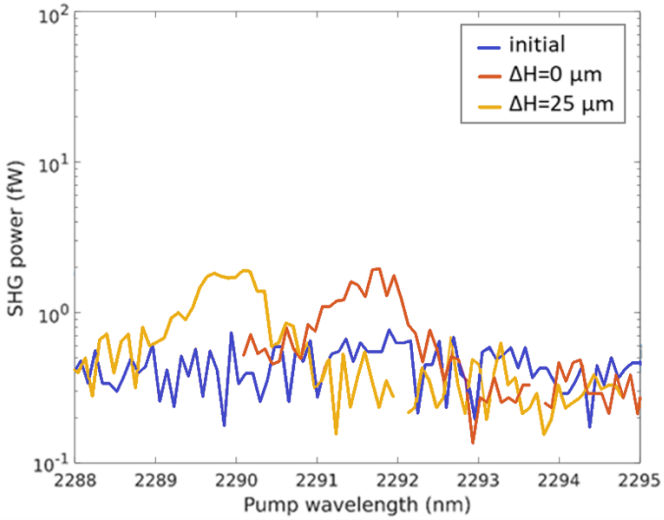

Figure 2.20: Effect of the external load on the sample after the passivation of the K^+ center defects. When a displacement of 25 μm is applied to the sample the peak appears again, but when it is removed the peak amplitude remains the same.

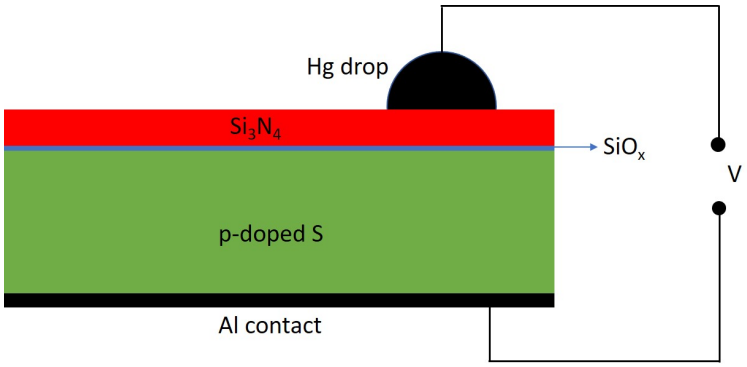

Figure 2.21: Sketch of the device used for the C-V measurements.

tact has the same work function of the semiconductor. The C-V curve shows three different regimes, that can be described in term of band structure [48] as in figure 2.22:

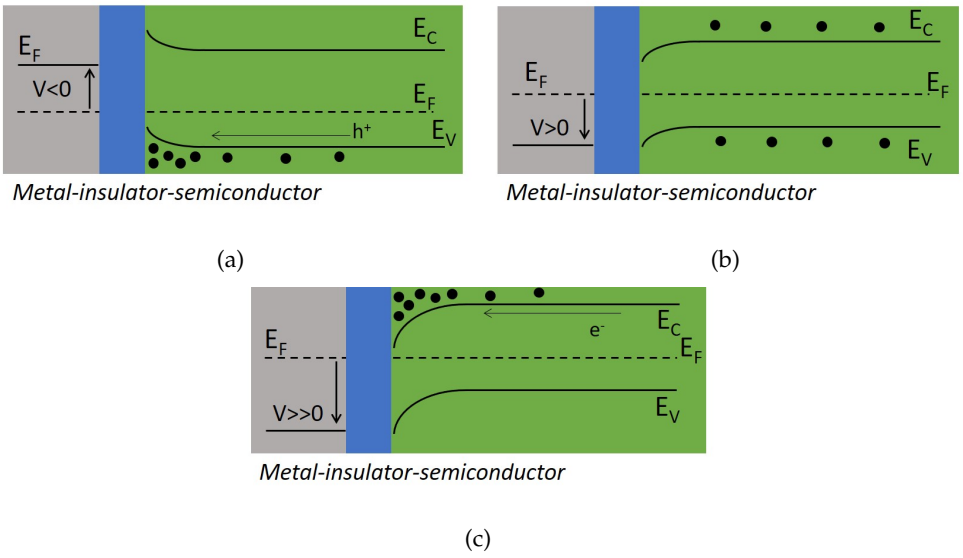

Figure 2.22: Band diagrams of the tree different regimes: (a) accumulation regime, (b) depletion regime, (c) inversion regime.

- The accumulation regime: when a negative voltage $V < 0$ is applied to the metal contact with the insulator, a bending of the band close to the semiconductor/insulator surface is observed. The Fermi level does not change in the semiconductor, as no current flows in this kind of device. Therefore, the valence band becomes closer to the Fermi level close to the surface and holes accumulated close to the interface, while the hole density is exponentially dependent on the energy difference between Fermi level and valence band. So positive charges are attracted close to the interface when $V < 0$ is applied.

- The depletion regime: when a voltage $V > 0$ is applied to the sample, close to the interface the bands bend downward. In this situation the distance of the Fermi level from the conduction band and the valence band is the same. In this regime, in the region close to the surface holes are depleted. Going from the accumulation regime to the depletion one,

one encounters the situation where $V = 0$ that is called flat-band condition. In this condition the bands become flat and the carrier distribution is the same both in the bulk silicon and close to the interface. In this condition the capacitance C_{fb} can be written as [33]:

$$C_{fb} = C_{max} \frac{\varepsilon_0 \varepsilon_s A / L_D}{C_{max} + \varepsilon_0 \varepsilon_s A / L_D} \tag{2.61}$$

with ε_s the semiconductor permittivity, A the area of the Hg droplet and L_D the Deby length of the semiconductor. Knowing the material, C_{fb} can be computed.

- The inversion regime: if $V \gg 0$ the bands bend more and close to the surface the distance of the Fermi level from the conduction band decreases with respect to the distance from the valence band. So, electrons accumulated near the interface.

This three regimes refer to the situation where the difference between the metal and the semiconductor work functions is $\phi_{ms} = 0$. In the general case when $\phi_{ms} \neq 0$, in the the flat-band condition $V_{fb} = \phi_{ms}$. Moreover, if fixed charges are accumulated at the insulator-semiconductor interface, being Q the total accumulated charge, the flat-band voltage becomes [27]:

$$V_{fb} = \phi_{ms} - \frac{Q}{C_{max}}. \tag{2.62}$$

In order to determine the total accumulated charge Q it is possible to evaluate the flat-band capacitance C_{fb} using equation 2.61 and then extract the flat-band voltage V_{fb} from the C-V curve. Finally, knowing ϕ_{ms}, the total accumulated charge can be evaluated using equation 2.62. Assuming a uniform distribution of the accumulated charge, an areal charge density of $\sigma = Q/A$ can be determined.

C-V measurements have been performed after different UV exposure times, and the results are shown in figure 2.23. Before the UV treatment, a flat-band voltage of -8 V is seen. After the UV irradiation, the curve shifts towards larger voltages, saturating at -0.5 V. This quantity corresponds to ϕ_{ms} for our structure. An areal density of $\sigma \sim 1.7 \times 10^{12}$ cm^{-2} can be estimated for the

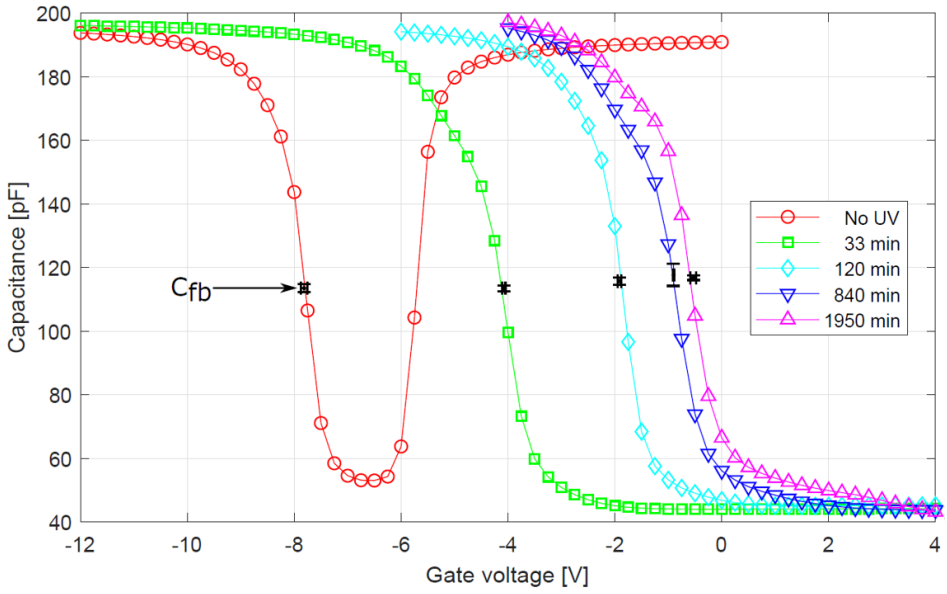

Figure 2.23: 10 kHz C-V curves measured before and after different UV exposure times (image of courtesy of Gioele Piccoli).

initial condition, while $\sigma \sim 3.1 \times 10^9$ cm^{-2} is the value estimated after 23 hours of UV irradiation.

To confirm the hypothesis that $\chi^{(2)}$ is given by the dangling bonds, the charge-induced electric field distribution inside the waveguide E_{DC} is estimated using FEM simulations. In this way it is possible to determine the distribution of $\chi^{(2)}_{EFISH}$ and extract the value of $\chi^{(2)}_{eff}$ to compare with the experimental results. Simulations have been performed using p-doped silicon with a concentration of 10^{15} cm^{-3} and a positive charge density of $\sigma = 1.7 \times 10^{12}$ cm^{-2}, as extimated from C-V measurements, on the top and sidewalls of the waveguide. These simulations have been performed using Comsol. In figure 2.24 are reported both the components x and y of E_{DC} field. The maximum of the field is close to the charged surface, with a rapid decrease while moving towards the center of the waveguide.

Since in this process the pump mode is at frequency ω_p, the SH mode is at frequency ω_{SH} and the DC field is at frequency $\omega_0 = 0$, the tensor $\chi^{(3)}\left(\omega_p, \omega_p, \omega_{SH}, 0\right)$ must be used. However, in literature there are not estimation of this coefficient. Thus, as a first approximation, the coefficient $\chi^{(3)}\left(\omega_p, \omega_p, \omega_p, \omega_p\right)$ has been used. Since the pump mode is TE polarized

and the SH mode in TM polarized, tensor elements that origin SHG are $\chi^{(3)}_{xxxy}$, related to $E_{DC,x}$, and $\chi^{(3)}_{xxyy}$, related to $E_{DC,y}$. In silicon $\chi^{(3)}_{xxxy}$=0 for symmetry [49]. So, $\chi^{(2)}_{EFISH} = 3\chi^{(3)}_{xxyy}E_{DC,y}$. In the spectral range from 1.2 μm to 2.4 μm, the empirical relationship $\chi^{(3)}_{xxyy} = \chi^{(3)}_{xxxx}/2.36$ is valid [50]. Since in literature for $\chi^{(3)}_{xxxx}$ are reported values from 0.94×10^{-19} m^2/V^2 to 4.24×10^{-19} m^2/V^2 [32, 51, 52], an average of these values has been used [4]. The final average value for a 906 nm wide waveguide of $\chi^{(2)}_{EFISH}$ is -0.3 pm/V. From this is possible to extract a value of $\chi^{(2)}_{eff} = 0.3 \pm 0.2$ pm/V where the error bar resul from the uncertainty on literature values. Since the value of $\chi^{(2)}_{eff}$ that can be extracted from the measuremet is 0.46 ± 0.05 pm/V and considering all the approximations, it can be concluded that the experimental and the simulation results are in good agreement.

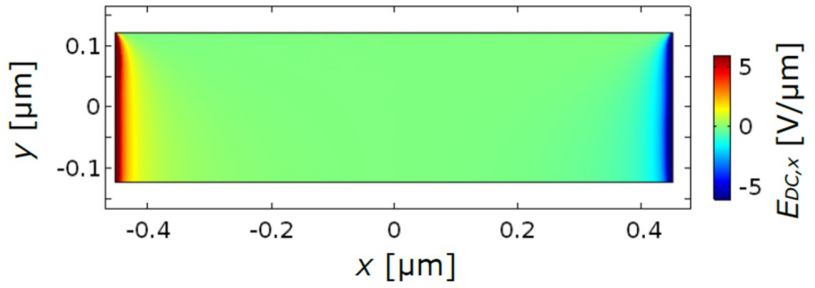

(a)

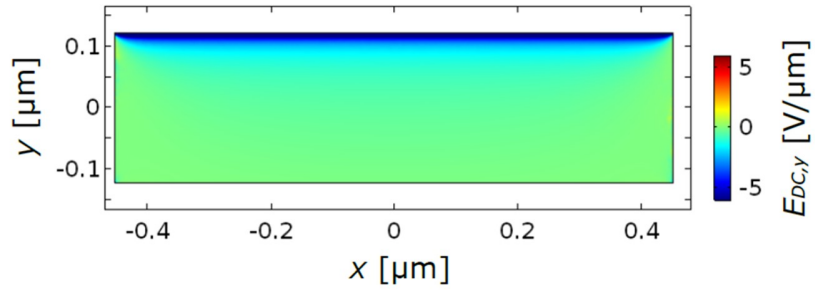

(b)

Figure 2.24: Components of the electric field E_{DC} determined by a surface charge density $\sigma = 1.7 \times 10^{12}$ cm^{-2} on the top and on the sidewalls of a 906 nm wide waveguide: (a) x component and (b) y component.

Chapter 3

EFISH Generation

3.1 EFISH theory

The results of the previous chapter show that SHG is due to static field within the waveguide caused by trapped charges. This points out that it is possible to obtain second order nonlinearities in silicon by introducing a static electric field in the waveguide. The approach consists in using silicon waveguides with lateral p-n junctions [53]. By applying a proper reverse bias to the junctions, a static electric field can be generated in the core of the waveguide. The electric field causes a variation both in the material refractive index as well as in the absorption coefficient. The material refractive index is modified due to the plasma-dispersion effect and DC Kerr effect. The first is a linear optical effect given by the variation of the free carrier concentration in the material. Calling ΔN_e and ΔN_h the variation of the electrons and holes concentrations, the material refractive index variation is:

$$\Delta n_{p-d} = -p\Delta N_e^q - r\Delta N_h^s \tag{3.1}$$

where the coefficients p, q, r and s are specific for each semiconductor and depend on the wavelength [54]. The second is a third order nonlinear effect that can be described starting from equation 1.6. Considering $\omega_3 = 0$, additional phase-modulation terms appear in equation 1.6. The nonlinear polarization vector for the wave propagating at frequency ω_1 has the form:

$$\mathbf{P}^{(3)}(\mathbf{r},t) = 3\varepsilon_0\chi^{(3)}\left[\mathbf{E}(\mathbf{r},0) + \mathbf{E}^*(\mathbf{r},0)\right]^2 \mathbf{E}_1(\mathbf{r},\omega_1)\, e^{-i\omega_1 t} + c.c. \tag{3.2}$$

Introducing $\mathbf{E}_{DC} = \mathbf{E}(\mathbf{r},0)$ and using $\mathbf{P} = \mathbf{P}_0 + \mathbf{P}^{(3)}$, it can be written:

$$\mathbf{P}(\mathbf{r},t) = \varepsilon_0\left[\chi^{(1)} + 3\chi^{(3)}\left|\mathbf{E}_{DC}\right|^2\right]\mathbf{E}_1(\mathbf{r},\omega_1)\, e^{-i\omega_1 t} + c.c. \tag{3.3}$$

So, the susceptibility perturbation induced by the DC Kerr effect is $\Delta\chi = 3\chi^{(3)}\left|\mathbf{E}_{DC}\right|^2$. Since $n^2 = \chi^{(1)} + 1$, the equation 3.3 can be written also as a function of the effective index perturbation Δn_k:

$$\Delta n_k = \frac{3\chi^{(3)}\left|\mathbf{E}_{DC}\right|^2}{2n_0} \tag{3.4}$$

being n_0 the unperturbed value of the refractive index. Therefore, both DC Kerr effect and plasma-dispersion cause a variation $\Delta n = \Delta n_{p-d} + \Delta n_k$ of the material refractive index [55].

For the absorption, the variation is due both to defects introduced during the implantation of the dopants as well as to free-carrier-induced absorption. In fact the variation of the absorption coefficient $\Delta\alpha$ as a function of the variation of the electrons and holes concentrations can be written as [54]:

$$\Delta\alpha = a\Delta N_e^b + c\Delta N_h^d. \tag{3.5}$$

The electric field in the waveguide can be created using a p-n junction fabricated across it and applying a reverse bias. In this way it is possible to create an E_{DC} field in the waveguide that can be controlled varying the value of the applied V. This field generates via EFISH an effective $\chi^{(2)}_{eff} = 3\chi^{(3)}E_{DC}$. Therefore, changing the applied bias it is possible to change the value of $\chi^{(2)}$ in the waveguide. Moreover, it is possible to use junctions placed along the length of the waveguide in a periodic way. This method is called *poling* and it allows to use the periodicity of the $\chi^{(2)}$ to absorb the mismatch between the pump and the SH modes and obtain the *quasi phase-matching condition*, as explained in section 1.2.3. Defined the propagation constant as in equation 1.14, it is possible to write the mismatch vector in presence of poling as [56]:

$$\Delta\beta = 2\beta_p - \beta_{SH} + \frac{2\pi}{\Lambda}, \tag{3.6}$$

where Λ is the periodicity of the junctions. The quasi phase-matching condition is $\Delta\beta = 0$. Therefore, from equation 3.6 it is obtained that, to satisfy this condition, the poling periodicity has to be set at

$$\Lambda = \frac{\lambda_{SH}}{n_{eff,p} - neff, SH}. \tag{3.7}$$

3.2 Propagation in poled waveguides

When SHG occurs with a constant $\chi^{(2)}$ along the propagation direction, the propagation in a waveguide of an optical pulse is described by the equation 2.52. However, in case of periodic poling also the variation of $\chi^{(2)}$ along the propagation direction has to be taken into account. For this situation we assume that $\chi^{(2)}$ can be factorized as [4]:

$$\chi^{(2)}\left(\mathbf{r}_\perp, z\right) = \chi^{(2)}\left(\mathbf{r}_\perp\right) s\left(z\right) \tag{3.8}$$

being $\chi^2\left(\mathbf{r}_\perp\right)$ the second order nonlinear coefficient in the waveguide cross section plane and $s\left(z\right)$ the poling function, i.e. the function that describes the modulation of $\chi^{(2)}$ along z. Now it is possible to write the coefficient $\widetilde{\Gamma}^{(2)}$ as:

$$\widetilde{\Gamma}^{(2)} = \frac{\sqrt{A_0}\int e\left(\mathbf{r}_\perp, \omega_p\right)\chi^{(2)}\left(\mathbf{r}_\perp\right) : e^*\left(\mathbf{r}_\perp, \omega_{SH}\right) e\left(\mathbf{r}_\perp, \omega_p\right) dA}{\left(\int n^2\left(\mathbf{r}_\perp, \omega_p\right)\left|e\left(\mathbf{r}_\perp, \omega_p\right)\right|^2 dA\right)\left(\int n^2\left(\mathbf{r}_\perp, \omega_{SH}\right)\left|e\left(\mathbf{r}_\perp, \omega_{SH}\right)\right|^2 dA\right)^{1/2}}. \tag{3.9}$$

and $\Gamma^{(2)} = s\left(z\right)\widetilde{\Gamma}^{(2)}$. Following the previous chapter, also $\widetilde{\gamma}^{(2)}_{SH}$ can be defined:

$$\widetilde{\gamma}^{(2)}_{SH} = \omega_i \frac{n_{G,p}\sqrt{n_{G,SH}}}{\sqrt{8A_0\varepsilon_0 c^3}}\widetilde{\Gamma}^{(2)}. \tag{3.10}$$

and $\gamma^{(2)}_{SH} = s\left(z\right)\widetilde{\gamma}^{(2)}_{SH}$. Therefore, equation 2.52 becomes:

$$\begin{cases} \frac{du_{SH}}{dz} + \sum_{m\geq 1} \frac{(i)^{m-1}\beta_{SH,m}}{m!} \frac{\partial^m u_{SH}}{\partial t^m} = \\ = i\widetilde{\gamma}^{(2)}_{SH} s\left(z\right) \frac{P_{0,p}}{\sqrt{P_{0,SH}}} u_p^2 e^{i\Delta\beta z} + 2i\gamma^{(3)}_{SH,p} P_{0,p} \left|u_p\right|^2 u_{SH} - \frac{\alpha_{SH}}{2} u_{SH} \\ \frac{du_p}{dz} + \sum_{m\geq 1} \frac{(i)^{m-1}\beta_{p,m}}{m!} \frac{\partial^m u_p}{\partial t^m} = \\ = 2i\widetilde{\gamma}^{(2)*}_{p} s\left(z\right) \sqrt{P_{0,SH}} u_{SH} u_p^* e^{-i\Delta\beta z} + i\gamma^{(3)}_{p,p} P_{0,p} \left|u_p\right|^2 u_p - \frac{\alpha_p}{2} u_p. \end{cases} \tag{3.11}$$

In the undepleted pump approximation $u_p\left(z\right) \sim const$, a continuous wave pulse is assumed. Temporal derivatives, third-order nonlinearities and losses can be neglected in this situation. So, from equation 3.11 it is obtained

$$\frac{du_{SH}}{dz} = i\widetilde{\gamma}^{(2)}_{SH} s\left(z\right) \frac{P_{0,p}}{\sqrt{(P_{0,SH})}} u_p^2 e^{i\Delta\beta z}. \tag{3.12}$$

As in equation 2.53, integrating along the length of the waveguide the total SH power can be expressed as:

$$P_{SH} = P_p^2 \left|\widetilde{\gamma}^2_{SH}\right|^2 L^2 S. \tag{3.13}$$

S is the term that describes what is happening along the length of the waveguide. In a waveguide without any poling it is possible to obtain 2.54. When a poling mechanism is present the equation becomes:

$$S = \frac{1}{L^2} \left| \int_0^L s\left(z\right) e^{i\Delta\beta z} dz \right|^2 \tag{3.14}$$

where $s\left(z\right)$ is the *poling function*, that describes the periodicity of the poling along the length of the waveguide, and $\Delta\beta$ is the *mismatch factor*:

$$\Delta\beta = 2\beta_p - \beta_{SH}. \tag{3.15}$$

3.14 is different respect to the equation for the SH power reported by Timurdogan et al. in [53]. The advantage of 3.14 is that it allow to separate and study the part that describes the quasi phase-matching along the length of the waveguide.

3.3 Poling configurations

In this work, two different configurations of the lateral p-n junctions are proposed. The first is similar to the one used in [53]. This configuration is named simple poling configuration and it consists in doped regions of width δ separated from the next doped region by a distance $\Delta = \Lambda - \delta$. Moreover, one type of doping is realized on each side of the waveguide, in order to have a DC field inside the waveguide directed always in the same direction. The second configuration, named interdigitated poling configuration, consists in doped regions alternating along the z direction. Each of these regions have a width δ, and neighboring regions are separated by a distance Λ, in a way such that $2(\delta + \Delta) = \Lambda$. This configuration allows a transition from negative to positive values of the field inside the waveguide, increasing the amplitude of the oscillations $\Delta\chi^{(2)}$ of the second harmonic susceptibility along the waveguide. A sketch of the two different design is shown in figure 3.1.

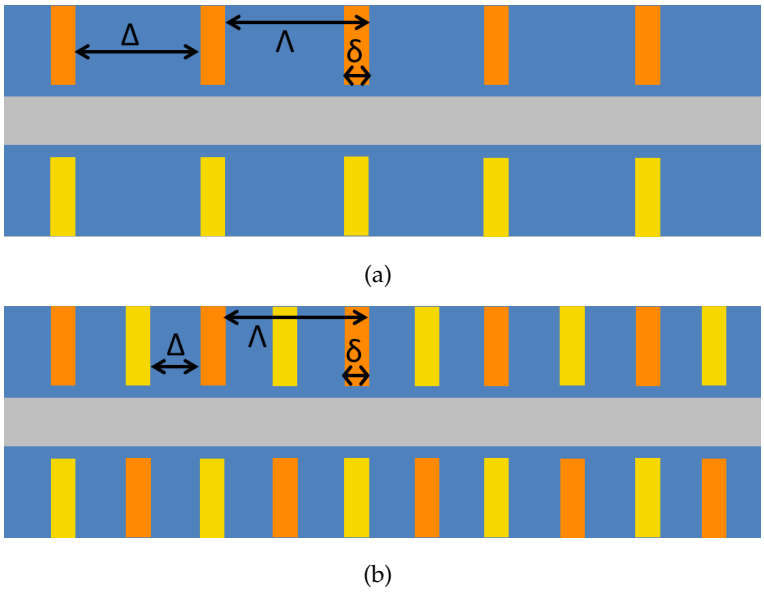

Figure 3.1: (a) sketch of the top view of a simple poling configuration waveguide; (b) sketch of the top view of an interdigitated poling configuration waveguide. Different colors correspond to different doping.

The size of each doped region is $\delta = 500$ nm. Once that Λ is set in order to satisfy 3.6, the value of Δ is determined accordingly. Moreover, in the inter-

digitate poling configuration there is also a p-i-n junction between neighboring doped regions of different sign. The value $\delta = 500$ nm is a compromise between a value unaffected by the lithographic resolution of the width of the doped regions and a large distance between neighboring doped regions to avoid breakdown between them. In fact the minimum nominal size allowed for the junctions is 400 nm, that is given by the use of i-line lithography (365 nm wavelength). Than, to take into account the angle of the implantation process, the junctions are further widened. At the end $\delta = 500$ nm is the minimum value that can be reached during the fabrication [57].

3.4 The experiment

An experiment to demonstrate that it is possible to obtain an higher generation using the interdigitated poling configuration instead of the simple poling configuration has been performed.

3.4.1 Setup

For this kind of measurements a CW solid state tunable laser source IPG Photonics CLT-2400-1100-2 pumped by a fiber laser IPG Photonics Corp ELR-10-1567 has been used. This laser is composed by two different parts. The first part is a linearly polarized continuous wave Erbium fiber laser. It is composed by a IPG single emitter diode coupled in a erbium fiber that provides multi-mode output. This source operate at 1567 nm with an output power of 10 W. This first block is fully assembled with the second high-power, CW, tunable, middle-infrared laser. This is a Cr:ZnS laser tunable in the $1895 - 3005$ nm range with an output power, dependent from the set wavelength, of up to 4.8 W. The output is a continuous linearly horizontal polarized wave. In order to avoid back reflection, that can damage the laser cavity, the beam is passed through a MIR optical isolator. After the isolator the beam is coupled to the same coupling stage described in the previous chapter.

As in the previous chapter, the pump signal wavelength is around 2300 nm.

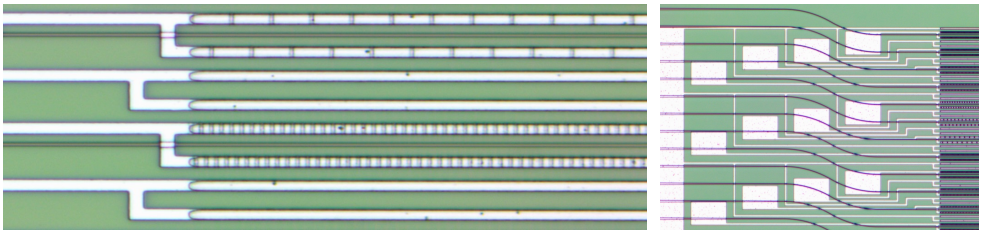

(a) (b)

Figure 3.2: Top images of the sample. (a) Zoom on the waveguide region. The white lines are the aluminum tracks and the dark ticks are insulating barriers between the junctions. In the image it is possible to see two waveguides with different poling period. (b) Zoom on the pads used to contacts the p-i-n junctions. Image courtesy of Dr. M. Ghulinyan.

3.4.2 The sample

Also the devices used for the measurements described in this chapter have been realized in FBK using first a 365 nm UV lithography to define the structures and a reactive ion etching for the final realization. The doped regions are realized by ion implantation to the sides of the waveguide, so the final junctions are p-i-n junctions. Different doped regions are separated by insulator barriers. In order to apply a reverse bias to the junctions, aluminum pads connected at them trough vias in the oxide (visible in figure 3.2) are used. The contact is made using metallic tips in contact with the pads, as sketched in figure 3.3(b). In the doped region, the concentration of the majority carriers is $1.00 \pm 0.02 \times 10^{18}$ cm^{-3}, with a residual $1.00 \pm 0.02 \times 10^{15}$ cm^{-1} p-doping in the intrinsic silicon, that correspond to the doping level of the SOI wafer.

The cross section of the waveguide is sketch in figure 3.3(a) and it is formed by a 190 nm high silicon rib on the top of a 300 nm high slab of intrinsic silicon. The waveguide has a total height of 490 nm. The distance between the doped region and the core of the waveguide is 200 nm. On the top of the waveguide a layer of oxide is deposited. Different width have been analyzed and the corresponding poling period is chosen in order to have quasi phase-matching condition. Table 3.1 shows for the three different geometries of the waveguides the relative poling period and pump resonant wavelength. For all the three waveguides both the simple and the interdigitated poling

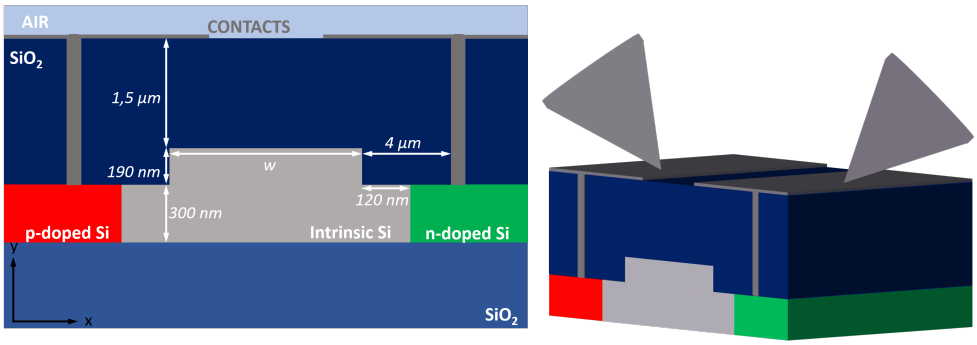

(a) (b)

Figure 3.3: Sketch of the sample. (a) Cross section of the analyzed waveguides. (b) Scheme of the contact made with metallic tips on the aluminium pads.

configuration have been realized. The propagation losses for the sample are $\alpha = 2.4 \pm 0.9$ dB/cm evaluated using the cut-back method. This design was realized by dott. Claudio Castellan.

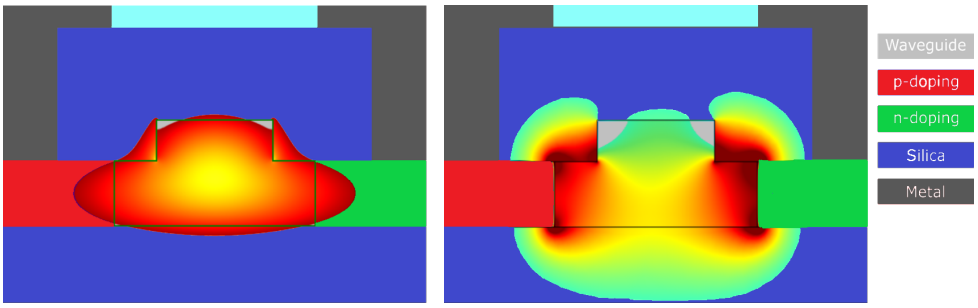

(a) (b)

Figure 3.4: (a) Distribution of the normalized pump mode in the core of the waveguide. (b) Distribution of the normalized elecric field E_{DC} in the core of the waveguide. Simulation performed by Claudio Castellan.

Applying a reverse bias an electric field E_{DC} is generated in the core of the waveguide, as shown in figure 3.4. This allows to have a good overlap between the electric field and the pump modes, that are confined in the waveguide core.

Table 3.1: **Geometric parameters and corresponding expected resonant wavelengths for the realized waveguides**

$w\ [\mu m]$	$\lambda_p\ [\mu m]$	$\Lambda\ [\mu m]$
0.809	2.3	2.600
1.238	2.3	2.897
1.878	2.3	3.137

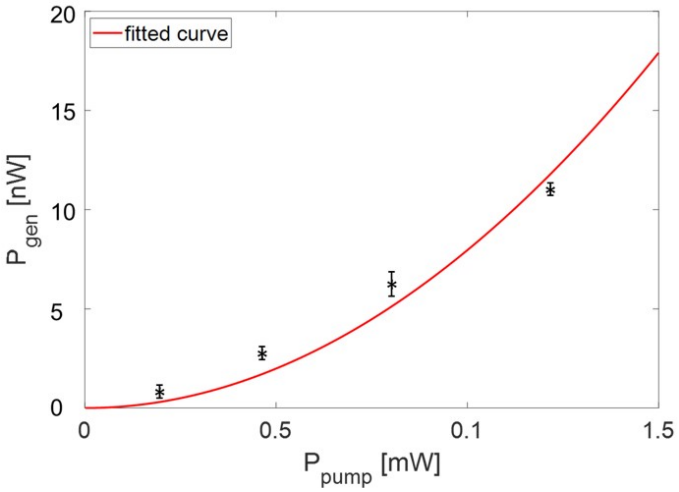

Figure 3.5: Study of the SHG power as function of the applied pump power P_p for a waveguide 0.809 μm wide and 17.5 mm long. The measurement has been done with an applied bias of 20 V and a pump wavelength $\lambda_p = 2343$ nm. The plot shows also a quadratic fit of the experimental data.

3.4.3 Electric Field Induced Second Harmonic Generation

First, SHG was observed in the samples, in order to verify the EFISH generation. When the proper bias is applied, a SH peak large less than 1 nm is generated at $\lambda_P/2$. In figure 3.6 is shown that increasing the applied bias, the generation increases in a quadratic way, according with equation 3.13. In figure 3.5 is shown that at fixed applied bias the generated peak scales in a quadratic way with the pump, as a second order nonlinear effect.

A comparison of the conversion efficiency between the simple and the interdigitated poling configuration for the same waveguide geometry has been performed. With an interdigitated poling configuration it is possible to obtain a better SHG with the same applied bias, as shown in figure 3.6. For the interdigitated poling configuration it is also visible a saturation region for an applied bias $V > 3$ V. Probably this is due to the effect of the free carriers: here there are about 200 mA of current that flow across the waveguide. This anomalous behavior is probably given by the failure of few of the more than ten thousand junctions and twice as many electrical contacts that can generate a large leakage current [58]. This effect is not visible in a simple poling configuration because in this design the electrical contacts are more simple to control. This is due to the fact that all the positive contacts are on one side of the waveguide and all the negative contacts are on the other side of it.

3.4.4 SHG as function of the pump

Also the shape of the spectrum of the generation efficiency scanning the pump wavelength has been investigated and the results are shown in figure 3.7. It is visible in figure 3.7(b) that changing the width of the waveguide the phase-matching condition changes, in contrast with the table 3.1. In fact, all the waveguides have been designed in order to have phase matching condition at $\lambda_{pump} = 2300$ nm. Moreover, there is not a real phase-matching contition but there are lot of peaks in a large emission band. In addition, the width of the emission band decreases when the width of the waveguide increases (figure 3.7(b)) and increases when the length of the waveguide increases (figure 3.7(a)). Therefore, one can suppose that these changes are given by variations in the geometry of the waveguide and in the poling periodicity due to fabrication unwanted variations (defects) along the propagation direction of

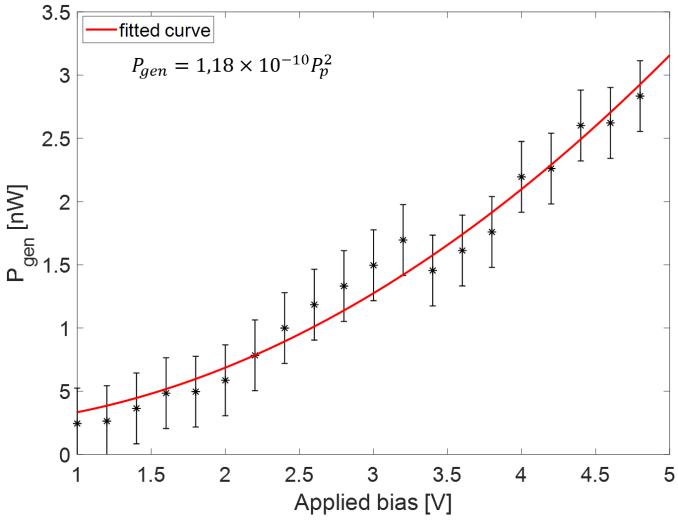

(a)

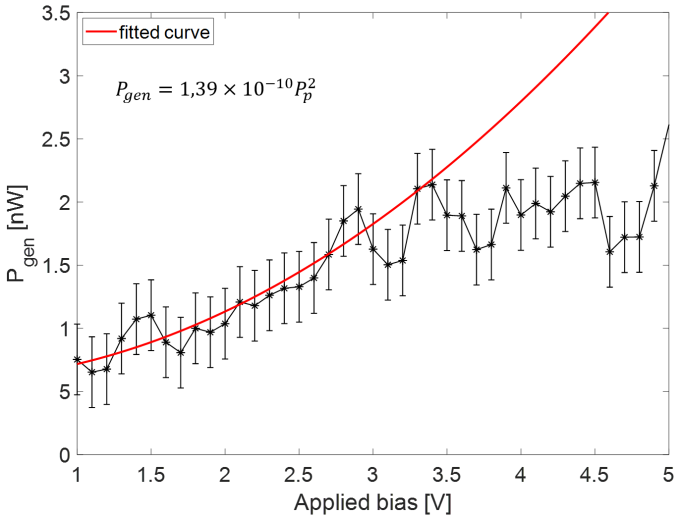

(b)

Figure 3.6: SHG power as a function of the applied bias for a $w = 0.890$ μm wide and 17.5 mm long waveguide with a simple poling configuration (up) and interdigitated poling configuration (down): with the interdigitated poling configuration it is possible to increase the effect of the bias. The measurements have been performed with $\lambda_p = 2353$ nm and $P_p = 0.8$ mW for the interdigitated poling configuration and $P_p = 1.2$ mW for the simple poling configuration.

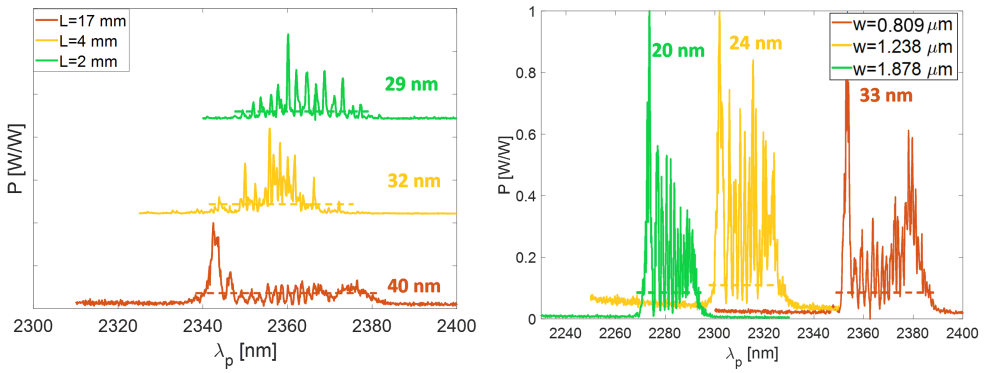

(a) (b)

Figure 3.7: (a) Variation of the band of emission as a function of the length of the waveguide: longer waveguides show larger emission band; (b) variation of the band of emission as a function of the width of the waveguide: larger waveguides show narrower emission band.

the waveguide. The width of the emission band decreases when the width of the waveguide increases because larger waveguides are more tolerant to geometrical defects, while the width of the emission band increases when the length of the waveguide increases because longer sample means more disorder. In figure 3.7(a) it is also visible that, when the sample is cleaved, some structures of the spectrum disappear. It is probably given by the fact that the region where the unwanted variations that originate these structures are present has been removed. Also the variation of the phase-matching conditions can be explain by the disorder. In fact, the phase-matching condition is dramatically influenced by the geometry of the sample. Inserting small variations in the geometry of the sample means inserting critical variation in the phase matching condition.

3.4.5 Modeling of the fabrication defects

To understand this strange form of the SH efficiency spectrum a modeling of the generated power as been done, using equation 3.14. The poling function depends from the periodicity of the junctions along the z direction, while the mismatch vector is related to the geometry from equation 1.14. The modeling has been done by considering the influence of the fabrication process

defects in the SH generation process. These defects affect SHG both inserting random variations in the waveguide cross section geometry as well as in the modulation of the p-i-n junctions along the waveguide. To model the variations in the cross section waveguide the parameter w_{eff}, that is the effective width of the rib waveguide, has been used to describe all the variations of the waveguide geometry. Meanwhile to model the variation in the modulation of the p-i-n junction, making explicit $s(z)$, the poling configuration can be written as [58]:

$$\begin{cases} s(z) = sin\left(\frac{2\pi}{\Lambda}z\right) & simple, \\ s(z) = \frac{1}{2}sin\left(\frac{2\pi}{\Lambda}z\right) + 0.5 & interdigitated. \end{cases} \tag{3.16}$$

Λ is the parameter in which the variations are induced. The calculations have been performed by using COMSOL and Matlab. Figure 3.8 shows an example of a SH generation efficiency spectrum that has been used to validate the method.

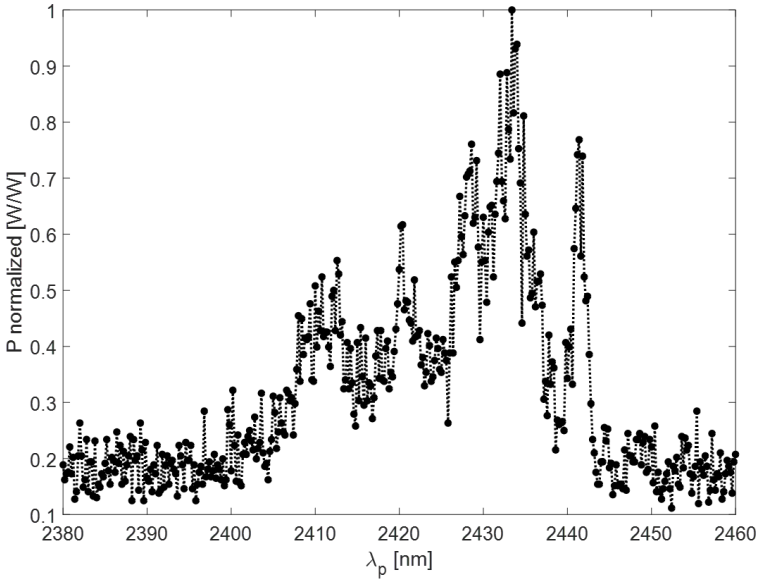

Figure 3.8: Typical spectrum of an interdigitated poling configuration waveguide. The aim of the modeling is to try to reproduce the principal features of this spectrum.

First, the proper parameters to have the quasi-phase matching wavelength of $\lambda = 2433$ nm have to be determined. From the equation

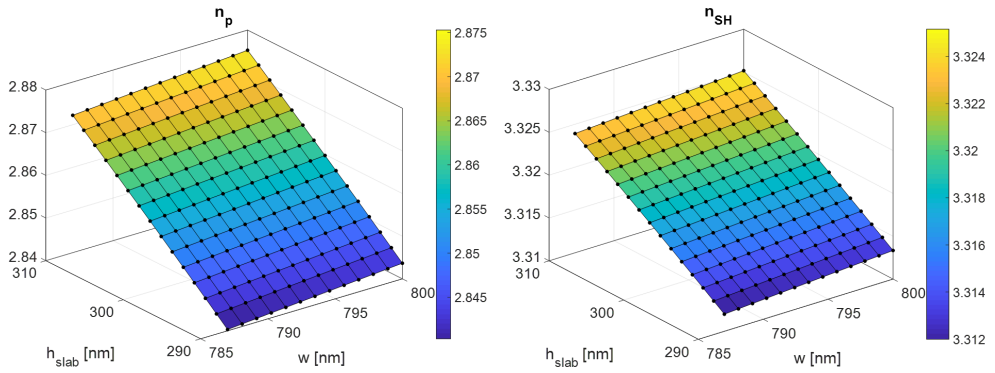

(a) (b)

Figure 3.9: (a) 2D map of n_p variation as a function of w and h_{slab}; (b) 2D map of n_{SH} variation as function of w and h_{slab} . Simulation performed with Comsol for fixed pump wavelength $\lambda_p = 2433$.

$$\Lambda = \frac{\lambda_{SH}}{n_{eff,p} - n_{eff,SH}} \tag{3.17}$$

it is obtained

$$\Delta n_{eff} = \frac{\lambda_{SH}}{\Lambda}. \tag{3.18}$$

The nominal value for the poling periodicity is $\Lambda = 2600$ nm, leading to $\Delta n_{eff} = 0.4679$. Starting from the nominal waveguide cross section parameters, that are width $w = 809$ nm, rib height $h = 190$ nm and slab height $h_{slab} = 300$ nm, a simulation in COMSOL has been done to determine the variation of the effective index both for the pump (n_p) and the SH (n_{SH}) modes as a function of w and h_{slab}. The results are shown in figure 3.9. The choice to use this two parameters as variables is dictated by the fabrication method. The total Si height in the SOI is fixed at 490 nm. Therefore, during the etching the parameter that can be changed is h_{slab} (h can be described as function of h_{slab}). On the other hand, the rib width is the result of the lithography and etching which can be changed as well. Combining the two 2D maps for the effective indexes for different geometries is possible to obtain the 2D map for Δn_{eff} as function of w and h_{slab}, that is shown in figure 3.10. From this map, the geometry of the sample that allows to have $\Delta n_{eff} = 0.4679$ can

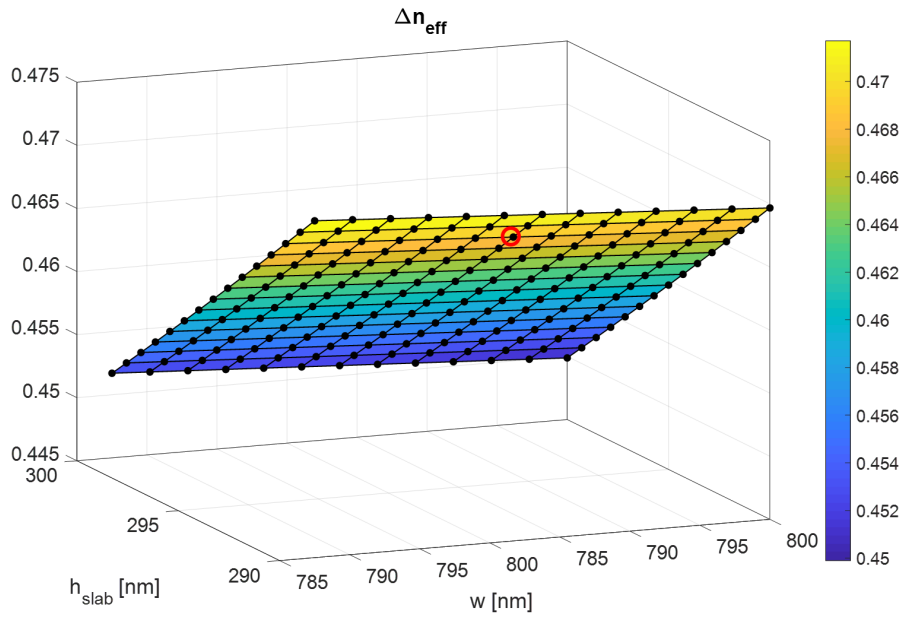

Figure 3.10: 2D map of Δn variation as a function of w and h_{slab}. The red circle indicates the selected geometry.

be extracted. Since the most critical variable is w we choose the geometry with $h_{slab} = 293$ nm and $w_{eff} = 793$ nm, that is the point that allows to reach the desired value for Δn_{eff} with the minimum variation of h_{slab}. This two parameters are in agreement with the resolution of the fabrication process.

Second, since in equation 3.14 enters $\Delta\beta$ as a parameter and not Δn_{eff}, in figure 3.11 its dependence from the pump wavelength λ_p and the vaweguide width w at fixed height of the slab has been mapped. A parametrization of this map allows to easily compute the dependence of $\Delta\beta$ on the disorder as function of λ_p, that is what is needed to reproduce figure 3.8.

Third a model to describe the disorder in the waveguide has been done assuming random fluctuations around the actual value of the width w_{eff}. $S(z)$ integral has been divided in different integration steps and a different random value of the width w_i has been used for each i integration step. Since the distribution of these defects in the waveguide is not known, two different distributions, that are the most probable in a fabrication process, have been studied and are shown in figure 3.12. The first is a normal distribution centered around the actual width, e.g. the waveguide widths have been

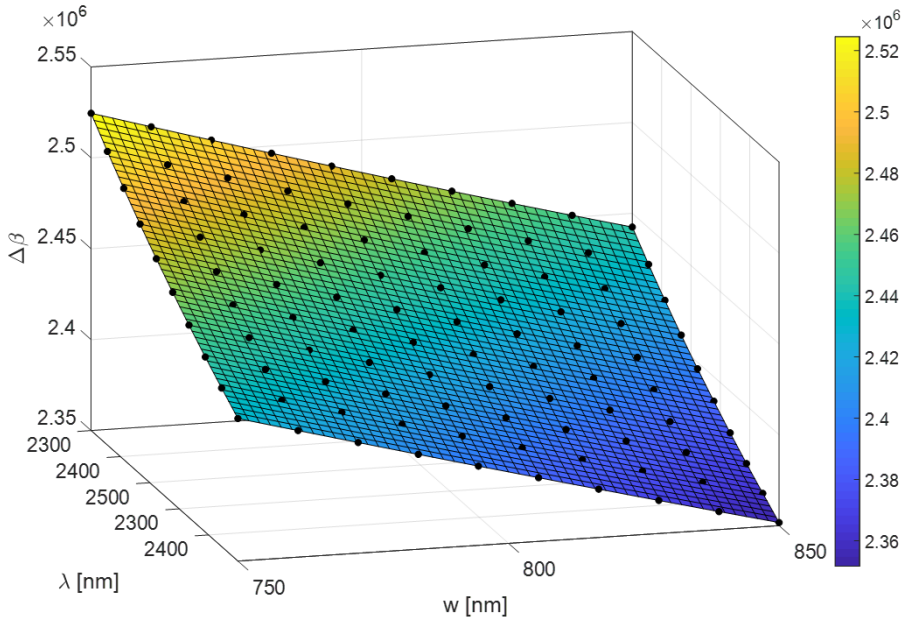

Figure 3.11: 2D map of $\Delta\beta$ as a function of λ_p and w. The actual slab height of 293 nm has been used.

randomly extracted from a Gaussian distribution centered around the width value $w_{eff} = 793$ nm and with a full width at half maximum $FWHM = 2\sigma_w$. The second is a white distribution centered around $w_{eff} = 793$ nm, e.g. the width values are randomly extracted with an equal probability between $w_{eff} - \sigma_w$ and $w_{eff} + \sigma_w$. Then the $S(z)$ integral has been evaluated using Stevino method. The shape of $S(\lambda_p)$ for different values of σ_w from 0 nm to 10 nm, values that are compatible with the used process resolution in the waveguide fabrication, has been studied and the result is shown in figure 3.13. It is important to notice that, from equation 3.13, the shape of $S(\lambda_p)$ reflects the shape of $P_{SH}(\lambda_p)$. Increasing the disorder the generation efficiency decreases and the band of generation increases. In particular, for the two distributions, when $\sigma_w > 2$ nm the central peak disappears and there are several peaks of generation.

Fourth, a chirping of the poling periods has been also modeled to study the effect of the error in the periodicity of the $\chi^{(2)}$ on the generated power. Poling unwanted fluctuations have been modeled by assuming for the different regions, where the p-i-n junctions are formed, different lengths. Using the

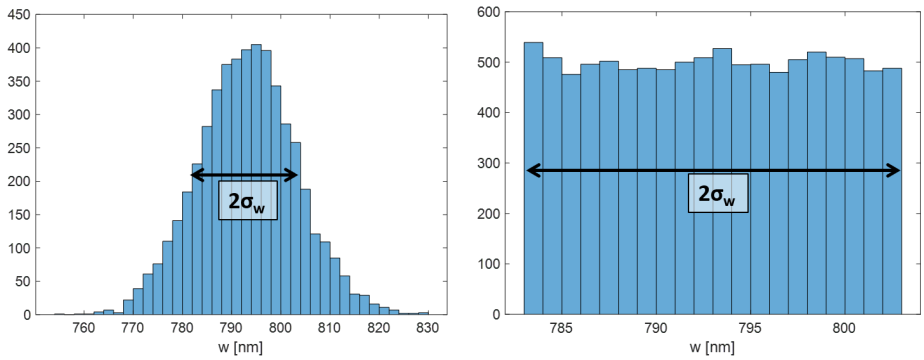

(a) (b)

Figure 3.12: (a) example of normal distribution used to extract the random values for w_i to use in the integral calculus; (b) example of white distribution used to extract the random values for w_i to use in the integral calculus. Each distribution is composed of 10000 samples.

number of junctions, evaluated as $N_j = L/\Lambda$, the integral in equation 3.14 is divided in N_j different domains:

$$S = \frac{1}{L^2}\left|\sum_{j=1}^{N_j}\int_0^{\Lambda_j} s_j(z)\, e^{i\Delta\beta z} dz\right|^2 \tag{3.19}$$

where each domain has different Λ_j and, by using 3.16, different poling function $s_j(z)$. Continuity of the poling function at the domains borders is imposed. The values Λ_j are extracted randomly from a normal or a white distribution centered around the nominal value of the poling period $\Lambda = 2600$ nm. The shape of $S(\lambda_p)$ has been studied also here for different values of σ_Λ, where σ_Λ is the width of the distribution, from 0 nm to 100 nm. Introducing disorder in the poling period of the waveguide, an error that is more that $\sigma_\Lambda = 20$ nm is needed in order to have an increment of the generation band and lot of different peaks. It is possible to compare this results with [59]. In this work a periodically poled lithium niobate fiber has been used. The authors find that using a white distribution with $\sigma_\Lambda = 35$ nm is possible to obtain a series of peaks in a broad emission band. Moreover, with an error of $\sigma_\Lambda = 50$ nm for the white distribution, from figure 3.14 it is possible to observe a 20 times reduction of S, while from [59] there is a 25 times reduction

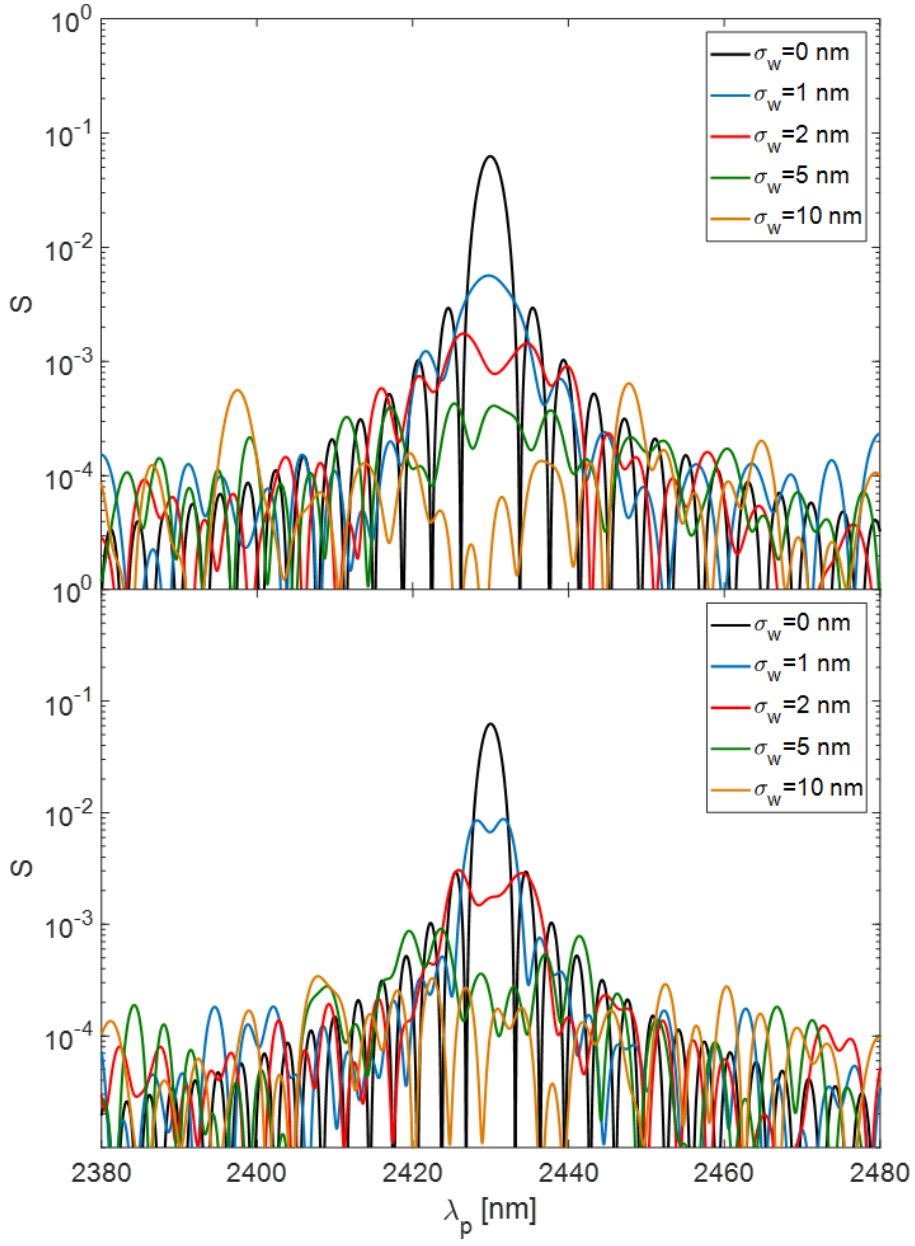

Figure 3.13: Comparison of the variation of the shape of the spectrum $S\left(\lambda_p\right)$ for different values of σ_w using the two different random distributions: normal (top) and white (bottom). Simulations have been done for a 10 mm long and 793 nm wide waveguide, with a poling period $\Lambda = 2600$ nm. To perform these simulations the waveguide has been divided in 10000 different integration steps.

in the same conditions. Considering that the material is different, the results of our model are in agreement with the reference.

Fifth, the experimental spectral width of $S\left(\lambda_p\right)$ peaks suggests to have a shorter generation length than the full waveguide length. In fact, the SHG efficiency spectral width is inversely proportional to the waveguide length [56]. Therefore, it is important to note that in 3.14 the length L describes the length where the SHG occurs. In a quasi-phase matching process the coherence length of the generation is the total length of the sample [56]. However, the coherence length of the MIR source can be evaluated as:

$$L_{coh} = \sqrt{\frac{2ln2}{\pi}} \frac{\lambda_p^2}{n_{eff}\Delta\lambda} \tag{3.20}$$

where n_{eff} is the effective index of the waveguide at λ_p and $\Delta\lambda = 0.16$ nm is the laser bandwidth. Using this formula at $\lambda_p = 2433$ nm, a coherence length of $L_{coh} = 6$ mm is found for the MIR source used in this work, that is shorter than the $L = 17$ mm total length of the waveguide. Figure 3.15 shows the effect of different lengths on the bandwidth of $S\left(\lambda_p\right)$ for an ideal waveguide. Simulation with $L = 6$ mm, i.e. equal to the coherence length of the source, yields to a 3 nm wide peak to be compared with the 2 nm width of the peak simulated for a 17 mm long ideal waveguide.

Assuming a coherence length of the process of 6 mm and a Gaussian distribution for fluctuations in the waveguide geometry as well as in fluctuations of the poling along the waveguide length, it is possible to study the value of the bandwidth and the peak value of S to estimate the value of the fluctuations which fit the experimental data and to extract the conversion efficiency η_{SH} of the EFISHG process. Plotting the peak value of $S\left(\lambda_p\right)$ as function of σ_w and σ_Λ, as in figure 3.16, it is possile to see that there is a strong dependence on σ_w whereas the dependence on σ_Λ is weak. Plotting the value of the peak for $S\left(\lambda_p\right)$ and the value of its bandwidth as function of σ_w, as shown in figure 3.17, it can be observed that after $\sigma_w = 5$ nm the conversion efficiency decreases by a factor 10^3 and after $\sigma_w = 4$ nm there is a sudden widening of the spectrum. From the plot of the bandwidth it is possible to estimate that the value for σ_w which fit the experimental data and the simulated results is $\sigma_w = 3$ nm.

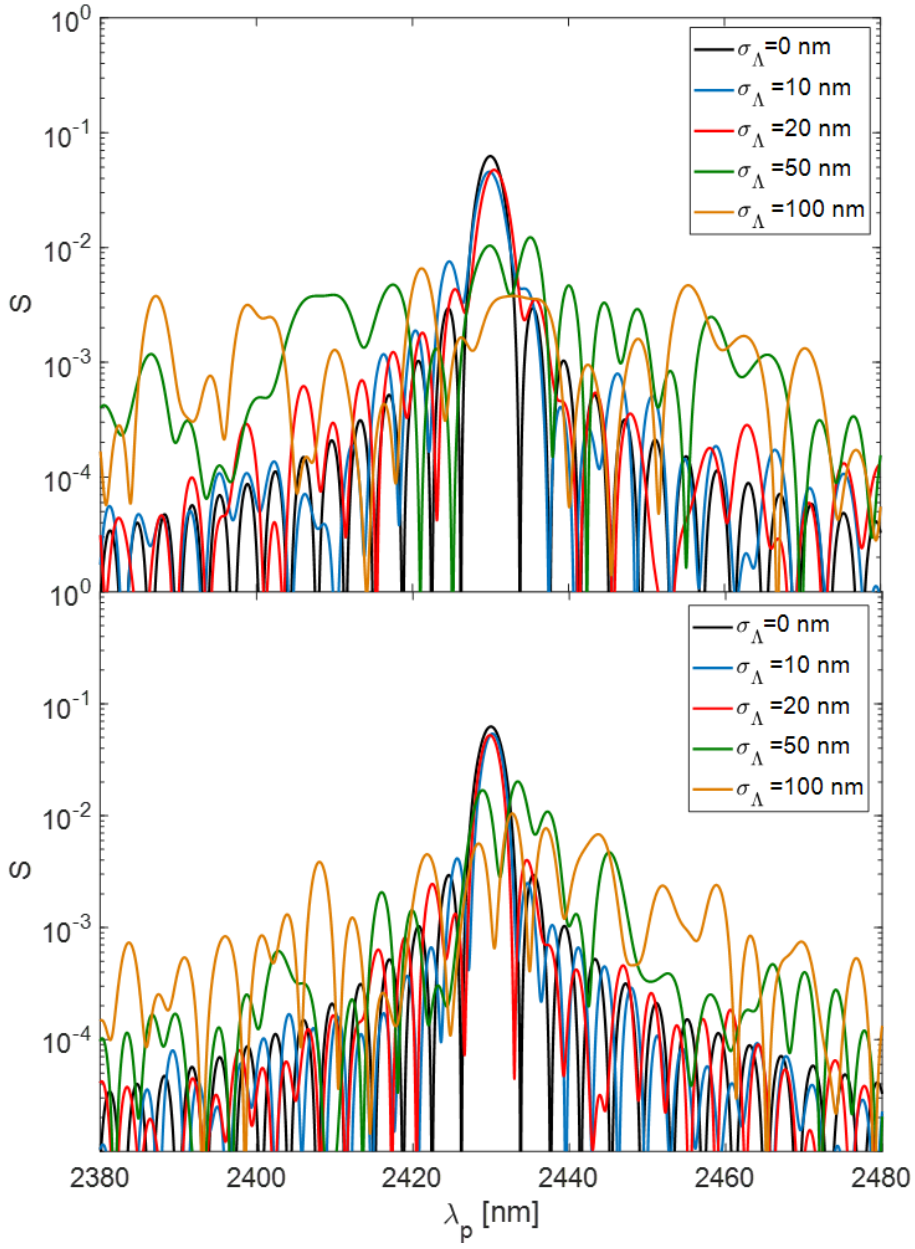

Figure 3.14: Comparison of the variation of the shape of the spectrum $S\left(\lambda_p\right)$ for different values of σ_Λ using the two different random distributions: normal (top) and white (bottom). The simulations have been done for a 10 mm long waveguide, with an average poling period of $\Lambda = 2600$ nm and a width of 793 nm. To perform these simulations the waveguide has been divided in 10000 different integration steps and 3846 domains.

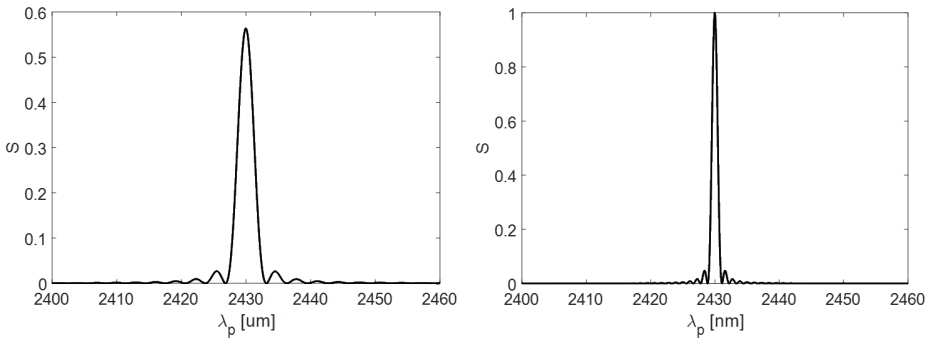

(a) (b)

Figure 3.15: Spectral dependence of the S function for an ideal waveguide at two different values of length L. (a) The used length is $L = 6$mm, that is the coherence length of the laser; (b) the used length is $L = 17$ mm, that is the total length of the waveguide.

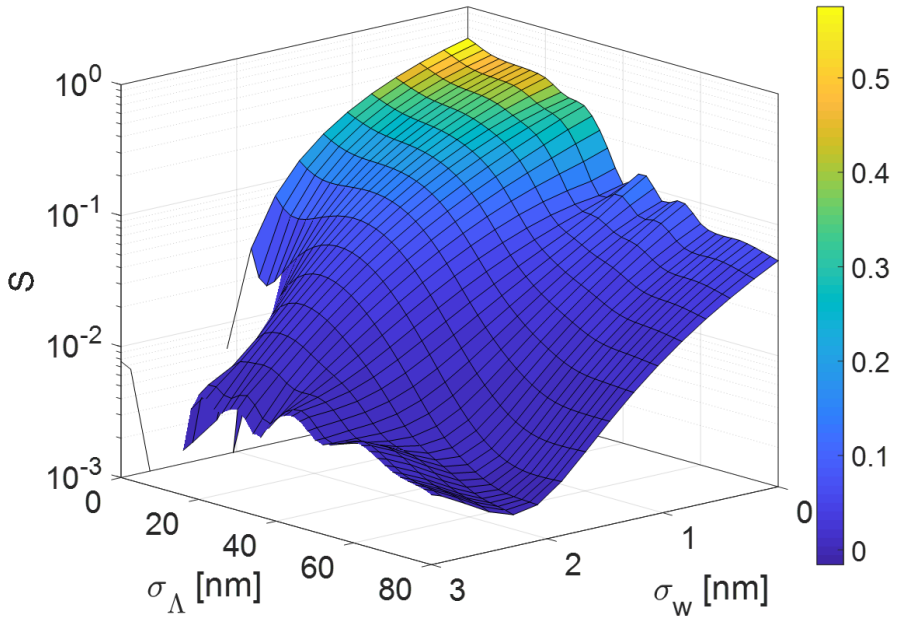

Figure 3.16: Variation of the peak value of $S\left(\lambda_p\right)$ as a function of σ_w and σ_Λ for $L = 6$ mm.

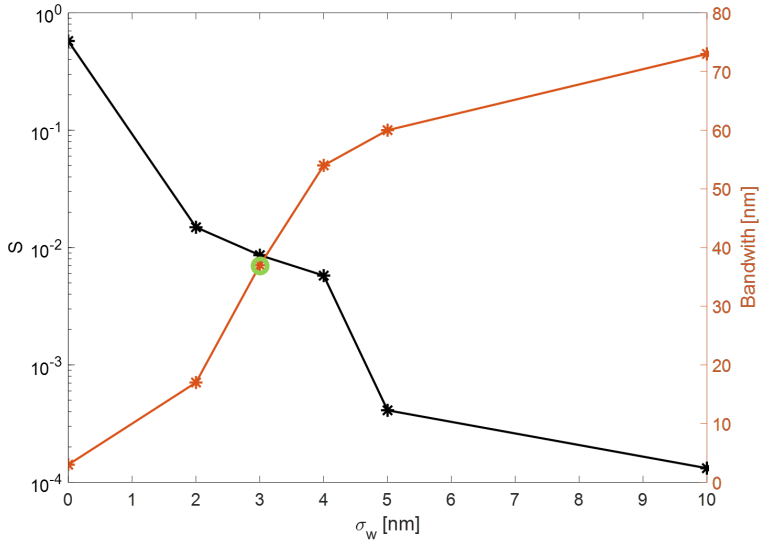

Figure 3.17: In black plot of the peak value of S as a function of σ_w ($\sigma_\Lambda = 0$). In red plot of the bandwidth as a function of σ_w. The green circle corresponds to the value of the bandwidth extracted from experimental data.

Finally, it is possible to compare the experimental data with the results of simulations where the S-function is computed with a normal distribution of fluctuations in the waveguide width of $\sigma_w = 3$ nm and for a length of the process $L = 6$ mm, equal to the pump laser coherence length. The comparison is shown in figure 3.18. Being random fluctuations, the single peaks are not fitted, but still the essential behavior of a broad multi-peaked band of the S-spectrum is reproduced.

3.4.6 Estimation of the conversion efficiency and $\Delta\chi^{(2)}$

From the experimental data it is possible to extract an effective generation efficiency η_{SH}^{exp} which is affected by the effect of poling period chirping and waveguide width fluctuations. From the model, it is possible to estimate the best combination of σ_w and σ_Λ which capture the experimental spectrum behaviour. The relative conversion efficiency $\eta_{SH}(\sigma_w, \sigma_\Lambda)$ can be scaled to the one in absence of any variation in Λ and w .

The scale factor between the ideal condition and the fit of an experimental spectrum can be estimated as:

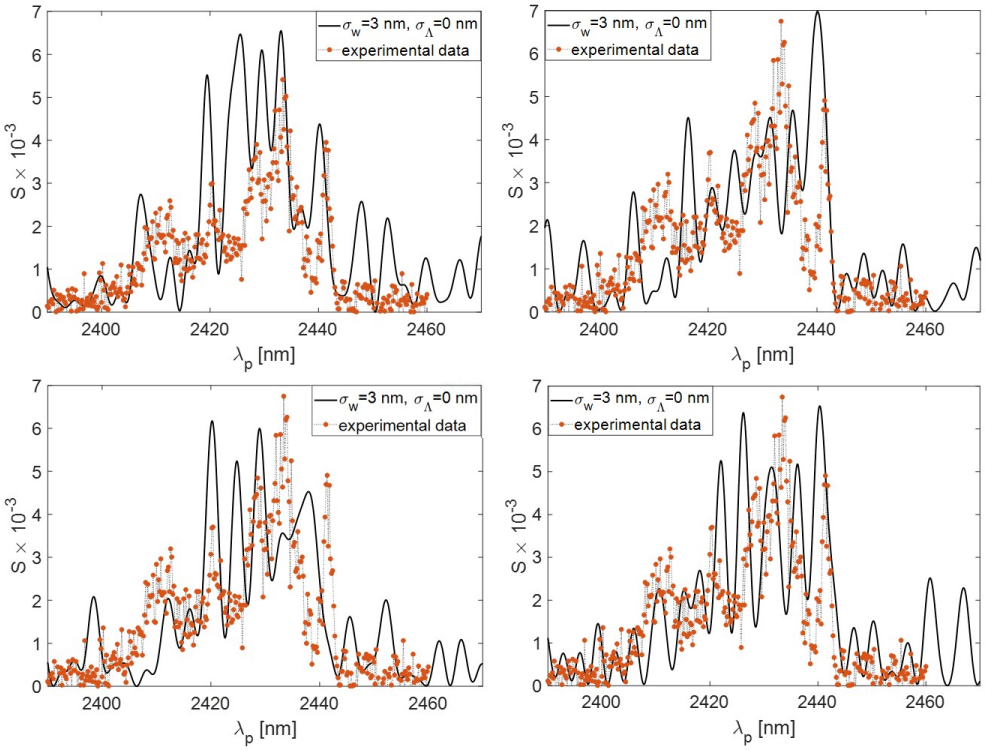

Figure 3.18: Real spectrum of an interdigitated poling configuration waveguide 17 mm long and with a nominal width of 809 nm (red), compared with four different configurations performed for a waveguide with $w_{eff} = 793$ nm, $h_{slab} = 293$ nm, $\sigma_w = 3$ nm, $\sigma_\Lambda = 0$ nm and $L = 6$ mm (black). Being random fluctuations the results of the simulations are always different. It is important to have more than one simulation with the same parameter in order to do a statistic study. Here it is possible to see that, using these parameters, the principal features of the experimental data are always reproduced by the simulations.

$$x = \frac{\eta_{SH}\left(\sigma_w = 3nm, \sigma_\Lambda = 0nm\right)}{\eta_{SH}\left(\sigma_w = 0nm, \sigma_\Lambda = 0nm\right)}. \tag{3.21}$$

If we define the conversion efficiency $\eta_{SH} = \frac{P_{SH}}{P_p^2}$, we get:

$$x = \frac{P_{SH}\left(\sigma_w = 3nm, \sigma_\Lambda = 0nm\right)}{P_{SH}\left(\sigma_w = 0nm, \sigma_\Lambda = 0nm\right)}. \tag{3.22}$$

Writing P_{SH} as in 3.13, 3.22 yields:

$$x = \frac{S\left(\sigma_w = 3nm, \sigma_\Lambda = 0nm\right)}{S\left(\sigma_w = 0nm, \sigma_\Lambda = 0nm\right)}. \tag{3.23}$$

From figure 3.17 it results $1/80$. With this scale factor the estimated conversion efficiency of the process is $0.32 \pm 0.02\ \mathrm{W}^{-1}$ for the interdigitated configuration with an applied bias of 4 V. From figure 3.6 it is possible to estimate the expected value at high voltage [53, 60]. The results are shown in table 3.2.

Table 3.2: **Extracted values of η and $\Delta\chi^{(2)}_{eff}$ for low and high voltage**

$V\ [V]$	$\eta_{\sigma_w=3nm}$	$\eta_{\sigma_w=0nm}$	$\Delta\chi^{(2)}_{eff}$
4	$4 \times 10^{-3}\ \mathrm{W}^{-1}$	$0.32 \pm 0.02\ \mathrm{W}^{-1}$	14.6 ± 0.5 pm/V
24	$0.115\ \mathrm{W}^{-1}$	$9.2 \pm 0.7\ \mathrm{W}^{-1}$	78 ± 3 pm/V

In table 3.2 are also shown the corresponding values for $\Delta\chi^{(2)}_{eff}$. Following [26] is possible to extract for $\Delta\chi^{(2)}$:

$$\Delta\chi^{(2)} = \frac{\int e\left(r_\perp, \omega_p\right) \Delta\chi^{(2)}_{EFISH}\left(r_\perp\right) e^*\left(r_\perp, \omega_{SH}\right) e\left(r_\perp, \omega_p\right) dA}{\int e\left(r_\perp, \omega_p\right) e^*\left(r_\perp, \omega_{SH}\right) e\left(r_\perp, \omega_p\right) dA} \tag{3.24}$$

where $e\left(r_\perp, \omega_i\right)$ are the profiles of the electromagnetic fields related to the different modes in the cross section of the waveguide. Here $\Delta\chi^{(2)}_{EFISH}$ is not known. From equation 3.13 it is possible to extract the value for $\widetilde{\gamma}^{(2)}_{EFISH}$ as:

$$\widetilde{\gamma}^{(2)}_{EFISH} = \sqrt{\frac{\eta}{L^2 S}}. \tag{3.25}$$

Using equation 3.10 it is possible to evaluate $\widetilde{\Gamma}^{(2)}$ as:

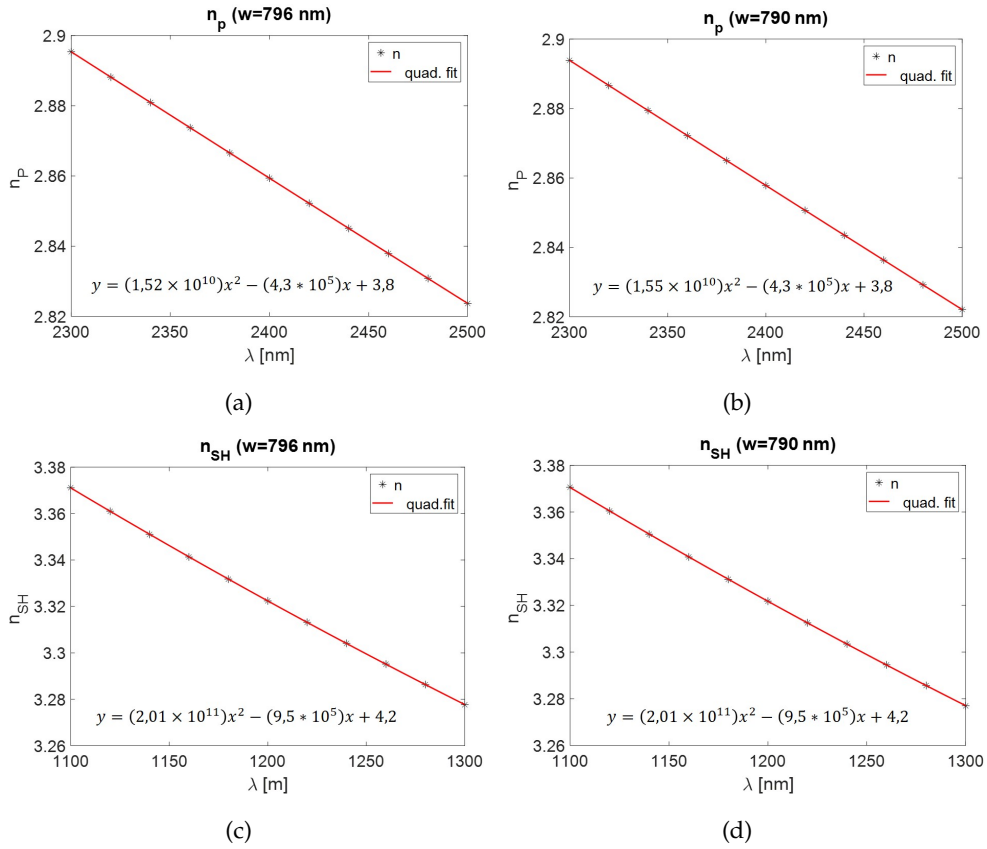

Figure 3.19: Dispersion of the effective index for two different widths of the sample for the pump mode (up) and the SH mode (down). The simulations have been performed using Comsol. For both the widths of the waveguide the result for the group index of the pump mode is $n_{g,p} = 3.7$ and for the group index of the SH mode is $n_{g,SH} = 3.9$.

$$\widetilde{\Gamma}^{(2)} = \frac{\sqrt{8A_0\varepsilon_0 c^3}}{\omega_{SH} n_{g,p}\sqrt{n_{g,SH}}}\widetilde{\gamma}^{(2)}_{EFISH} \tag{3.26}$$

with A_0 cross section of the waveguide and $n_{g,i}$ the group indexes of the SH and pump modes. Finally, joying together the equations 3.9 and 3.24, it is possible to estimate the effective $\Delta\chi^{(2)}$ as:

$$\Delta\chi^{(2)}_{eff} = \widetilde{\Gamma}^{(2)}\frac{\left(\int n^2\left(\mathbf{a}_p\right)\left|e\left(\mathbf{a}_p\right)\right|^2 dA\right)\left(n^2\left(\mathbf{a}_{SH}\right)\left|e\left(\mathbf{a}_{SH}\right)\right|^2 dA\right)^{1/2}}{\sqrt{A_0}\int e\left(\mathbf{a}_p\right)e^*\left(\mathbf{a}_{SH}\right)e\left(\mathbf{a}_p\right)dA} \tag{3.27}$$

where the vector $\mathbf{a}_i$ is defined as $\mathbf{a}_i = (r_\perp, \omega_i)$.

It is important to notice that the term $\widetilde{\Gamma}^{(2)}$ is directly proportional to $\sqrt{A_0}$, and this made the dependence of $\Delta\chi^{(2)}$ to the waveguide cross section vanishes. Moreover, the variation of the dispersion of the effective index both for the pump and the SH mode for small variations of the cross section is very low. A variation of 6 nm does not influence the group index in a critical way, as it is shown in figure 3.19. Therefore, this model allows to totally remove the dependence on fabrication defects from the $\chi^{(2)}$, enabling to evaluate the real $\Delta\chi^{(2)}$ of the process. The result reported in this section is higher respect to the one find by Timurdogan et al. in [53]. In [53] the authors find a $\chi^{(2)}_{eff} = 41 \pm 1.5$ pm/V at an applied reverse bias of 21 V using a simple poling configuration. In this work it was demonstrated how it is possible to increase the value of $\chi^{(2)}$ up to 78 pm/V using an interdigitated poling configuration.

3.4.7 Future prospects

This sample is a prototype that has been realized in Fondazione Buno Kessler using a i-line lithography with 365 nm wavelegnth, that is the standard process used in this facility. This study has been done in order to estimate the conversion efficiency and $\Delta\chi^{(2)}$ that it is possible to reach using EFISH generation. We have now a clear understanding of the EFISHG process and of the limitations induced by fabrication imperfections. It is now possible to use a customized high resolution process in order to improve the conversion efficiency of the chip.

Chapter 4

Microring resonator design

4.1 SHG condition in a microring

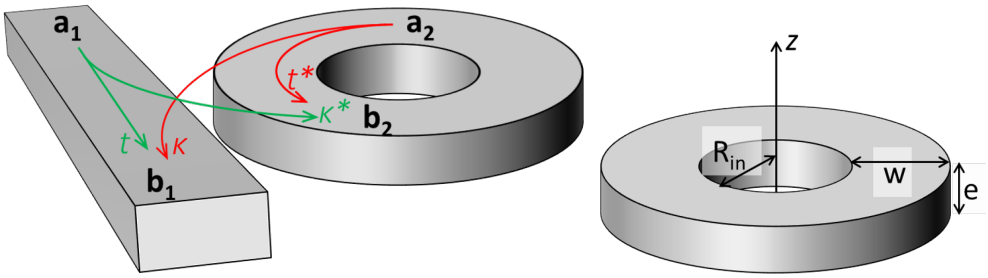

(a) (b)

Figure 4.1: (a) Sketch of the coupling between the bus waveguide and the ring. $\mathbf{a}_1$ and $\mathbf{b}_1$ are the amplitudes of the electric field inside the bus waveguide before and after the coupling with the ring. $\mathbf{a}_2$ and $\mathbf{b}_2$ are the amplitudes of the electric field in the ring before and after the coupling with the bus waveguide. k and k^* are the coupling coefficients. t and t^* are the transmission coefficients. (b) Sketch of a microring: R_{in} is the internal radius of the microresonato, w is its width and e is its thickness.

Having demonstrated SHG in silicon , we here discuss the design of a microresonator suitable for SHG. We used a microresonator with a ring geometry which is named microring resonator. Comsol within Matlab was used to realize the design.

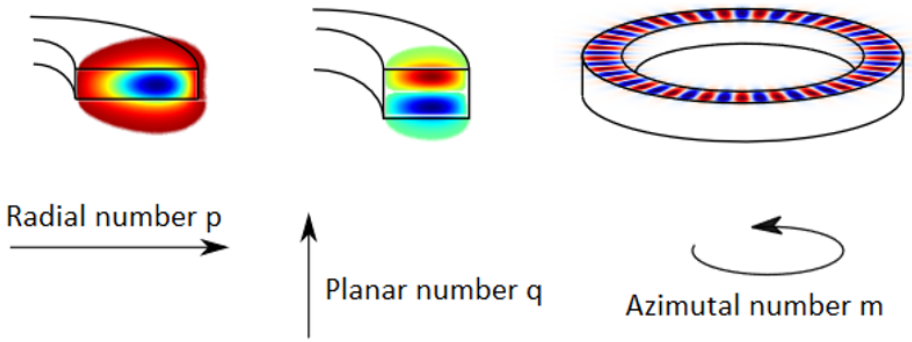

Figure 4.2: Sketch of the different numbers that describe a resonant mode in a ring.

4.1.1 Light propagation in a microring resonator

The light propagating in a microring can be described by the resonant modes of the electric field. Each mode is described by three numbers, as shown in figure 4.2. q is the planar number and gives the number of the electric field extremes along z. p is the radial number and corresponds to the number of extremes along r. m is the azimuthal number and represents the number of wavelengths in one round-trip. In order to be resonant, the mode need to have an integer number of m: in this way there is a constructive interference within waveguide propagating in different round-trip, otherwise there will be destructive interference between them and no light will propagate in the microring. m is related to the effective index by the relationship [61]

$$m\lambda = 2\pi n_{eff} R. \tag{4.1}$$

where R is the radius of the microring evaluated in the center of the microring waveguide. This relation is called *resonant condition*. These modes can be found in the two different polarizations TE and TM.

To inject the pump field in the ring, a straight bus waveguide is used. It is possible to engineer the distance between the bus and the ring in order to have a coupling between them [61]. Defined P_{cpld} the power injected in the ring by the bus and P_{loss} the power that is dissipated by the microring in a round trip, during the coupling three different condition are possible:

- $P_{cpld} < P_{loss}$ that is the under coupling condition. In this condition it is

not possible to observe SHG in the ring because the power injected is lower respect to the intrinsic loss of the ring.

- $P_{cpld} = P_{loss}$ that is the critical coupling condition. This is the best condition to observe SHG in the microresonator.
- $P_{cpld} > P_{loss}$ that is the over coupling condition. We want to generate SH in the microring and be able to observe it. In this condition the power injected is to high that at the output it will cover the SH signal.

4.1.2 The momentum conservation

The angular momentum, as well as the energy, must be conserved in a ring. This conservation depends on the modes that are coupled trough the susceptibility tensor. Here we assume a $\bar{4}$ symmetry for $\chi^{(2)}$:

$$\chi^{(2)}_{zxy} \neq 0. \tag{4.2}$$

Thanks to the geometry of the second order susceptibility tensor, a TE pump mode generates a TM SH mode [62, 11]. The eletric field of the generated mode is given by:

$$E_{z,SH} = \chi^{(2)}_{zxy} E_{x,p} E_{y,p} \tag{4.3}$$

where $E_{x,p}$ and $E_{y,p}$ are the electric fields of the two pump photons. It is useful to switch to the circular polarizations instead of the cartesian coordinates [63]. The x-linearly polarized and y-linearly polarized states can be written as:

$$\begin{cases} |x\rangle = \frac{1}{\sqrt{2}} \left(|+\rangle + |-\rangle\right) & x - polarized \\ |y\rangle = \frac{i}{\sqrt{2}} \left(|+\rangle - |-\rangle\right) & y - polarized. \end{cases} \tag{4.4}$$

To evaluate the $|xy\rangle$ SH state it is useful to define the creator operator $\hat{a}^+_n$ and destruction operator $\hat{a}_n$:

$$\begin{cases} creator & \hat{a}^+_n |n\rangle = \sqrt{n+1}\, |n+1\rangle \\ destruction & \hat{a}_n |n\rangle = \sqrt{n}\, |n-1\rangle . \end{cases} \tag{4.5}$$

The $|x\rangle$ and the $|y\rangle$ states can be written as:

$$\begin{cases} |x\rangle = \hat{a}_x^+ |0\rangle \\ |y\rangle = \hat{a}_y^+ |0\rangle . \end{cases} \tag{4.6}$$

Matching equation 4.4 with 4.6 it is obtained:

$$\begin{cases} \hat{a}_x^+ = \frac{1}{\sqrt{2}} \left(\hat{a}_+^+ + \hat{a}_-^+\right) \\ \hat{a}_y^+ = \frac{i}{\sqrt{2}} \left(\hat{a}_+^+ - \hat{a}_-^+\right) . \end{cases} \tag{4.7}$$

Using this two operators to generate the SH state the result is:

$$\begin{aligned} |xy\rangle &= \hat{a}_x^+ \hat{a}_y^+ |0_x 0_y\rangle = \\ &= \frac{1}{\sqrt{2}} \left(\hat{a}_+^+ + \hat{a}_-^+\right) \frac{i}{\sqrt{2}} \left(\hat{a}_+^+ - \hat{a}_-^+\right) |0_+ 0_-\rangle = \\ &= \frac{i}{2} \left(\hat{a}_+^+ \hat{a}_+^+ + \hat{a}_-^+ \hat{a}_+^+ - \hat{a}_+^+ \hat{a}_-^+ - \hat{a}_-^+ \hat{a}_-^+\right) |0_+ 0_-\rangle = \\ &= \frac{i}{2} \left(\hat{a}_+^+ \hat{a}_+^+ - \hat{a}_-^+ \hat{a}_-^+\right) |0_+ 0_-\rangle = \\ &= \frac{i}{2} \left(\hat{a}_+^+ |+\rangle - \hat{a}_-^+ |-\rangle\right) = \\ &= \frac{i}{2} \left(\sqrt{2} |++\rangle - \sqrt{2} |--\rangle\right) = \\ &= \frac{i}{\sqrt{2}} \left(|++\rangle - |--\rangle\right) \end{aligned} \tag{4.8}$$

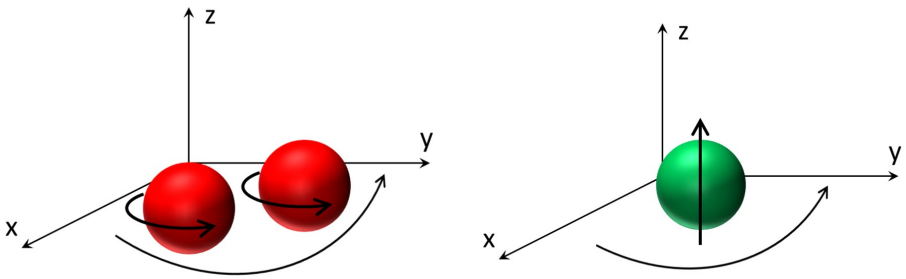

(a) (b)

Figure 4.3: (a) Sketch of the angular momentum along z for the 2 pump photons. (b) Sketch of the angular momentum along z for the SH generated photon. The condition $m_{SH} = 2m_p + 2$ must be respected to have the angular momentum conservation.

As a consequence the SH can be generated by using either two photons $|+\rangle$ or two photons $|-\rangle$. Figure 4.3 shows the case where two $|+\rangle$ photons interact. In the pump mode each photon has a $+1$ spin momentum and m_p orbital momentum. The total angular momentum along z is then $2m_p + 2$. For the SH mode the photon has 0 spin momentum and m_{SH} orbital momentum. The total angular momentum along z is then m_{SH}. For the angular momentum conservation it is possible to obtain

$$m_{SH} = 2m_p + 2. \tag{4.9}$$

If the two interacting photons are two $|-\rangle$ photons, the angular momentum conservation condition is

$$m_{SH} = 2m_p - 2. \tag{4.10}$$

Therefore, the general momentum conservation condition for the SHG generation process in a ring can be written as:

$$m_{SH} = 2m_p \pm 2. \tag{4.11}$$

4.1.3 The radius of the ring

In this work the study is limited to the case where $q_p = q_{SH} = 1$, $p_p = 1$ and $p_{SH} = 3$. In order to have SHG in the ring, the radius that can support in a resonant way both the pump wavelength λ_p and the SH wavelength $\lambda_{SH} = \lambda_p/2$ with $m_{SH} = 2m_p + 2$ has to be found. A comsol within matlab program has been used to find the internal radius of the ring and the corresponding pump wavelength to have SHG. The typical iteration of the program is shown in figure 4.4. The user has to fix the thickness, the width and the pump azimuthal number. Moreover, he has to give the extremes R_1 and R_2 of the interval in which the internal radius of the ring is expected to be. The program finds the pump resonant wavelength with azimuthal number m_p and the SH resonant wavelength with azimuthal number m_{SH} for both the radii. Than it connects the two pump modes and the two SH modes

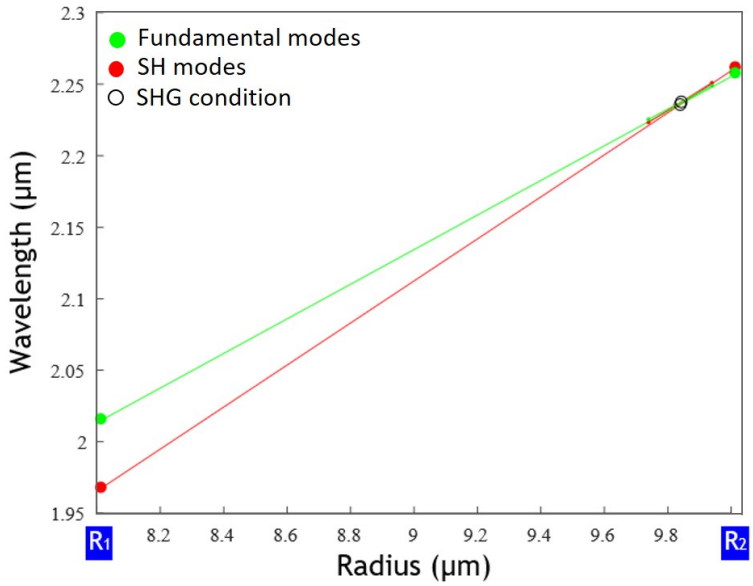

Figure 4.4: Typical iteration of the program. In the first step the first condition for SHG is found. Then the radius interval is reduced, a second condition for SHG is found and the radius interval is reduced again. The program stops when the difference between two consecutive SHG conditions is lower with respect to a threshold that can be chosen by the user.

with straights lines, as shown in figure 4.4, and finds the intersection between them. Than it takes two new R_1 and R_2 around the intersection point so that the radius interval is reduced and performs another time the evaluation of the pump and SH modes. The program performs several iterations that modify the interval of the ring's internal radius until SHG condition is satisfied. The refractive index dispersions used in the modeling for the different materials are taken from [63].

4.2 Pump wavelength vs geometrical parameters

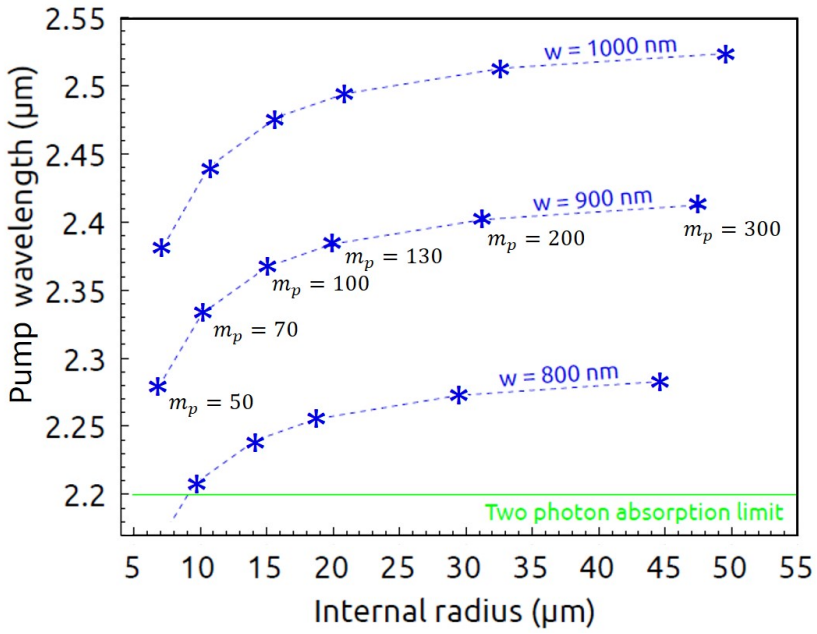

Figure 4.5: Pump wavelenght as a function of the ring's internal radius for different widths w and fixed thickness $e = 280$ nm. The points represent the different geometries suitable for SHG generation.

Figure 4.5 shows different possible geometries that satisfy the SHG condition for fixed thickness $e = 280$ nm. For a fixed value of the width w, it is possible to find different azimuthal numbers m_p that allow to generate SH. It is also possible to see that when the radius increases, the wavelength increases. This comes from the resonant condition:

$$\begin{cases} m_p \lambda_p = 2\pi R n_{eff}^p \\ m_{SH} \lambda_{SH} = 2\pi R n_{eff}^{SH}. \end{cases} \tag{4.12}$$

Replacing m_p and m_{SH} in the angular momentum conservation $m_{SH} = 2m_p + 2$ it is possible to obtain:

$$\frac{2\pi R n_{eff}^{SH}}{\lambda_p/2} = 2\frac{2\pi R n_{eff}^{p}}{\lambda_p} + 2 \tag{4.13}$$

and this leads to

$$2\pi R \left(n_{eff}^{SH} - n_{eff}^{p} \right) = \lambda_p. \tag{4.14}$$

In figure 4.5 it is also shown how changing the azimuthal number it is possible to change the pump wavelength for SHG. In the figure dashed curves are used to underline that SHG occurs only on the ring resonances, and these resonances are separated, i.e. the azimuthal number is an integer. It can also be noticed that along the same curve (fixed w), the radius increases with m_p. This because an higher numbers of maximum is needed to fit one round-trip. Moreover, a saturation region is visible for large radii. This is due to the fact that when the radius becomes large the ring resembles more a straight waveguide. Therefore, the angular momentum conservation is replaced by the linear momentum conservation, losing the dependence from the radius. Finally, the figure also shows that for a given m_p the pump wavelength is longer when the width increases. This is given by the fact that when w is larger the effective index increases, therefore in order to keep the azimuthal number constant the wavelength lengthens. From this study it is possible to find the combinations w-m_p that allow to have 2.2 μm $< \lambda_p <$ 2.6 μm. The shorter wavelength limit is chose in order to avoid TPA in silicon, that will compete with SHG, reducing his generation efficiency. The largest wavelength limit is chose because of the available laser source in our laboratory.

Figure 4.6 shows the variation of the pump wavelength as a function of the internal radius changing the thickness of the ring for fixed width $w = 800$ nm. Here, it is possible to notice that the variation of the pump wavelength is not monotonous with the thickness. There are three different regimes:

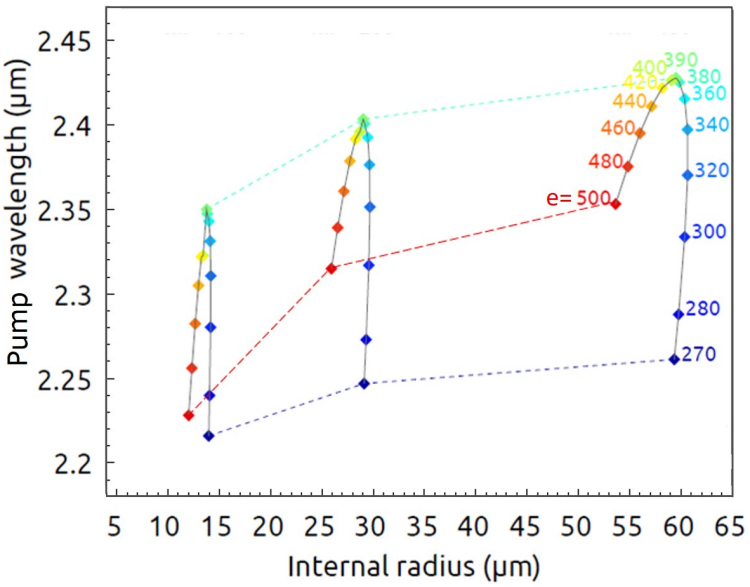

Figure 4.6: Pump wavelenght as a function of the ring internal radius for different widths e. The three curves represent three different azimuthal numbers: from left to right $m_p = 100$, $m_p = 200$ and $m_p = 400$. Different colors are used to identify the different thicknesses (expressed in nm).

- $e < 400$: the pump wavelength increases with the thickness,
- $e = 400$: the maximum for all the three curves is observed,
- $e > 400$: the wavelength decreases with the thickness.

In this figure the curves are continuous: if we fix w, for any values of e an internal radius as well as a pump wavelength fulfilling the SHG condition are found.

4.3 Robust geometries

The conversion efficiency expression can be written as (see *Appendix B* for further details):

$$\eta_{SH} = 4\pi^2 |K|^2 \frac{\hat{\alpha}_{SH}^2 \left(1 - t_{SH}^2\right)}{1 + \hat{\alpha}_{SH}^2 t_{SH}^2 - 2\hat{\alpha}_{SH} t_{SH} cos(\phi_{SH})} \left(\frac{\hat{\alpha}_p^2 \left(1 - t_p^2\right)}{1 + \hat{\alpha}_p^2 t_p^2 - 2\hat{\alpha}_p t_p cos(\phi_p)} \right)^2 \tag{4.15}$$

with $\hat{\alpha}_i$ absorption of the material, t_i transmission of the waveguide, ϕ_i phase of the mode and K evaluated with Comsol from equation 5.29.

In the critical coupling condition, with $P_{in} = 1$ mW, $Q_p^{int} = 10^4$, $Q_{SH}^{int} = 10^6$ and $\chi_{zxy} = 1$ pm/V [41], η_{SH} as a function of the internal radius and of the thickness has been evaluated. Concerning the radius, the results are shown in figure 4.7. It is visible that the smaller is the radius, the larger the conversion efficiency is.

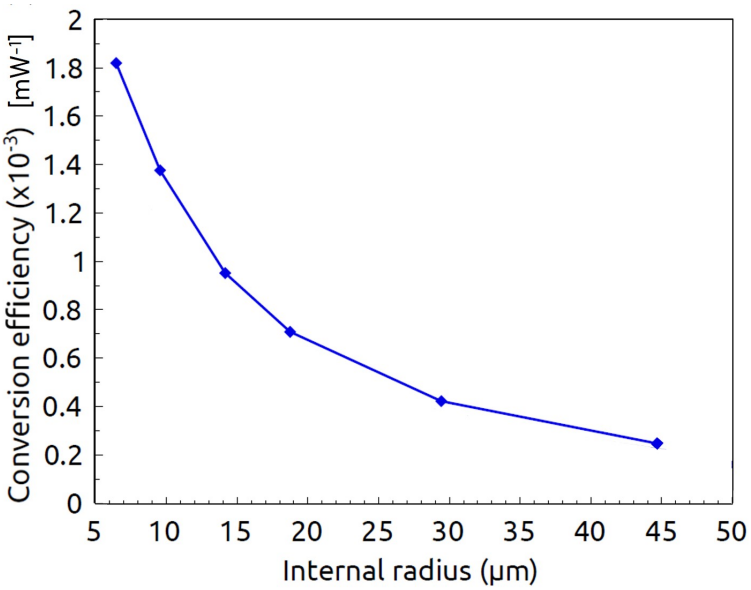

Figure 4.7: Conversion efficiency as a function of the internal radius for a microring with $w = 800$ nm and a microring thikness $e = 280$ nm

Concerning the thickness, the results are shown in figure 4.8. The conversion efficiency is not monotonous with the thickness of the microring waveguide.

The optimal geometry is a compromise between the experimental, the fabrication and the theoretical requirements. Figure 4.7 shows that the best conversion efficiencies are obtained with small radii. On the other hand, fig-

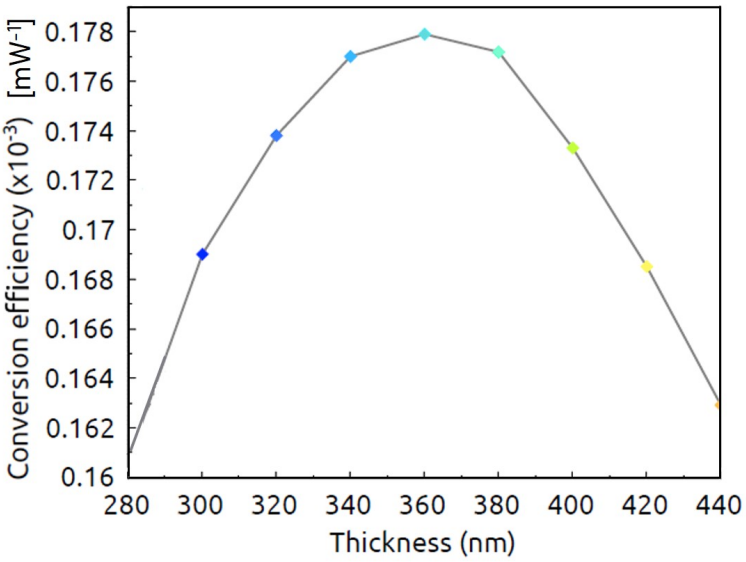

Figure 4.8: Conversion efficiency as a function of the thickness of the waveguide for a microring of $w = 800nm$ and an internal radius as close as possible to $R_{in} = 60$ μm. This because it is not possible to fix the value of the radius for a given cross section geometry. Actually, it must correspond to an integer for the azimuthal numbers.

ure 4.5 shows that to avoid two photon absorption of the fundamental mode with a small radius, $w \geq 900$ is needed to keep $e \geq 280$ nm.

Of particular interest in figure 4.8 is the region in which the conversion efficiency flattens around $e = 360$. This means that there is a range where small variations in the thickness, given by the fabrication tolerance, do not change the results. Moreover, plotting the variation of the radius as a function of the thickness, as shown in figure 4.9, it is possible to see that there is a flat maximum around $e = 330$ nm. So, for the same radius there is a range of thicknesses values instead of a fixed thickness value.

In order to better investigate the properties of this region, the conversion efficiency of a microring with $m_p = 400$, and $w = 800$ nm has been computed for two different radii: the first $R_{int} = 0.755$ μm, that corresponds to a thickness $e = 330$ nm, and the second $R_{int} = 57.208$ μm, that corresponds to a thickness $e = 440$ nm. The first radius has been chosen because is the the maximum in figure 4.9. So changing the thickness, the resonant condition is still satisfied. The second radius has been chosen far from this condition in order to have a comparison between the two situations. To simulate a fab-

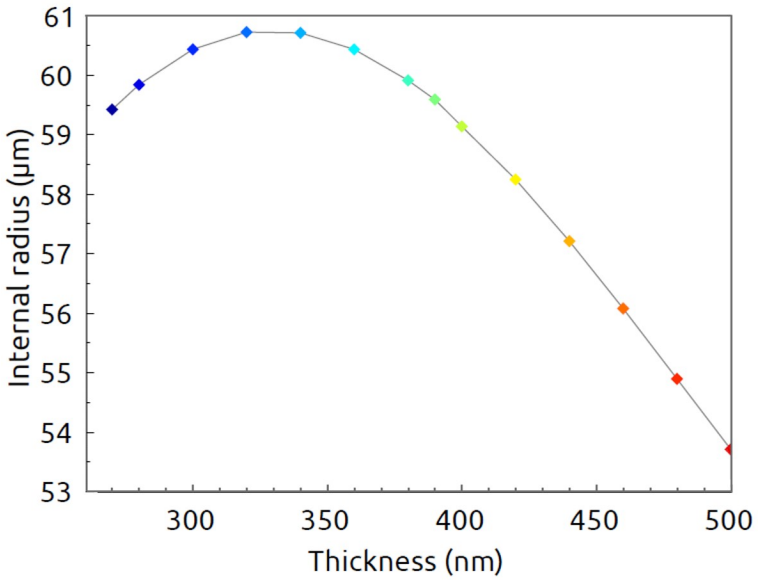

Figure 4.9: Internal radii values that allow SHG as a function of the waveguide thickness for a microring of width $w = 800$ nm and a fundamental azimuthal number $m_p = 400$. The colors of the points correspond to the same thicknesses used in figure 4.6.

rication error the thickness is swept around the nominal value and for each new thickness, the fundamental wavelength is adjusted around 2.3 μm to keep the fundamental mode resonant with $m = 400$. This can be easily done during an experiment by tuning the pump wavelength so that this simulative process reflects the experimental process. On the other side, SH is not resonant, thus in order to compute η_{SH} a pseudo-azimuthal number m'_{SH} is interpolated between the closest resonances. The results are shown in figure 4.10. The maximum of the conversion efficiency is $\eta_{SH} = 1.7 \times 10^{-4}$ mW^{-1} for both the two geometries. For the first geometry (green) the SHG remains efficient in a range of 10 nm and it is larger than 10^{-4} mW^{-1} in a range of 16 mm. For the second geometry (red) $\eta_{SH} > 10^{-4}$ mW^{-1} only in a range of 1 nm. So the first geometry is robust against thickness error, that affects in a critical way the other parameters.

During the fabrication process errors can occur in the radius of the microring, as well. The effect of this error has been investigated fixing the thickness while keeping other parameters as for fiure 4.10. The results are shown in figure 4.11. In both the geometries $\eta_{SH} > 10^{-4}$ mW^{-}1 in a range larger that

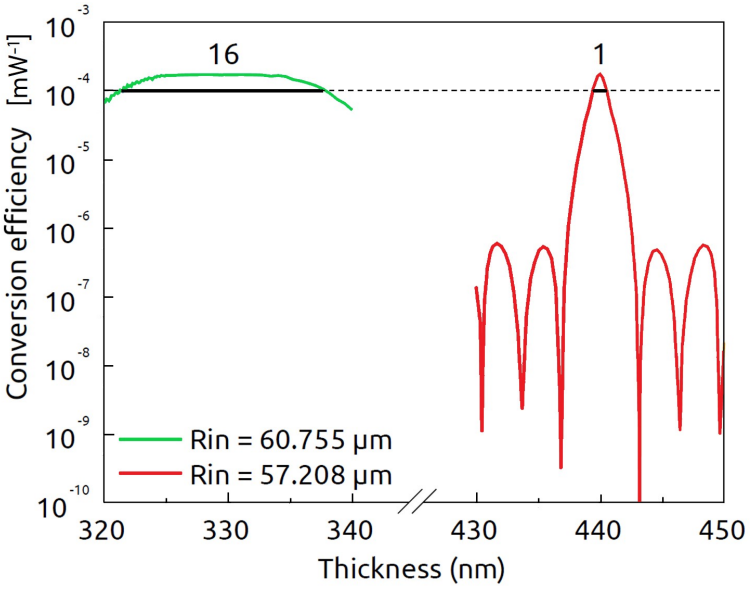

Figure 4.10: Effects of the thickness oscillations in two different geometries. It is visible that the green geometry allows to accommodate the fabrication errors of the thickness.

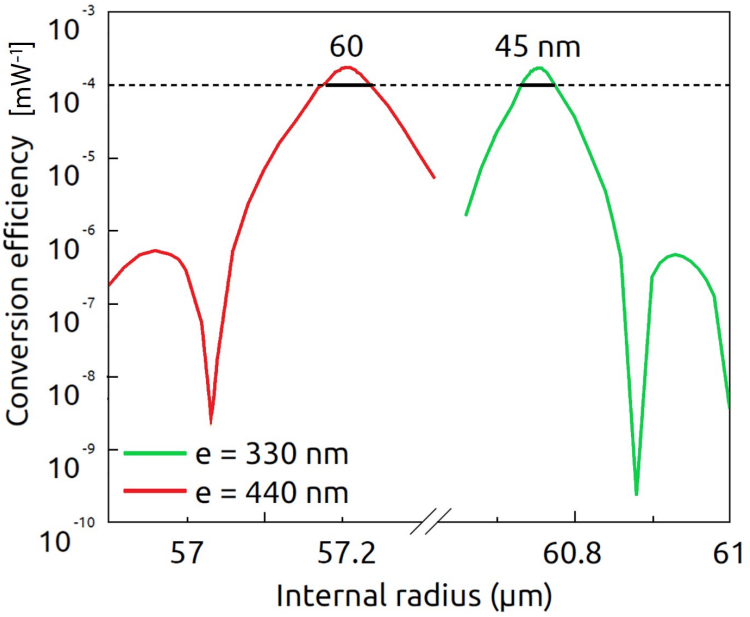

Figure 4.11: Effects of the radius oscillations in the two different geometries. The oscillations on the radius are not as critical as the one on the thickness.

40 nm, so the variations of the radius are not critical. The value of η_{SH} is lower respect to the one find in GaAs [11] but is in agreement with the result reported by Lake et al. ($\eta_{SH} = 3.8 \pm 0.2 \times 10^{-4}$ mW^{-1}) [64]. Moreover, thanks to he use of p-i-n junctions it is possible to increase the value of $\chi^{(2)}$ (and consequently η_{SH}) increasing the applied reverse bias.

4.4 The $\bar{4}$ symmetry

The only relevant assumption in this section is the $\bar{4}$ symmetry for the $\chi^{(2)}$. This assumption is general. There are several materials that show this symmetry of the second order susceptibility tensor. In literature this symmetry has been observed in several III-V semiconductors like AlN, GaN, GaAs, InP and their alloys [65, 66, 67, 68, 64]. The method can be used for all the materials that show this kind of symmetry, in order to find the robust geometries for the desired systems.

Further studies are now needed to find a way to preserve this simmetry in Silicon in order to take advantage of this kind of geometries.

Chapter 5

Conclusion

In Chapter 2 the origin of SHG in strained silicon waveguides has been investigated in a complete way. An experiment that allows to separate the strain effect from the effect of the charged defects has been performed. It was demonstrated that the second harmonic generation efficiency is not influenced by the increase of the strain in the waveguide. It was also demonstrated that passivating the charges at the Si/SiN interface allows to remove the SHG. This results point out that the origin of second order nonlinearities in strain silicon waveguides is strictly linked to the dangling bonds at the interfaces between the waveguide and the stressing layer. It is possible to fix an upper limit of $\chi^{(2)}$ due to the strain at 0.05 pm/V. This result is also supported by a previous theoretical estimation proposed by Khurgin et al. [46].

In Chapter 3 it was demonstrated a new method to generate a controlled $\chi^{(2)}$ in silicon waveguides based on the results of Chapter 2. Starting from the work of Timurdogan et al. [53] periodic p-i-n junctions have been fabricated across the waveguides to generate an electric E_{DC} field in their core. Moreover, the poling of the junctions is used to guarantee quasi phase-matching condition. Two different configurations of poling have been studied: the *simple poling configuration*, where the same kind of doping is on the same side of the junction, and the *interdigitated poling configuration*, where the sign of the junctions is alternated along the waveguide. It was demonstrated that the use of the interdigitated poling configuration increases the generation efficiency because it maximize the variation of E_{DC}. Also, a modeling of the effects of fabrication defects has been performed. The modeling shows how these

defects broaden and weaken the SHG spectrum. The founded geometrical variation are compatible with the waveguide fabrication process resolution. An estimation of the potentiality of the effective second order nonlinearity in the ideal case has been calculated. The values estimated in this work is $\Delta\chi^{(2)}_{eff} = 78 \pm 0.3$ pm/V at 24 V of applied bias, which is higher than the ones reported in ref [53] using simple poling configuration waveguides.

In Chapter 4 it was shown a study of microrings that can accomodate geometrical defects. Using a $\bar{4}$-symmetry of the $\chi^{(2)}$ tensor, a study of the conversion efficiency as a function of the different parameters of the microring as been performed. It was demonstrated that the most critical parameter is the thickness of the waveguide in the ring and it was shown a method to find a geometry that allows to have efficient conversion efficiency in a range of thickness of 16 nm around the nominal value. Moreover, this method is more general, since it is based only on the symmetry of the nonlinear tensor. Therefore, it can be easily applied to other materials.

The outcome of my thesis is a clear demonstration that the presence of an E_{DC} field in the core of the waveguide is the source of SHG in strained silicon waveguide. I demonstrated as well how this field can be engineered in order to control the value of the $\chi^{(2)}$ with poled waveguide. I have also proposed an innovative design of the poling to enhance the SHG strength. Moreover, I proposed a model that can describe in a complete way SHG in poled waveguide, highlighting a new method to control the effects of the undesired fabrication defects. Finally, I showed how is possible to use a $\bar{4}$-symmetric $\chi^{(2)}$ to find a set of microring geometries that are robust against fabrication imperfections. These geometries will be used in the future studies about a microring designs to obtain a comb generation.

Appendix A: Spitfire Pro System Amplifier

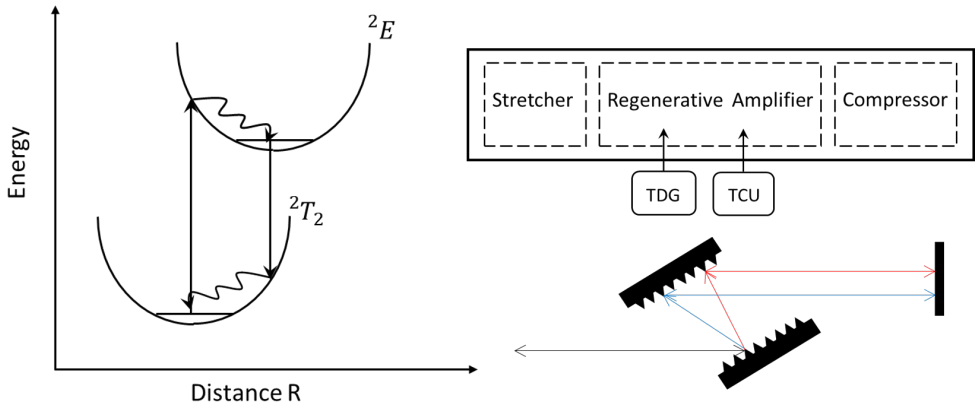

Figure 5.1: on the left: sketch of a 4 level laser operational process. The strong interaction between the photons and the lattice phonons causes a shift of the equilibrium distance between the different atoms in the lattice changing the electronic level of the different atomic orbital. When an electron jumps in the excited level, it then phononically decays on the bottom of the potential. From this situation it then decays on the lower electric level in a radiative way and finally it phononically decays on the ground of the energy system. In this kind of laser the absorption band and the emission band are different. In this way it is possible to use a first source (pump source) to guarantee a constant population inversion and a second source (seed source) to stimulate the emission of the laser. In the Ti:sapph laser the absorption band is from 400 nm to 600 nm and the emission band is from 670 nm to 1000 nm. On the right: at the top, sketch of the three different part of the Regenerative Amplifier and at the bottom, sketch of the stretcher operation system in which bluer wavelengths do a longer path respect to the redder ones.

The Spectra-Physics Millennia® amplifier is based on chirped pulse amplification. In the chirped pulse amplification, the pulse is first stretched in order to reduce the peak power, then it is amplified and finally it is recompressed to obtain the desired pulse width.

The Spitfire Pro System is divided in three different steps, as shown in figure 5.1: the stretcher, the regenerative amplifier and the compressor. The stretcher is composed by two different diffraction gratings that separate the different wavelengths and force the short wavelengths to follow a longer path respect to the long wavelengths (see the bottom left sketch in figure 5.1). In this way the pulse is stretched and the peak power is reduced. This allows the pulse to pass trough the crystal of the amplifier without damaging it. The stretched Tsunami pulse is used as a seed, while a separate 20 W laser at 527 nm with a repetition rate of 1 kHz (Spectra-Physics Empower®) is used as pump beam. The active medium of the amplifier is a Ti:sapphire crystal. This act as a 4-level laser cristal. In a 4-level crystal the strong interaction between the photons and the lattice phonons causes a shift of the equilibrium distance between the different atoms in the lattice changing the electronic levels. In this way the electron in the excited level first phononically decays on the bottom of the potential, then it decays on the lower electric level in a radiative way and finally it decays by multi phonon emission on the ground state. The empower guarantees to have a constant population inversion in the gain medium in order to have a large gain available in the cavity. Furthermore, the Spitfire Pro amplification cavity is designed to select and optically confine an individual pulse, so the gain of the amplifier can be concentrated in fewer pulses, thus producing more energy per pulse. To select single pulses pockels cells are used. A pockels cell is an electro-optic device that, with a properly applied voltage, acts as a $1/4$ waveplate, rotating the polarization by 45° each time a pulse passes trough it. The cavity, sketched in figure 5.2, is designed to trap vertically polarised light. The seed pulse after being stretched, passes trough 2 pockels cells. When the two cells are activated the polarization pulse is rotated by 90° and is reflected by the polarized mirror placed in the cavity entrance, while when the cells are deactivated the pulse passes without been modified end enters in the cavity. Once the pulse is in the cavity it passes trough a third pockels cell and the sapphire doped crystal, and is then reflected back by a mirror. When the pockels cell is deactivated the dou-

ble passage trough a $\lambda/4$ plate rotates the pulse polarization by 90° trapping the pulse in the cavity, whereas when the cell is activated the double passage trough the $\lambda/4$ plate and the pockels cell leaves the polarization unchanged and the beam can pass the polarized mirror and exit the cavity. The timing of the activation and deactivation of pockels cells is used to trap the seed pulses in the cavity and eject them once they have reached their maximum amplification. The pockels cells are controlled by a Timing and Delay Generator (TDG). The amplification cavity is also equipped with a Temperature Control Unit (TCU) that keeps the crystal temperature to a constant value. After the amplification the pulse is directed into the compressor. This has the same structure of the stretcher but is designed to have bluer wavelengths travel a shorter path than the redder ones, compressing in this way the pulse to the desired duration.

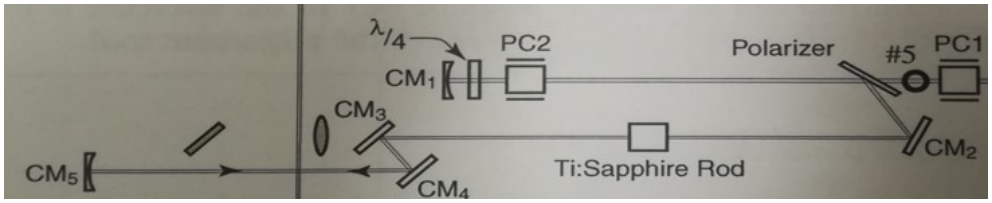

Figure 5.2: Sketch of the regenerative amplifier's cavity. The two pockels cells outside the cavity (PC1 and PC3 not visible in the image) rotate the polarization of the beam allowing it to pass through the polarizer. The third pockels cell inside the cavity (PC2) is used to trap the beam in the cavity. Image taken from the user's manual of the Spectra-Physics Spitfire Pro System®

Appendix B: Conversion Efficiency

The conversion efficiency η_{SH} has been defined in chapter 3 as:

$$\eta_{SH} = \frac{P_{out,SH}}{P_{in,p}^2} \tag{5.1}$$

where $P_{in,p}$ is the pump power in the waveguide before the coupling with the ring and $P_{out,SH}$ is the SH power in the waveguide after the coupling region. Following [11] and referring to figure 4.1(a)

$$\begin{cases} P_{out,SH} = |\mathbf{b_1}|^2 \\ P_{out,p} = |\mathbf{a_1}|^2 \end{cases} \tag{5.2}$$

it is possible to write the conversion efficiency as

$$\eta = \left| \frac{\mathbf{b_{1,SH}}}{\mathbf{a_{1,p}}^2} \right|^2 . \tag{5.3}$$

The relation between $\mathbf{b}_1$, $\mathbf{b}_2$ and $\mathbf{a}_1$, $\mathbf{a}_2$ is:

$$\begin{bmatrix} \mathbf{b_1} \\ \mathbf{b_2} \end{bmatrix} = \begin{bmatrix} t & k \\ -k^* & t^* \end{bmatrix} \begin{bmatrix} \mathbf{a_1} \\ \mathbf{a_2} \end{bmatrix} \tag{5.4}$$

with

$$det \begin{bmatrix} t & k \\ -k^* & t^* \end{bmatrix} = 1 \tag{5.5}$$

due to the energy conservation.

While $\mathbf{a}_1$, $\mathbf{a}_2$, $\mathbf{b}_1$ and $\mathbf{b}_2$ are the amplitudes of the electric field, it is also useful to write the electric field in the waveguide and in the ring. A general electric field in a waveguide can be written as

$$\begin{aligned}\mathbf{E} &= \sum_{m'p'q'} \left(A_{m'p'q'}(TM) + B_{m'p'q'}(TE)\right) = \\ &= \sum_{m'p'q'} \left(A_{m'p'q'}\widetilde{E}^{SH}_{m'p'q'}(z)\mathbf{u}_z + B_{m'p'q'}\widetilde{E}^{SH}_{m'p'q'}(r)\mathbf{u}_r\right) e^{i(\omega_{SH}t - m'\theta)}\end{aligned} \tag{5.6}$$

with $\widetilde{E}^{SH}_{m'p'q'}$ so that $\left|A_{m'p'q'}\right|^2 = P(TM)_{m'p'q'}$ power of the TM mode and $\left|B_{m'p'q'}\right|^2 = P(TE)_{m'p'q'}$ power of the TE mode.

For the nonlinear polarization vector is possible to write

$$\Delta\mathbf{E}^{SH} - \mu_0\varepsilon\frac{\partial^2\mathbf{E}^{SH}}{\partial t^2} = \mu_0\frac{\partial^2\mathbf{P}^{NL}}{\partial t^2}. \tag{5.7}$$

In this design a pump in the TE1 mode is used to obtain a SH in the TM3 mode. Hence, it is possible to project the SH electric field along z and obtain via 5.7:

$$\sum_{m'p'q'}\left(-\frac{i}{r^2}2m'\widetilde{E}^{SH}_{m'p'q'}\frac{dA_{m'p'q'}(\theta)}{d\theta}e^{i(\omega_{SH}t+m'\theta)}\right) = -\mu_0\omega^2_{SH}P^{NL}_z. \tag{5.8}$$

Since the SH mode is a TM3 mode, $q' = 1$ and $p' = 3$. Projecting on the single mode it is possible to obtain:

$$\begin{aligned}&\sum_{m'p'q'}\int_0^{+\infty}dr\int_0^{2\pi}d\theta\int_{-\infty}^{+\infty}dz - 2im'\frac{dA_{m'p'q'}(\theta)}{d\theta}e^{i(m-m')\theta}e^{-i\omega_{SH}t}\frac{1}{r}\widetilde{E}^{SH}_{m'p'q'}\widetilde{E}^{SH*}_{mpq} = \\ &= -\mu_0\omega^2_{SH}\int_0^{+\infty}dr\int_0^{2\pi}d\theta\int_{-\infty}^{+\infty}dzrP^{NL}_z e^{im\theta}\widetilde{E}^{SH*}_{m'p'q'}.\end{aligned} \tag{5.9}$$

It is now possible to extract the θ-dependent part from the integrals:

$$\sum_{m'p'q'} \int_0^{2\pi} d\theta \left(-2im' e^{i(m-m')\theta} e^{i\omega_{SH}t} \frac{dA_{m'p'q'}(\theta)}{d\theta} \right) \int_0^{+\infty} dr \int_{-\infty}^{+\infty} dz \frac{1}{r} E^{SH}_{m'p'q'} \widetilde{E}^{SH*}_{mpq} =$$
$$= -\mu_0 \omega_{SH}^2 \int_0^{+\infty} dr \int_0^{2\pi} d\theta \int_{-\infty}^{+\infty} dz r P_z^{NL} e^{im\theta} \widetilde{E}^{SH*}_{m'p'q'}. \tag{5.10}$$

The power of the electric field can be evaluated as:

$$P = \int \int_\Sigma \wp \cdot \hat{u}_\theta d\Sigma = \frac{1}{2} \int \int_\Sigma \Re \left(\mathbf{E} \times \mathbf{H}^* \right) \hat{u}_\theta d\Sigma = |A|^2 \tag{5.11}$$

where $\wp$ is the poynting vector. From Maxwell's equations

$$\widetilde{H}_r = \frac{m}{\mu_0 r \omega_{SH}} A_{mpq} \widetilde{E}_z \tag{5.12}$$

and using 5.12, the poynting vector can be written as:

$$\wp = \frac{1}{2} \Re \left(\mathbf{E} \times \mathbf{H}^* \right) = \frac{1}{2} \Re \left(E_z H_r^* \right) = \frac{1}{2} \Re \left[A_{mpq} \widetilde{E}_z \left(\frac{m}{\mu_0 r \omega_{SH}} A_{mpq} \widetilde{E}_z \right)^* \right] =$$
$$= \frac{1}{2} \Re \left[\frac{m \left| A_{mpq} \right|^2}{\mu_0 r \omega_{SH}} \left| \widetilde{E}_z \right|^2 \right]. \tag{5.13}$$

Using the form of the poynting vector of 5.13 in 5.11 the result is

$$\frac{1}{2} \frac{m \left| A_{mpq} \right|^2}{\mu_0 \omega_{SH}} A_{mpq} \int_0^{+\infty} dr \int_{-\infty}^{+\infty} dz \frac{1}{r} \left| \widetilde{E}_z \right|^2 = \left| A_{mpq} \right|^2 \tag{5.14}$$

that yields to:

$$\int_0^{+\infty} dr \int_{-\infty}^{+\infty} dz \frac{1}{r} \left| \widetilde{E}_z \right|^2 = \frac{2\mu_0 \omega_{SH}}{m}. \tag{5.15}$$

Using this results it is possible to solve equation 5.10:

$$\sum_{m'p'q'} \int_0^{2\pi} d\theta \left(-2im' e^{i(m-m')\theta} e^{i\omega_{SH}t} \frac{dA_{m'p'q'}(\theta)}{d\theta} \right) \frac{2\mu_0\omega_{SH}}{m} \delta_{pp'}\delta_{qq'} = \\ = \sum_{m'} \int_0^{2\pi} -2im' \frac{2\mu_0\omega_{SH}}{m} e^{i\omega_{SH}t} e^{i(m-m')} \frac{dA_{m'pq}(\theta)}{d\theta} d\theta. \tag{5.16}$$

In the undepleted pump approximation $\frac{dA_{m'pq}(\theta)}{d\theta} \sim const.$ It can be used this approximation to solve the θ integral:

$$\sum_{m'p'q'} -2im' \frac{2\mu_0\omega_{SH}}{m} e^{i\omega_{SH}t} \frac{dA_{m'pq}(\theta)}{d\theta} \int_0^{2\pi} e^{i(m-m')\theta} d\theta \\ = \sum_{m'p'q'} -2im' \frac{2\mu_0\omega_{SH}}{m} e^{i\omega_{SH}t} \frac{dA_{m'pq}(\theta)}{d\theta} 2\pi\delta_{m-m'} = \\ = -8\pi i\mu_0\omega_{SH} e^{i\omega_{SH}t} \frac{dA_{mpq}(\theta)}{d\theta}. \tag{5.17}$$

Recalling 5.10:

$$8\pi i e^{i\omega_{SH}t} \frac{dA_{mpq}(\theta)}{d\theta} = \omega_{SH} \int_0^{+\infty} \int_{-\infty}^{+\infty} \int_0^{2\pi} r P_z^{NL} e^{im\theta} \widetilde{E}_{mpq}^{SH*} dr dz d\theta. \tag{5.18}$$

In order to continue the evaluation of this integral the geometry of the $\chi^{(2)}$ tensor has to be fixed. In this work it has been chosen a $\bar{4}$ symmetric geometry ($\chi^{(2)}_{zxy} \neq 0$). Using 1.5 it is possible to define the nonlinear polarization along the z direction as

$$P_z^{NL} = \varepsilon_0 2\chi^{(2)}_{zxy} E_x^{\omega} E_y^{\omega} = \\ = \varepsilon_0 2\chi^{(2)}_{xyz} \left(A_p \widetilde{E}_r^p cos(\theta) - A_p \widetilde{E}_\theta^p sen(\theta) \right) \left(A_p \widetilde{E}_r^p sen(\theta) + A_p \widetilde{E}_\theta^p cos(\theta) \right) e^{2i\left(\omega_p t - m_p\theta\right)} = \\ = 2\varepsilon_0 \chi^{(2)}_{xyz} e^{2i\left(\omega_p t - m_p\theta\right)} \left[A_p^2 \widetilde{E}_r^p \widetilde{E}_\theta^p cos(2\theta) + \left(\left(A_p \widetilde{E}_r^p \right)^2 - \left(A_p \widetilde{E}_\theta^p \right)^2 \right) sen(\theta) cos(\theta) \right] \tag{5.19}$$

where $A_p\widetilde{E}_r^p$ and $A_p\widetilde{E}_\theta^p$ are the r and θ components of the pump electric field respectively. Using Maxwell's equation it is possible to write E_r and E_θ as:

$$\begin{cases} E_r = \frac{im}{-ir\omega\varepsilon_r} H_z \\ E_\theta = \frac{i}{\varepsilon_0 n^2 \omega} \frac{\partial H_z}{\partial r}. \end{cases} \tag{5.20}$$

Using 5.19 and 5.20 in 5.18 the result is

$$
\begin{aligned}
8\pi e^{i\omega_{SH}t}\frac{dA}{d\theta} &= \omega_{SH}\int_0^{+\infty}\int_{-\infty}^{+\infty}\int_0^{2\pi} 2r\varepsilon_0\chi^{(2)}_{zxy}e^{2i\omega_p t}e^{i\left(m-2m_p\right)\theta}\left[A_p^2\widetilde{E}_r^p\widetilde{E}_\theta^p cos(2\theta)+\right.\\
&\left.+A_p^2\left(\left(\widetilde{E}_r^p\right)^2-\left(\widetilde{E}_\theta^p\right)^2\right)sen(\theta)cos(\theta)\right]\widetilde{E}^{SH*}drdzd\theta =\\
&= \omega_{SH}\int_0^{+\infty}\int_{-\infty}^{+\infty}\int_0^{2\pi} 2r\varepsilon_0\chi^{(2)}_{zxy}e^{2i\omega_p t}e^{i\left(m-2m_p\right)\theta}\left[A_p^2\frac{-m_p}{r\varepsilon_0 n_p^2\omega_p}\widetilde{H}_z^p\frac{i}{\varepsilon_0 n_p^2\omega_p}\right.\\
&\left.\frac{\partial\widetilde{H}_z^p}{\partial r}+A_p^2 sen(\theta)cos(\theta)\left(\left(\frac{-m_p}{r\varepsilon_0 n_p^2\omega_p}\widetilde{H}_z^p\right)^2-\left(\frac{i}{r\varepsilon_0 n_p^2\omega_p}\frac{\partial\widetilde{H}_z^p}{\partial r}\right)^2\right)\right] =\\
&= \omega_{SH}\int_0^{+\infty}\int_{-\infty}^{+\infty}\int_0^{2\pi}\frac{2rA_p^2}{\varepsilon_0^2 n_p^4\omega_p^2}\chi^{(2)}_{zxy}e^{2i\omega_p t}e^{i\left(m-2m_p\right)\theta}\left[-\frac{im_p}{r}\widetilde{H}_z^p\frac{\partial\widetilde{H}_z^p}{\partial r}\right.\\
&\left.cos(2\theta)+\frac{m_f^2}{r^2}\left(\widetilde{H}_z^p\right)^2\frac{1}{2}sen(2\theta)+\left(\frac{\partial\widetilde{H}_z}{\partial r}\right)^2\frac{1}{2}sen(2\theta)\right]\widetilde{E}^{SH*}drdzd\theta.
\end{aligned}
\tag{5.21}
$$

Defining:

$$
C=\frac{2rA_p^2}{\varepsilon_0 n_p^4\omega_p^2}\chi^{(2)}_{zxy}e^{2i\omega_p t} \tag{5.22}
$$

and

$$
\Delta m = m-2m_p \tag{5.23}
$$

it is possible to write:

$$
\begin{aligned}
8\pi e^{i\omega_{SH}t}\frac{dA}{d\theta} &= \omega_{SH}\int_0^{+\infty}\int_{-\infty}^{+\infty}\int_0^{2\pi} Ce^{i\Delta m\theta}\left[-\frac{im_p}{r}\widetilde{H}_z^p\frac{\partial\widetilde{H}_z^p}{\partial r}\frac{e^{i2\theta}+e^{-i2\theta}}{2}+\right.\\
&\left.+\left(\frac{m_p}{r^2}\right)^2\left(\widetilde{H}_z^p\right)^2+\left(\frac{\partial\widetilde{H}_z^p}{\partial r}\right)^2\right]\frac{1}{2}\frac{e^{i2\theta}-e^{-i2\theta}}{2i}\widetilde{E}^{SH*}drdzd\theta =\\
&= -\omega_{SH}\int_0^{+\infty}\int_{-\infty}^{+\infty}\int_0^{2\pi} Ce^{i(\Delta m-2)\theta}\frac{1}{4i}\left[\frac{m_p}{r}\widetilde{H}_z^p-\frac{\partial\widetilde{H}_z^p}{\partial r}\right]^2\widetilde{E}^{SH*}drdzd\theta.
\end{aligned}
\tag{5.24}
$$

As explained in section 4.1, $2m_p - m_{SH} = 2$, and so $\Delta m = -2$. Now it is possible to write:

$$32\pi e^{i\omega_{SH}t}\frac{dA_{SH}}{d\theta} = -\omega_{SH}\int_0^{+\infty}\int_{-\infty}^{+\infty}\int_0^{2\pi} Ce^{i4\theta}\left[\frac{m_p}{r}\widetilde{H}_z^p + \frac{\partial\widetilde{H}_z^p}{\partial r}\right]^2 \widetilde{E}^{SH*}drdzd\theta + \\ + \omega_{SH}\int_0^{+\infty}\int_{-\infty}^{+\infty}\int_0^{2\pi} C\left[\frac{m_p}{r}\widetilde{H}_z^p - \frac{\partial\widetilde{H}_z^p}{\partial r}\right]^2 \widetilde{E}^{SH*}drdzd\theta. \tag{5.25}$$

From this equation it is possible to obtain for A_{SH}:

$$\frac{dA_{SH}}{d\theta} = \frac{-\omega_{SH}A_p^2}{\varepsilon_0 n_p^4\omega_p^2 16\pi}\chi_{zxy}^{(2)}e^{i\left(\omega_{SH}-2\omega_p\right)t}\left\{-2\pi\int\int_\Sigma r\left[\frac{m_p}{r}\widetilde{H}_z^p - \frac{\partial\widetilde{H}_z^p}{\partial r}\right]^2\widetilde{E}^{SH*}d\Sigma\right\} \\ = \frac{A_p^2}{4\epsilon_0\omega_f n_f^4}\chi_{zxy}^{(2)}\left\{\int\int_\Sigma r\left[\frac{m_p}{r}\widetilde{H}_z^p - \frac{\partial\widetilde{H}_z^p}{\partial r}\right]^2\widetilde{E}^{SH*}d\Sigma\right\}. \tag{5.26}$$

Writing $\widetilde{E}_z$ and $\widetilde{H}_z$ as function of E_z and H_z:

$$\begin{cases}\widetilde{E}_z = E_z\sqrt{\frac{2\mu_0\omega}{mN}} \\ \widetilde{H}_z = H_z\sqrt{\frac{2\epsilon_0 n^2\omega}{mN}}.\end{cases} \tag{5.27}$$

Given the normalization constant N:

$$N = \int\int\frac{|E_z|^2}{r}d\Sigma, \tag{5.28}$$

it can be obtained:

$$\frac{dA_{SH}}{d\theta} = A_p^2\frac{1}{2n_p^2 m_p N_p}\sqrt{\frac{2\mu_0\omega_{SH}}{m_{SH}N_{SH}}}\left\{\int\int_\Sigma r\left[\frac{m_p}{r}H_z^p - \frac{\partial H_z^p}{\partial r}\right]^2 E_z^{SH*}d\Sigma\right\}. \tag{5.29}$$

Recalling equation 5.3, $\mathbf{a}_{1,p}$ is the pump power while $\mathbf{b}_{1,SH} = \mathbf{a}_{2,SH}k_{SH}$. $\mathbf{a}_{2,SH}$ can be evaluated as:

$$A_{SH}(2\pi) - A_{SH}(0) = \frac{\mathbf{a}_{2,SH}}{\hat{\alpha}_{SH}e^{i\phi}} - \mathbf{b}_{2,SH} \tag{5.30}$$

where $\hat{\alpha}_{SH}$ is the absorption of the material at the SH wavelength λ_{SH}, ϕ is the phase of the mode and $\mathbf{b}_{2,SH} = t^*_{SH}\mathbf{a}_{2,SH}$. From equation 5.29:

$$A_{SH}(2\pi) - A_{SH}(0) = 2\pi(A_p^2)K \tag{5.31}$$

where K is a constant that can be evaluated using comsol from equation 5.29. Since $A_p = \mathbf{b}_{2,p} = \mathbf{a}_{2,p}$ due to the undepleted pump approximation, it is so possible to write

$$2\pi \left|\mathbf{b}_{2,p}\right|^2 K = \frac{\mathbf{a}_{2,SH}}{\hat{\alpha}_{SH}e^{i\phi}} - t^*_{SH}\mathbf{a}_{2,SH} = \left(\frac{1 - t^+_{SH}\hat{\alpha}_{SH}e^{i\phi}}{\hat{\alpha}_{SH}e^{i\phi}}\right)\mathbf{a}_{2,SH}. \tag{5.32}$$

It is now possible to evaluate $\mathbf{a_{2,SH}}$ as:

$$\begin{aligned}\mathbf{a}_{2,SH} &= \frac{\hat{\alpha}_{SH}e^{i\phi}}{1 - t\hat{\alpha}_{SH}e^{i\phi}} 2\pi \left|\mathbf{a}_{2,p}\right|^2 K = \\ &= \frac{(2\pi\hat{\alpha}_{SH}cos(\phi)) - i\,(2\pi\hat{\alpha}_{SH}sen(\phi))}{(1 - t\hat{\alpha}_{SH}cos(\phi)) - i\,(t\hat{\alpha}_{SH}sen(\phi))} \left|\mathbf{a}_{2,p}\right|^2 K\end{aligned} \tag{5.33}$$

in wich $\mathbf{a}_{2,p} = \mathbf{b}_{2,p}$ can be evaluated as $\mathbf{a}_{1,p}k^*_p$.

Now to determine η_{SH}, the losses $\hat{\alpha}$, coefficients t and k have to be determined. The losses $\hat{\alpha}$ are related to the *Q-factor* of the ring and the coefficients k and t are related to the coupling. So, in order to determine η_{SH}, the coupling between the bus and the ring and the *Q-factor* of the ring have to be determined.

The coupling between the ring and the bus can be evaluated with the *overlap integrals method*. This method consists in the study of the overlap in the ring cross section of two different optical modes: the one generated by the ring and the one generated by the bus. In order to evaluate the two fields, two different situations have been simulated. In the first situation only the ring is present and in the second only the bus. With the results of these simulations it is possible to evaluate to overlap of the two electric fields and to normalize it on the poynting vector evaluated in all the space:

$$k^* = \frac{\omega\epsilon_0 \int \int_{\Sigma_{tot}} n_{Si}^2 \left(\mathbf{E}_{bus}^* \mathbf{E}_{ring}\right) d\Sigma}{\int \int_{\Sigma_{tot}} \wp d\Sigma}. \tag{5.34}$$

where E_{ring} is the electric field generated by the ring, E_{bus} is the electric field generated by the bus and Σ_{tot} is the total area. The same can be done for k:

$$k = \frac{\omega\epsilon_0 \int \int_{\Sigma_{tot}} n_{Si}^2 \left(\mathbf{E}_{ring}^* \mathbf{E}_{bus}\right) d\Sigma}{\int \int_{\Sigma_{tot}} \wp d\Sigma}. \tag{5.35}$$

It is then possible to find t^* and t using the energy conservation:

$$(t^*)^2 = 1 - (k^*)^2 \tag{5.36}$$

and

$$t^2 = 1 - k^2 \tag{5.37}$$

It is important to notice that k_p^* and k_p at the pump wavelength are different from k_{SH}^* and k_{SH} at the second harmonic wavelength.

We need also to determine $\hat{\alpha}$ to evaluate η. $\hat{\alpha}$ is the absorption of the material and is linked to the intrinsic *Q-factor* via:

$$Q^{int} = \pi n \frac{\sqrt{\hat{\alpha}}}{1 - \hat{\alpha}} \tag{5.38}$$

where n is an integer number. Therefore, the intrinsic Q-factor depends on the fabrication facility. As a consequence it is so possible to extract the value of α for a known *Q-factor* as [69]:

$$\hat{\alpha} = \left| \frac{2(Q^{int})^2 + \pi^2 n^2 \pm \sqrt{\pi^4 n^4 + 4(Q^{int})^2 \pi^2 n^2}}{2(Q^{int})^2} \right|. \tag{5.39}$$

It is also possible to evaluate directly $\hat{\alpha}$ of the sample in a experimental way. Straight waveguides with different length can be used as test-structures

to extract the propagation losses α. Once it has the the propagation losses, it is possible to obtain the value of $\hat{\alpha}$ as:

$$\hat{\alpha} = e^{-2\alpha\pi R_{int}}. \tag{5.40}$$

Is important to notice that the losses change with the wavelength. This means that $\alpha_p \neq \alpha_{SH}$. This leads to the fact that even Q and $\hat{\alpha}$ evaluated for the pump mode are different from the ones evaluated for the SH mode.

Knowing it is possible to evaluate the conversion efficiency expression [63]:

$$\eta_{SH} = 4\pi^2 |K|^2 \frac{\hat{\alpha}_{SH}^2 \left(1 - t_{SH}^2\right)}{1 + \hat{\alpha}_{SH}^2 t_{SH}^2 - 2\hat{\alpha}_{SH} t_{SH} cos(\phi_{SH})} \left(\frac{\hat{\alpha}_p^2 \left(1 - t_p^2\right)}{1 + \hat{\alpha}_p^2 t_p^2 - 2\hat{\alpha}_p t_p cos(\phi_p)} \right)^2. \tag{5.41}$$

Bibliography

[1] Xiaoping Liu, Bart Kuyken, Gunther Roelkens, Roel Baets, Richard M. Osgood Jr, and William M. J. Green. Bridging the mid-infrared-to-telecom gap with silicon nanophotonic spectral translation. *Nature Potonics*, (6):667–671, September 2012. doi: 10.1038/nphoton.2012.221.

[2] Geoffrey New. In *Introduction to Nonlinear Optics*. Cambridge University Press, April 2011.

[3] R. W. Boyd. In *Nonlinear Optics, 3rd edition*. Academic Press, 2007.

[4] Claudio Castellan. *Second order nonlinearities in silicon photonics*. PhD thesis, University of Trento, 2019.

[5] Lucia Caspani, Chunle Xiong, Benjamin J. Eggleton, Daniele Bajoni, Marco Liscidini, Matteo Galli, Roberto Morandotti, and David J. Moss. Integrated sources of photon quantum states based on nonlinear optics. *light: science and applications*, 6(e17100), November 2017. doi: 10.1038/lsa.2017.100.

[6] J. Leuthold, C. Koos, and W. Freude. Nonlinear silicon photonics. *nature photonics*, (4):535–544, August 2010. doi: 10.1038/nphoton.2010.185.

[7] R. M. Osgood, N. C. Panoiu, J. I. Dadap, Xiaoping Liu, Xiaogang Chen, I-Wei Hsieh, E. Dulkeith, W. M.J. Green, and Y. A. Vlasov. Engineering nonlinearities in nanoscale optical systems: physics and applications in dispersion-engineered silicon nanophotonic wires. *Advances in Optics and Photonics*, 1(1):162–235, January 2009. doi: 10.1364/AOP.1.000162.

[8] S. Signorini, M. Mancinelli, M. Borghi, M. Bernard, M. Ghulinyan, G. Pucker, and L. Pavesi. Intermodal four-wave mixing in silicon waveg-

uides. *Photon. Res.*, 6(8):805–814, August 2018. doi: 10.1364/PRJ.6.000805.

[9] J.A. Giordmaine. Mixing of light beams in crystals. *Physical Review Letters*, 8(1):19–20, January 1962. doi: 10.1103/PhysRevLett.8.19.

[10] P. D. Maker, R. W. Terhune, M. Nisenoff, and C. M. Savage. Effects of dispersion and focusing on the production of optical harmonics. *Physical Review Letters*, 8(1):21–22, January 1962. doi: 10.1103/PhysRevLett.8.21.

[11] Paulina S. Kuo and Glenn S. Solomon. On- and off-resonance second-harmonic generation in gaas microdisks. *Optics Express*, 19(18):16898–16918, August 2011. doi: 10.1364/OE.19.016898.

[12] URL `https://sites.google.com/view/prin-nemo/home?authuser=0`.

[13] J.Reichert, R.Holzwarth, Th.Udem, and T.W.Hänsch. Measuring the frequency of light with mode-locked lasers. *Optics Communications*, 172 (1-6):59–68, december 1999. doi: 10.1016/S0030-4018(99)00491-5.

[14] R. Holzwarth, Th. Udem, T. W. Hänsch, J. C. Knight, W. J. Wadsworth, and P. St. J. Russell. Optical frequency synthesizer for precision spectroscopy. *Physical Review Letters*, 85(11), September 2000. doi: 10.1103/PhysRevLett.85.2264.

[15] Albert Schliesser, Nathalie Picqué, and Theodor W. Hänsch. Mid-infrared frequency combs. *Nature Photonics*, 6:440–449, July 2012. doi: 10.1038/nphoton.2012.142.

[16] Andreas Hugi, Gustavo Villares, Stéphane Blaser, H. C. Liu, and Jérôme Faist. Mid-infrared frequency comb based on a quantum cascade laser. *Nature Photonics*, 492:229–233, December 2012. doi: 10.1038/nature11620.

[17] Tobias J. Kippenberg, Ronald Holzwarth, and Scott A. Diddams. Microresonator-based optical frequency combs. *Science*, 332(6029):555–559, April 2011. doi: 10.1126/science.1193968.

[18] Iolanda Ricciardi, Simona Mosca, Maria Parisi, Pasquale Maddaloni, Luigi Santamaria, Paolo De Natale, and Maurizio De Rosa1. Frequency

comb generation in quadratic nonlinear media. *Physical Review A*, 063839 (91), June 2015. doi: 10.1103/PhysRevA.91.063839.

[19] Massimo Cazzanelli and Joerg Schilling. Second order optical nonlinearity in silicon by symmetry breaking. *Applied Physics Reviews*, (3):011104, March 2016. doi: 10.1063/1.4941558.

[20] Rune S. Jacobsen, Karin N. Andersen, Peter I. Borel, Jacob Fage-Pedersen, Lars H. Frandsen, Ole Hansen, Martin Kristensen, Andrei V. Lavrinenko, Gaid Moulin, Haiyan Ou, Christophe Peucheret, Beáta Zsigri, and Anders Bjarklev. Strained silicon as a new electro-optic material. *Nature*, 441(7090):199+, May 2006. doi: 10.1038/nature04706.

[21] Bartos Chmielak, Michael Waldow, Christopher Matheisen, Christian Ripperda, Jens Bolten, Thorsten Wahlbrink, Michael Nagel, Florian Merget, and Heinrich Kurz. Pockels effect based fully integrated, strained silicon electro-optic modulator. *Optic Express*, 19(18):17212–17219, August 2011. doi: 10.1364/OE.19.017212.

[22] Pedro Damas, Xavier Le Roux, David Le Bourdais, Eric Cassan, Delphine Marris-Morini, Nicolas Izard, Thomas Maroutian, Philippe Lecoeur, and Laurent Vivien. Wavelength dependence of pockels effect in strained silicon waveguides. *Optic Express*, 22:22095–22100, September 2014. doi: 10.1364/OE.22.022095.

[23] M. Cazzanelli, F. Bianco, E. Borga, G. Pucker, M. Ghulinyan, E. Degoli, E. Luppi, V. Véniard, S. Ossicini, D. Modotto, S. Wabnitz, R. Pierobon, and L. Pavesi. Second-harmonic generation in silicon waveguides strained by silicon nitride. *Nature Materials*, (11):148–154, December 2011. doi: 10.1038/nmat3200.

[24] S. Sharif Azadeh, F. Merget, M. P. Nezhad, , and J. Witzens. On the measurement of the pockels effect in strained silicon. *Optics Letters*, 40 (8):1877–1880, April 2015. doi: 10.1364/OL.40.001877.

[25] Irene Olivares, Todora Angelova, and Pablo Sanchis. On the influence of interface charging dynamics and stressing conditions in strained silicon devices. *Scientific Reports*, (7):7241, August 2017. doi: 10.1038/s41598-017-05067-9.

[26] M. Borghi, M. Mancinelli, F. Merget, J. Witzens, M. Bernard, M. Ghulinyan, G. Pucker, and L. Pavesi. High-frequency electro-optic measurement of strained silicon racetrack resonators. *Optics Letters*, 40 (22):5287–5290, November 2015. doi: 10.1364/OL.40.005287.

[27] Clemens Schriever, Federica Bianco, Massimo Cazzanelli, Mher Ghulinyan, Christian Eisenschmidt, Johannes de Boor, Alexander Schmid, Johannes Heitmann, Lorenzo Pavesi, and Jörg Schilling. Second-order optical nonlinearity in silicon waveguides: Inhomogeneous stress and interfaces. *Advanced Optical Material*, 3(1):129–136, January 2015. doi: 10.1002/adom.201400370.

[28] Malvin Carl Teich and Bahaa E A Saleh. In *Fundamentals of photonics*. Wiley New York, 1991.

[29] M Borghi, C Castellan, S Signorini, A Trenti, and L Pavesi. Nonlinear silicon photonics. *Journal of Optics*, 19(19):093002, August 2017. doi: 10.1088/2040-8986/aa7a6d.

[30] Claudio Castellan, Alessandro Trenti, Mattia Mancinelli, Alessandro Marchesini, Mher Ghulinyan, Georg Pucker, and Lorenzo Pavesi. From shg to mid-infrared spdc generation in strained silicon waveguides. *Proceedings in Quantum Photonic Devices*, 10358(1035804):1035804, August 2017. doi: 10.1117/12.2273641.

[31] Stefano Signorini, Mattia Mancinelli, Massimo Borghi, Martino Bernard, Mher Ghulinyan, Georg Pucker, and Lorenzo Pavesi. Intermodal four-wave mixing in silicon waveguides. *Photonics Research*, 6(8):805–814, July 2018. doi: 10.1364/PRJ.6.000805.

[32] A. D. Bristow, N. Rotenberg, and H. M. van Driel. Two-photon absorption and kerr coefficients of silicon for 850–2200nm. *Applied Physics Letters*, 90(191104), May 2007. doi: 10.1063/1.2737359.

[33] Gioele Piccoli, Martino Bernard, and Mher Ghulinyan. Permanent mitigation of loss in ultrathin silicon-on-insulator high-q resonators using ultraviolet light. *Optica*, 5(10):1271–1278, October 2018. doi: 10.1364/OPTICA.5.001271.

[34] D. T. Krick and P. M. Lenahan. Electrically active point defects in amorphous silicon nitride: An illumination and charge injection study. *Journal of Applied Physics*, 64(7):3558–3563, June 1988. doi: 10.1063/1.341499.

[35] W. L. Warren. Electron paramagnetic resonance investigation of charge trapping centers in amorphous silicon nitride films. *Journal of Applied Physics*, 74(6):4034–4046, June 1993. doi: 10.1063/1.355315.

[36] B. Cowan. Optical damage threshold of silicon for ultrafast infrared pulses. *Proc. SPIE 6720, Laser-Induced Damage in Optical Materials*, 6720 (67201M), Decemer 2007. doi: 10.1117/12.753720.

[37] Andrew M. Weiner. In *Ultrafast Optics*. Jhon Wiley & sons, October 2008.

[38] Jean-Claude Diels and Wolfgang Rudolph. In *Ultrashort Laser Pulse Phenomena, Second edition*. Academic Press, January 2006.

[39] Mathias Berciano, Guillaume Marcaud, Pedro Damas, Xavier Le Roux, Paul Crozat, Carlos Alonso Ramos, Diego Pérez Galacho, Daniel Benedikovic, Delphine Marris-Morini, Eric Cassan, and Laurent Vivien. Fast linear electro-optic effect in a centrosymmetric semiconductor. *Communications Physics*, 1(64), October 2018. doi: 10.1038/s42005-018-0064-x.

[40] Pedro Damas, Delphine Marris-Morini, Eric Cassan, and Laurent Vivien. Bond orbital description of the strain-induced second-order optical susceptibility in silicon. *Physical Review B*, 93(16):165208, April 2016. doi: 10.1103/PhysRevB.93.165208.

[41] C. Castellan, Alessandro Trenti, Chiara Vecchi, Alessandro Marchesini, Mattia Mancinelli, Mher Ghulinyan, Georg Pucker, and Lorenzo Pavesi. On the origin of second harmonic generation in silicon waveguides with silicon nitride cladding. *Scientific Reports*, 9(1088), January 2019. doi: 10.1038/s41598-018-37660-x.

[42] John Robertson and Martin J. Powell. Gap states in silicon nitride. *Applied Physics Letters*, 44(4):415, November 1984. doi: 10.1063/1.94794.

[43] John Robertson, William L.Warren, and Jerzy Kanicki. Nature of the si and n dangling bonds in silicon nitride. *Journal of Non-Crystalline Solids*, 187:297–300, July 1995. doi: 10.1016/0022-3093(95)00153-0.

[44] William L. Warren, John Robertson, and Jerzy Kanicki. Si and n dangling bond creation in silicon nitride thin films. *Applied Physics Letters*, 63(19): 2685, September 1993. doi: 10.1063/1.110420.

[45] Pedro A.L de S. Damas. *Pockels effect in strained silicon waveguides.* PhD thesis, Université Paris-Saclay, 2016.

[46] Jacob B. Khurgin, Todd H. Stievater, Marcel W. Pruessner, and William S. Rabinovich. On the origin of the second-order nonlinearity in strained si–sin structures. *Journal of the Optical Society of America B*, 32(12):2494–2499, November 2015. doi: 10.1364/JOSAB.32.002494.

[47] Gernot Pfanner, Christoph Freysoldt, Jörg Neugebauer, and Uwe Gerstmann. *Ab initio* epr parameters for dangling-bond defect complexes in silicon: Effect of jahn-teller distortion. *PHYSICAL REVIEW B*, 85(19): 195202, May 2012. doi: 10.1103/PhysRevB.85.195202.

[48] Simon M. Sze and Kwok K. Kg. In *Physics of Semiconductor, third edition*. John Wiley and Sons Inc, 2006.

[49] Peter Tidemand-Lichtenberg Karsten Rottwitt. In *Nonlinear Optics, Principles and Applications*. CRC Press, January 2015.

[50] J. Zhang, Q. Lin, G. Piredda, P. M. Fauchet, R. W. Boyd, and G. P. Agrawal. Anisotropic nonlinear response of silicon in the near-infrared region. *Applied Physics Letters*, 91(7):07113, August 2007. doi: 10.1063/1.2768632.

[51] Nick K. Hon, Richard Soref, and Bahram Jalali. The third-order nonlinear optical coefficients of si, ge, and si1-xgex in the midwave and longwave infrared. *Journal of Applied Physics*, 110(1):011301, July 2011. doi: 10.1063/1.3592270.

[52] Q. Lin, J. Zhang, G. Piredda, P.M. Fauchet, G.P. Agrawal, and W. Boyd. Dispersion of silicon nonlinearities in the near infrared region. *Applied Physics Letters*, 91(2):021111, July 2007. doi: 10.1063/1.2750523.

[53] E. Timurdogan, C. V. Poulton, M. J. Byrd, and M. R. Watts. Electric field-induced second-order nonlinear optical effects in silicon waveguides. *Nature Photonics*, 11(12):200–206, March 2017. doi: 10.1038/nphoton.2017.14.

[54] Milos Nedeljkovic, Richard Soref, and Goran Z. Mashanovich. Free-carrier electrorefraction and electroabsorption modulation predictions for silicon over the 1˜14 μm infrared wavelength range. *IEEE Photonics Journal*, 3(6):1171 – 1180, October 2011. doi: 10.1109/JPHOT.2011.2171930.

[55] Massimo Borghi, Mattia Mancinelli, Martino Bernard, Mher Ghulinyan, Georg Pucker, and Lorenzo Pavesi. Homodyne detection of free carrier induced electro-optic modulation in strained silicon resonators. *Journal of Lightwave Technology*, 34(24):5657–5668, November 2016.

[56] Govind Agrawal. In *Nonlinear Fiber Optics, fifth edition*. Academic Press, October 2013.

[57] Cmm, center for materials and microsystems. `https://cmm.fbk.eu/en/`.

[58] Riccardo Franchi, Claudio Castellan, Mher Ghulinyan, and Lorenzo Pavesi. Second harmonic generation in periodically poled silicon waveguides by lateral p-n junctions. *Optics Letters*, 45(12):31883191, June 2020. doi: 10.1364/OL.391988.

[59] Sten Helmfrid and Gunnar Arvidsson. Influence of randomly varying domain lengths and nonuniform effective index on second-harmonic generation in quasi-phase-matching waveguides. *Journal of the Optical Society of America B*, 8(4):797–804, september 1991. doi: 10.1364/JOSAB.8.000797.

[60] Claudio Castellan, Riccardo Franchi, Stefano Biasi, Martino Bernard, Mher Ghulinyan, and Lorenzo Pavesi. Field-induced nonlinearities in silicon waveguides embedded in lateral p-n junctions. *Frontiers in Physics*, (7:104), July 2019. doi: 10.3389/fphy.2019.00104.

[61] J. Heebner, R. Grover, and T. Ibrahim. In *Optical Microresonators: Theory, Fabrication, and Applications*. Springer, 2008.

[62] Yannick Dumeige and Patrice Féron. Whispering-gallery-mode analysis of phase-matched doubly resonant second-harmonic generation. *Physical Review A*, 74(6):063804, December 2006. doi: 10.1103/PhysRevA.74.063804.

[63] Pierre Guilleme, Chiara Vecchi, Claudio Castellan, Stefano Signorini, Mher Ghulinyan, Martino Bernard, Maria Parisi, and Lorenzo Pavesi. Robust geometries for second-harmonic-generation in microrings exhibiting a $\bar{4}$ symmetry. *Applied Sciences*, 10(24:904), December 2020. doi: 10.3390/app10249047.

[64] David P. Lake, Matthew Mitchell, Harishankar Jayakumar, Laís Fujii dos Santos, Davor Curic, , and Paul E. Barclay. Efficient telecom to visible wavelength conversion in doubly resonant gallium phosphide microdisks. *Applied Physics Letters*, 108(3):031109, January 2016. doi: 10.1063/1.4940242.

[65] Xiang Guo, Chang-Ling Zou, and Hong X. Tang. Second-harmonic generation in aluminum nitride microrings with 2500%/w conversion efficiency. *Optica*, 3(10):1126–1131, October 2016. doi: 10.1364/OPTICA.3.001126.

[66] I. Roland, M. Gromovyi, Y. Zeng, M. El Kurdi, S. Sauvage, C. Brimont, T. Guillet, B. Gayral, F. Semond, J. Y. Duboz, M. de Micheli ans X. Checoury, and P. Boucaud. Phase-matched second harmonic generation with on-chip gan-on-si microdisks. *Scientific Reports*, 6(34191), September 2016. doi: 10.1038/srep34191.

[67] S. Mariani, A. Andronico, A. Lemaître, I. Favero, S. Ducci, , and G. Leo. Second-harmonic generation in algaas microdisks in the telecom range. *Optics Letters*, 39(10):3062–3065, May 2014. doi: 10.1364/OL.39.003062.

[68] Paulina S. Kuo, Jorge Bravo-Abad, and Glenn S. Solomon. Second-harmonic generation using -quasi-phasematching in a gaas whispering-gallery-mode microcavity. *Nature Communications*, 5(3109), January 2014. doi: 10.1038/ncomms4109.

[69] A. Yariv and P. Yeh. Electromagnetic propagation in periodic stratified

media. ii. birefringence, phase matching, and x-ray lasers. *JOSA*, 67(4): 438–447, April 1977. doi: 10.1364/JOSA.67.000438.